Locally Continuous-fiber Reinforced Sheet Molding Compound

Zur Erlangung des akademischen Grades eines

DOKTORS DER INGENIEURWISSENSCHAFTEN (Dr.-Ing.)

bei der KIT-Fakultät für Maschinenbau des

Karlsruher Instituts für Technologie (KIT)

genehmigte

DISSERTATION

von

Dipl.- Ing. David Bücheler

Zusammenfassung

Durch lokales Endlosfaserverstärken von Sheet Molding Compound (SMC) kann auf wirtschaftliche Weise Bauteilsteifigkeit mit Designfreiheit kombiniert werden. Um das gesamte Potenzial dieses Fertigungsverfahrens auszuschöpfen und um Bauteile gleichbleibender Qualität herzustellen, müssen allerdings das Materialsystem und die Fertigungsschritte angepasst oder teilweise neu konzipiert werden. Bisherige Arbeiten konnten positionstreue Lage und Orientierung der Endlosfaserverstärkung nicht mit den Vorteilen der Fließfähigkeit des SMCs verbinden. Daher muss nach Stand der Technik, sobald lokale Endlosfaserverstärkungen zum Einsatz kommen, das SMC formgepresst werden, um Fließbewegungen innerhalb des Werkzeuges zu reduzieren.

Durch den Einsatz eines Harzes mit zweistufiger Vernetzungsreaktion kann die Matrix der Endlosfaserverstärkung in ihrer Viskosität gegenüber Standard-UP-Harzen um eine Größenordnung erhöht werden. Auch der Viskositätsabfall im heißen Presswerkzeug ist geringer. Die abgeschlossene erste Reaktionsstufe führt zu einem steifen Einleger, der während des Pressvorgangs die Kräfte des fließenden SMCs erträgt und nicht deformiert wird. Zudem kann durch die zweite, noch nicht erfolgte Reaktionsstufe, eine chemische Vernetzung mit dem SMC erfolgen. Um eine Verschiebung der lokalen Endlosfaserverstärkung auszuschließen, wird eine innovative Fixierung mittels magnetischen Feldern entwickelt. Hierzu muss die Materialformulierung weiter angepasst werden.

Zur Umsetzung des hier beschriebenen Fertigungskonzeptes bedarf es der Materialcharakterisierung und Modellierung, zudem der Simulation des Fließprozesses und der magnetischen Felder. Experimente dienen der Validierung des Konzeptes. Schließlich konnten Bauteile hoher und gleichbleibender Qualität hergestellt werden und somit ein wichtiger Schritt in Richtung Industrialisierung gegangen werden.

Abstract

The process of co-molding of locally continuous-fiber reinforced structures with Sheet Molding Compound (SMC) has the potential to realize structures economically combining high stiffness with freedom in design. In order to exploit the full potential and to achieve reliable components, materials as well as process steps have to be tailored or completely rethought. Previous work has failed to combine the flowability of the SMC, needed to form ribs and to integrate inlays, with accurate position and intact shape of the continuous-fiber reinforcement. State-of-the-art in co-molding is still a near net-shape mold coverage of the SMC to prevent any flow.

The introduction of a two-step curing resin enables to raise the viscosity level after impregnation of the matrix of the continuous-fiber reinforcement by one order of magnitude. Additionally, the viscosity drop when placed in the hot mold is reduced, because of the cross-linking of the polymer at the first reaction step. Both results in a stiff reinforcement during co-molding, which endures the forces applied by the flowing SMC and therefore is not deformed. Furthermore, the second, still latent, reaction step allows for chemical bonding to the SMC. To prevent displacement of the reinforcement, a novel fixation method is introduced by using magnetic fields to keep the material in position. As conventional fiber reinforced plastics behave neutral in magnetic fields, the material formulation has to be modified. For this purpose ferrimagnetic particles are dispersed in the reinforcement's matrix.

To realize this innovative co-molding concept a multidisciplinary approach is needed, including material characterization and material modelling, process simulation and magnetic field simulation and likewise experiments. Hereby, the performance as well as the reliability of these hybrid structures are significantly improved and a major step toward industrialization of co-molding is achieved.

Danksagung

Ich bin froh an dieser Stelle meinen tiefen und aufrichtigen Dank ausdrücken zu können:

List of Publications

Paper I: Mechanical Properties of Unidirectional Continuous Carbon Fiber Reinforced Sheet Molding Compounds,
A. Trauth, D. Bücheler, K.A. Weidenmann and F. Henning,
17th European Conference on Composite Materials (ECCM17),
ISBN: 978-3-00-053387-7, 26-30.06.2016, pp 6716-6723.

Paper II: Hybrid Resin Improves Position and Alignment of Continuously Reinforced Prepreg During Compression Co-molding With Sheet Molding Compound,
D. Bücheler and F. Henning,
17th European Conference on Composite Materials (ECCM17),
ISBN: 978-3-00-053387-7, 26-30.06.2016, pp 6699-6703.

Paper III: Using Thermogravimetric Analysis to Determine Carbon Fiber Weight Percentage of Fiber-Reinforced Plastics,
D. Bücheler, A. Kaiser and F. Henning,
Composites Part B: Engineering, vol. 106, pp. 218–223, 2016.

The contribution of the author of this thesis to the appended paper is:

I   Material preparation and manuscript writing
II   Material preparation, characterization and manuscript writing
III   Material preparation, characterization and manuscript writing

Other publications not included in this thesis:

Expanding Applications Areas for Sheet Molding Compound (SMC) Through New Material Compositions and New Hybrid Processes,
A. Hrymak, D. Bücheler, F. Henning, V. Ugresic and M. Hohberg,
33rd International Conference of the Polymer Processing Society,
Cancun, 10.-14.12.2017.

Rheological In-Mold measurements and characterizations of Sheet-Molding-Compound (SMC) formulations with different constitution properties by using a compressible shell model,
M. Hohberg, L. Kärger, D. Bücheler and F. Henning,
International Polymer Processing, vol. 32, no. 5, pp. 659-668, 2017.

Processing of Continuous-discontinuous-fiber-reinforced Thermosets
D. Bücheler, A. Trauth, A. Damm, T. Böhlke, F. Henning, L. Kärger,
T. Seelig and K. A. Weidenmann,
SAMPE Europe Conference 2017, Stuttgart, 15.11.2017.

MAI qfast - Assessment and direct comparison of various fiber reinforced systems based on generic structures,
T. Müller, S. Ebli, J. Krämer, J. Rausch, J. Starke, M. Karcher, B. Hangs and D. Bücheler,
1st International Composites Congress (ICC),
Stuttgart, 21./22.09.2015.

Validierung eines Simulationsmodells für Wälzlager durch Abgleich von Simulations- mit Messdaten,
F. Fritz, D. Bücheler and W. Seemann,
PAMM- Proc. Appl. Math. Mech, Volume 10, Issue 1, pp 239 -240, 2010.

Patent applications related to this thesis:

Verfahren und Vorrichtung zur Herstellung von mit Einlegern versehenen Polymer-Formteilen,
D.Bücheler, DE 102014012971 A1: 20140908.

Contents

Abbreviations

CAD	Computer-aided design
CF	Carbon fiber
CNC	Computerized numerical control
CoDicoFRP	Continuous-discontinuous-fiber reinforced plastic
CoDicoFRTS	Continuous-discontinuous-fiber reinforced thermoset
CoFRP	Continuous-fiber reinforced plastic
CoFRTS	Continuous-fiber reinforced thermoset
DoE	Design of experiments
DicoFRP	Discontinuous-fiber reinforced plastic
DicoFRTS	Discontinuous-fiber reinforced thermoset
DXF	Drawing interchange file format
EM	Electronic magnet
EP	Epoxy
Fe_3O_4	Magnetite
FRP	Fiber reinforced plastic
GF	Glass fiber
MDI	Di-isocyanate
MgO	Magnesium oxide
MMA	Methyl methacrylate
ModV	Volume based model
MR	Magnetorheological
NCF	Non-crimp fabric
NdFeB	Neodymium magnet
	(alloy from neodymium, iron, and boron: $Nd_2Fe_{14}B$ [1])
pBQ	Poly benzoquinone
PCM	Prepreg compression molding
phr	Parts per hundred resin
PM	Permanent magnet
SEM	Scanning electron microscope
SMC	Sheet molding compound
SVD	Singular value decomposition

UP   Unsaturated polyester
UPPH   Unsaturated polyester polyurethane hybrid
VE   Vinylester
VSM   Vibrating sample magnetometer

List of symbols

Symbol	Parameter	Unit
$()_0$	In free space, for values towards 0	-
$()^{\parallel}$	In molding direction	-
$()^{\perp}$	Perpendicular to molding direction	-
$()_{dis}$	Displacement	-
$()_{emp}$	Empiric	-
$()_{fix}$	Fixation	-
$()_r$	Relative	-
$()_A$	Air gap	-
$()_C$	Coercivity	-
$()_{CF}$	Carbon fiber	-
$()_{Dy}$	Dynamic	-
$()_{EM}$	Electronic magnet	-
$()_{Fe}$	Iron	-
$()_M$	Magnet	-
$()_{MathFit}$	Mathematical fit	-
$()_{ModV}$	Volume based model	-
$()_N$	Normal	-
$()_{PM}$	Permanent magnet	-
$()_R$	Remanent	-
$()_S$	Saturation	-
$()_{Shear}$	Shear	-
$()_{St}$	Static	-
$()_{Temp}$	Temperature	-
$()_{UP}$	Unsaturated polyester	-
$()_{UPPH}$	Unsaturated polyester polyurethane hybrid	-
c	Degree of cure	%
c_p	Heat capacity	J/(kg K)
d	Displacement	mm
g	Acceleration due to gravity	m/s^2
h	Height	mm, m
k_B	Boltzmann constant	J/K
l	Length	mm
n	Cross exponent	-
p	Pressure	MPa

q	Electric charge	C
r	Radius	m
s	Stamp distance	mm
$\tan \delta$	Loss factor	-
v	Velocity	m/s
w	Width	mm
A	Area	mm^2
B	Magnetic flux density	T
E	Electric field strength	V/m
	or	
	Young's modulus, elastic modulus	Pa
F	Force	N
G	Shear modulus	Pa
G^*	Complex shear modulus	Pa
G'	Storage modulus	Pa
G''	Loss modulus	Pa
H	Magnetic field strength	A/m
J	Magnetic polarization	T
R^2	Coefficient of determination	-
$\bar{R}^2$	Adjusted coefficient of determination	-
$Rp_{0.2}$	Yield strength	N/mm^2
S	Material constant	Pa s
T	Temperature	°C, K
T_S	Material constant	°C
T_C	Curie temperature	°C
V	Volume	mm^3
W	Energy	J
β	Rotation	deg
$\dot{\gamma}$	Shear rate	1/s
δ	Air gap height	mm
η	Viscosity	Pa s
η^*	Complex viscosity	Pa s
λ	Thermal conductivity	W/(m K)
μ	Magnetic permeability	V s/A m
	or	
	Friction coefficient	-
μ_B	Bohr magneton, physical constant	J/T
ρ	Density	g/cm^3
τ	Shear stress	Pa

τ^*	Transition parameter	Pa
φ	Volume content	vol.-%
Δl	Change in length	%
Δw	Change in width	%
$\varPhi$	Magnetic flux	Wb
ω	Angular frequency	1/s

1 Introduction

Lightweight design for mass produced passenger cars is clearly not a new field of research and was driven by different motives during the last decades. At least since 1972 car manufacturers have reduced the weight of single components significantly by substituting non-structural metal parts by glass fiber reinforced polymeric composite components, mainly to reduce fuel consumption [2, 3]. Later, the reduction of carbon dioxide was enforced by the legislation of the European union to $130\,\mathrm{g\,CO_2\,km^{-1}}$ by 2015, respectively to $95\,\mathrm{g\,CO_2\,km^{-1}}$ by 2021 [4]. The emerging energy turnaround is currently driving the automotive industry. Replacing a conventional engine by an electrical engine including the required energy storage leads to an increase in the car's weight [5], which is an influencing factor for the cars range [6, 7]. Therefore, lightweight design is as relevant as ever, but weight reduction possibilities for non-structural parts appear to be almost exploited. Thus, the structure itself has to be tackled and we could be in the midst of a 'make-or-break' decade for carbon fiber reinforced composites [3].

1.1 Scope of Work

Chopped glass and carbon fiber sheet molding compounds (GF-SMC and CF-SMC) offer excellent characteristics for complex part geometry, functional integration, material utilization and productivity at reasonable costs. On the other hand limited fiber length and insufficient process control over fiber orientation are leading to limited mechanical strength and stiffness. [8–13]

The characteristics of continuous-fiber reinforced prepreg materials show the opposite behavior. They offer superior mechanical properties at very limited freedom of design and at high costs for material and sometimes even the process. [8–11, 14, 15]

Co-molding of prepreg material with sheet molding compound (SMC) allows for fast and cost effective manufacturing of complex but still structural composites. The flowability of SMC is suitable to realize complex geometries like ribs and to integrate inserts, whereas the continuous-fiber reinforcement creates the structural backbone of the component. Therefore, position and alignment of the continuous-fibers inside a component determines the structural integrity. [16–22]

1.2 Background

State of the art prepreg systems used in compression molding are based on unsaturated polyester (UP) [23], vinylester (VE) [18, 22] or epoxy (EP) [19–21] resins. All these resin chemistries lack the ability to create a chemically stable, highly viscous B-stage. The viscosity of MgO-thickened UP-based and VE-based prepreg drops dramatically when molded at 150 °C. Thus, the prepreg cannot withstand the forces applied by the flowing co-molding material [16]. B-staging of EP resins leads to higher viscosity levels under compression molding conditions, however the material shows a narrow process window for draping [19, 20] and short shelf life [24].

It is generally known that for state-of-the-art resin systems a reinforcing effect of the co-molded prepreg can only be achieved by eliminating flow inside the mold [19, 23, 25]. As SMC is appreciated for its superior design freedom and capability of functional integration this limitation is not acceptable. Thus, material and process development are needed to lock the continuous-fiber position and alignment during co-molding.

1.3 Objective and Approach

The aim is to realize a reliable process for co-molding of prepreg with SMC at high flow rates. Therefore, the following is postulated:

- The prepreg-matrix must provide a stable high viscous B-stage to achieve a stiff and shape consistent reinforcement under molding conditions.
- Fixation of the prepreg inside the mold is required to avoid a displacement due to the forces applied by the flowing SMC.

These conditions are supposed to be achieved by process and material development. The aspired process approach is shown in Figure 1.1.
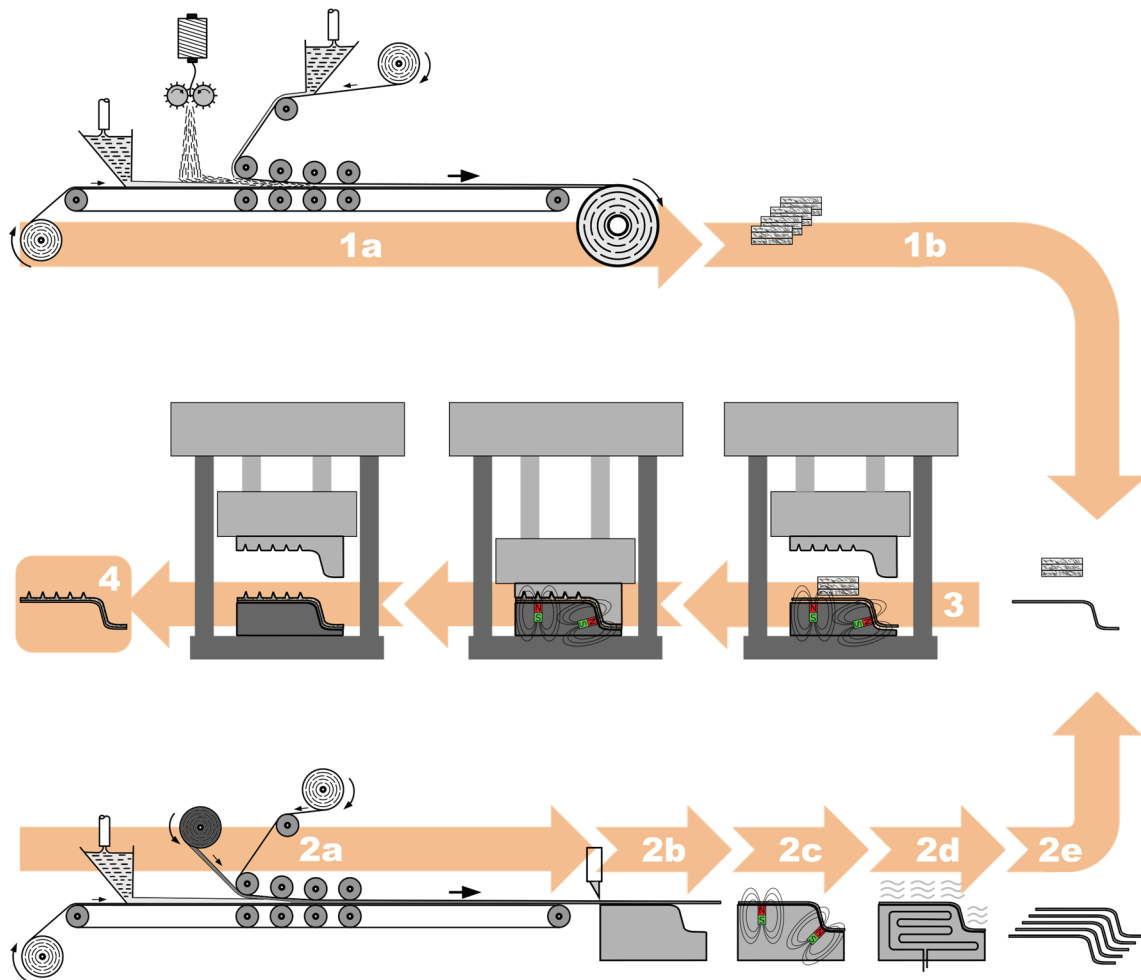
Figure 1.1: **Concept for processing of locally continuous-fiber reinforced SMC**

State of the art chopped glass- or carbon-fiber SMC is produced on a flat conveyor plant (1a), subsequently matured, cut and combined to a stack of SMC (1b). The prepreg material is manufactured accordingly on a modified and heatable flat conveyer plant (2a). Prepregs' matrix is

based on an unsaturated polyester polyurethane hybrid resin (UPPH) and combined with a 50k carbon fiber non-crimp fabric (NCF). The UPPH resin offers an alternative thickening technology leading to a stable, high viscous B-stage. This B-stage is reached in less than five minutes at 80 °C. Thus, the material is viscous enough to enable a direct cut the prepreg to dimensions of the final reinforcements (2b) without subsequent maturation. Furthermore the prepreg-matrix contains a certain amount of ferrimagnetic particles. This enables for draping of the reinforcement by one solid mold half only (2c). After a second heating step at the draping device (2d), B-staged and thus stiff reinforcements (2e) are obtained, which can be stored or processed subsequently. The final part (4) is generated by compression molding (3). Hereby, magnetic fields as fixation for the local reinforcements inside the mold are applied during co-molding with SMC.

To validate the hypotheses and to develop the process-concept various interdisciplinary experiments, calculations and simulations have to be performed. Before, however, chapter 2 introduces the current state of science and the required theoretical background. I chapter 3 and 4 the basic raw materials are selected and introduced and the prepreg formulation as well as the processing equipment is developed. Chapter 5 characterizes the prepreg material in terms of friction to the mold, mechanical properties and models its magnetical behavior. Furthermore co-molding trials and co-molding simulations are performed. This enables to discuss all relevant forces applying on the prepreg during co-molding with SMC at a 2D level. Afterwards, three different concepts of draping of prepreg are investigated with respect to their geometrical accuracy. Finally, complex structures with locally continuous-fiber reinforced Sheet Molding Compound are produced and investigated in terms of fiber alignment. The thesis closes with a summary and an outlook.

2 Current State of Science

The state of science for fiber reinforced plastics (FRPs) is characterized by a wide variety of inconclusive terms and competing definitions. Thus, this section shall provide clear explanation and classifications for the materials and processes used in the present work. Furthermore, relevant scientific fundamentals for a better understanding will be introduced briefly. Finally, a demarcation to the state of science will be given.

2.1 Pre-impregnated Semi-finished Materials

Fibers which are pre-impregnated by either a thermoset or a thermoplastic polymer are today commonly known as prepregs. Prepregs are available in flat shape, as bulk or rolled-up on coils as semi-finished materials [8, 11, 26]. Pre-impregnated materials were first used in compression molding under the name *Bakelite* in 1930 [26]. The term "prepreg" was introduced 30 years later by *Boeing*. The company developed a material of continuously uni-directional aligned fibers impregnated by a thermoset resin for structural parts [8, 26]. With aerospace as main application for the *Boeing* material, the term is often reduced to this specific material class and therefore associated with high cost and small quantities. This thesis however discusses prepreg materials in the context of mass production.

The separation of component manufacturing from fiber impregnation is an advantage of prepregs towards process technologies combining fibers and matrix during the production of the part. On the one hand, the component manufacturer does not necessarily need profound understanding of the chemistry of the material - the production of components made of fiber reinforced plastics is thus relatively straight forward [15, 27]. On the other hand, prepregs produced by suppliers specialized in the production of these semi-finished materials are

showing high quality by low deviation of fiber content at low void content [11, 15, 28].

Besides matrix material, delivery form or application, prepregs can be categorized by flowability, fiber type or fiber condition [8, 9, 11, 14, 26]. Within this thesis two types of prepregs are in the focus. The fiber condition is either continuous and parallelly aligned or discontinuous and randomly distributed in two dimensions. These two FRP systems are named according to Figure 2.1 as CoFRP and DicoFRP. The CoFRP material should be non-flowable, the DicoFRP flowable. A combination of both materials is named CoDicoFRP. Furthermore, for this thesis the prepregs' matrix material is limited to thermosets (TS).
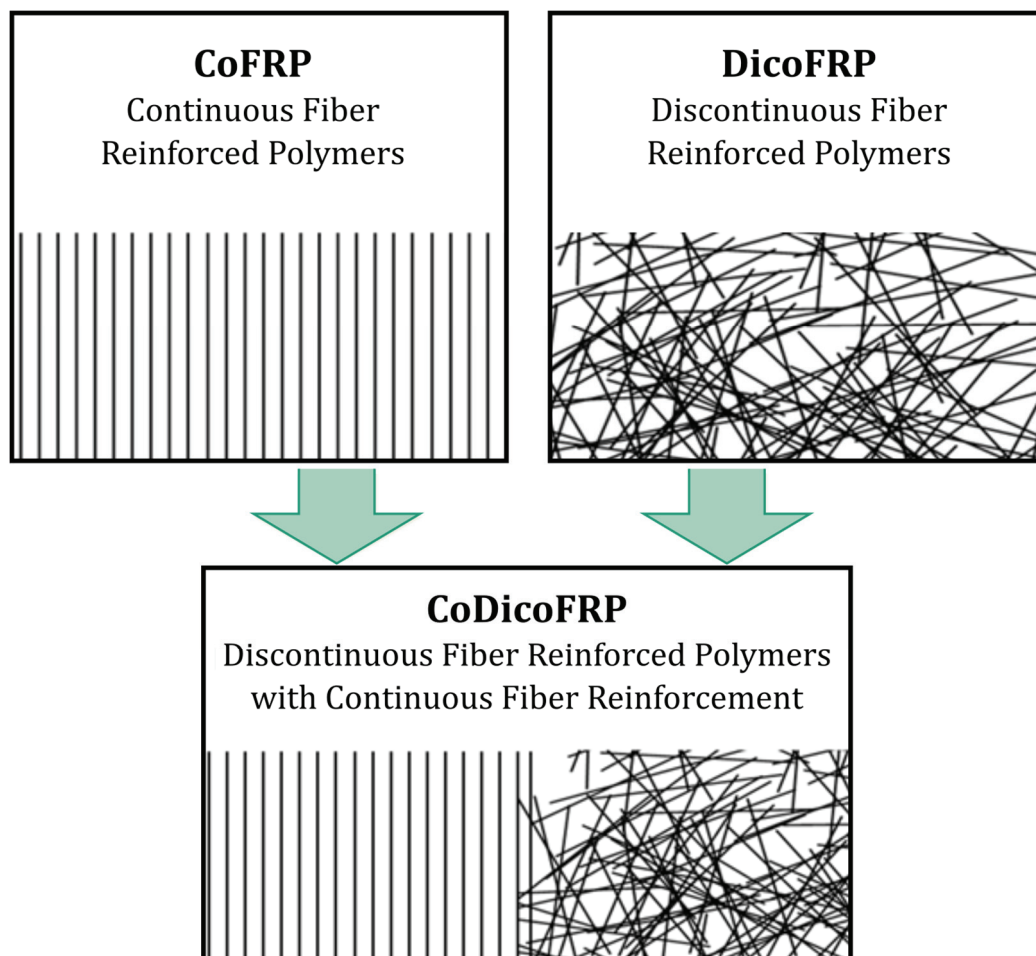
Figure 2.1:   Explanation of terms, according to [29]

2.2 Sheet Molding Compound

In Europe the FRTS system of highest economic importance in terms of production volume is Sheet Molding Compound (SMC) [8, 30]. SMC is a DicoFRTS material and can be classified as flowable pre-impregnated semi-finished material [26]. SMCs ingredients vary extensively [31]. A usual compound could be composed for example of unsaturated polyester resins, chopped glass fibers of 25.4 mm length (2 inch), mineral fillers and additives [8, 31]. The impregnation of the fibers is achieved by the help of a flat conveyor plant (see Figure 2.2.) at relatively low viscosity of the matrix material.
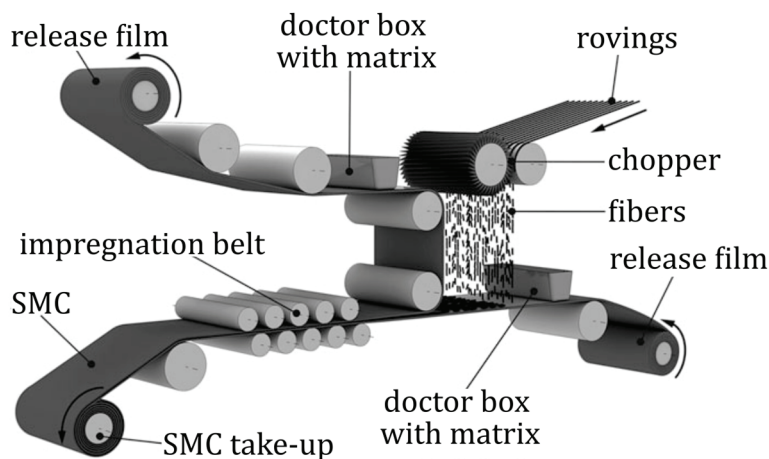
Figure 2.2:   Schematic drawing of a flat conveyor plant, according to [14]

The manufacturing of components is then done by compression molding. Between these two process steps the SMC is usually stored at elevated temperature to increase the viscosity of the matrix. This is called thickening. Impregnation and molding are extensively described in literature [8, 9, 11, 14, 26, 31, 32]. However, the mechanism of thickening is still topic of fundamental research.

2.2.1 Thickening by Magnesium Oxide

In the period between impregnation and molding the resin paste has to increase its viscosity from about $10 - 30$ Pa s to $2 \ 10^4 - 15 \ 10^4$ Pa s [9,

31] to enable handling operations prior to molding. This drastic increase is usually achieved by adding alkaline earth metal oxides or hydroxides as thickening agent. Besides calcium oxide, calcium hydroxide and magnesium hydroxide, the thickening agent most used in industry is magnesium oxide (MgO) [31]. The thickening mechanisms of unsaturated polyester resin and MgO is investigated since 1970 [33], but still not understood satisfyingly [34]. In general, the published works describe either a two or a four step mechanism starting with the dissolution of the magnesium oxide and a simple acid-base reaction [31, 33, 35–39]. In each case a stable chain extension is achieved next to a weak and reversible three dimensional formation of the molecules. As those models fail to explain several observations made by the use of MgO, like the absence of thickening when using reagent grade MgO, Eisemon and Lewis [40, 41] proposed an alternative mechanism. This mechanism assumes that there is no dissolution of the magnesium oxide, but rather the MgO is present as crystal aggregate having a large surface. Lattice defects in this surface could act as a catalyst for a polymerization reaction or chemisorb the polyester (compare Figure 2.3). In either case, this would lead to an increase in molecular weight and thus in an increase in viscosity.
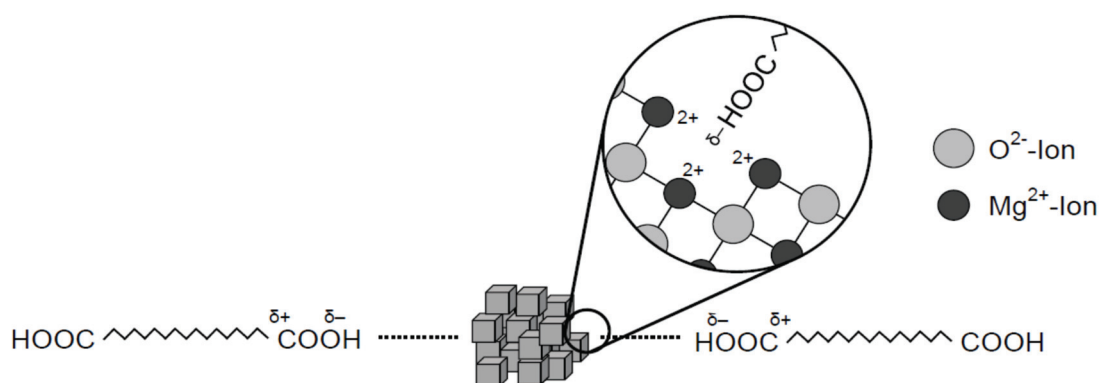
Figure 2.3:   **Mg0 thickening mechanism, according to Eisemon and Lewis [34]**

2.2.2 Thickening by Isocyanate

Another possibility in thickening of polyesters is the use of isocyanate. Hereby, the hydroxyl and carboxyl groups of the UP form covalent bonds with the isocyanate and increase consequently the viscosity [42]. Mostly, the influence of isocyanate thickening on shrinkage was investigated [42, 43], rarely its influence on mechanical properties [44]. From 1984 onwards, Edwards [45–48] published information of a polyester resin specifically modified for isocyanate thickening and the idea was adopted by several others [49–53]. This new resin class was developed to combine the advantages of polyester and polyurethanes and will be called unsaturated polyester polyurethane hybrid (UPPH) in the following. In most cases the UP resin was modified to provide only terminal hydroxide groups for the isocyanate. Thus, the full length of the molecule carries loads and improves hereby the ductility of the matrix. Summarized, mechanical properties like tensile strength, toughness, impact resistance, elongation at break and the thermal stability of the fully cured polymer can be improved [53].

2.3 CoFRTS for Compression Molding

CoFRTS materials are usually produced by either solvent or hot melt impregnation [11, 54]. In solvent impregnation the fibers are guided to a matrix dip. The resin in this dip is blended with solvent to achieve low viscosity and good impregnation. A heating tunnel is then used to remove the solvent and to start a preliminary cross linking of the resin before the prepreg is rolled up [14]. Due to the increased environmental awareness and the risk of residual solvent, the use of solvents has to be avoided and the hot melt impregnation is gaining market shares [11, 55]. Hot melt impregnation is often done in two steps. First the resin is heated to achieve low viscosity and is filmed on a foil or paper. In a second step this resin carrier gets in contact with spread out fiber filaments. Calenders and heating devices ensure uniform thickness and complete impregnation. Uni-directional CoFRTS materials are usually made by hot melt processing. The spread out fibers show low thickness

and can be completely impregnated by the high viscous hot melt resins. Fabrics are limited regarding spreadability of the single roving and show greater thickness. They are impregnated by solvent processes, because of the lower resin viscosity achievable. [11, 55, 56]

Most prepreg materials showing a continuous-fiber condition are used for autoclave processing [15, 54]. The heat transfer is here driven by convection. This results in long cycle times. The low degree of automation leads to high labor costs. Along with high capital investment required, the component costs are inevitable high for components manufactured by autoclave processing. [15, 55, 57]

For mass production the even higher invest costs for hydraulic press and mold [24] can be accepted due to low cycle time and high degree of automation. As a result of isothermal driven molds and conductive heat transfer, the cycle time is dominated by the curing time of the resin system. Thus, the use of fast curing materials can enable cycle times of one to four minutes [58]. However, there is no time for complex draping of the prepreg in the mold. Thus, parts of high complexity have to be preformed prior to molding.

The high pressure achievable in the mold (up to 300 bar) leads to excellent consolidation of the single layers and low porosity [15]. Upon reversion, there is a potential in cost saving at the production of the semi-finished material. For instance the complicated process step of spreading the fiber tows becomes obsolete. Thus, conventional flat conveyor plants meant for the production of SMC can be used [24].

Such CoFRTS materials made for compression molding are also called Prepreg Compression Molding (PCM) [19, 20] or Advanced SMC [59, 60]. There are several companies producing commercial products such as *Polytec Composites GmbH, Quantum Composites, Mitsubishi Rayon Europe GmbH, Polynt Composites Germany GmbH or Menzolit GmbH.* Most of these materials are based on a fast curing polyester or vinylester resin system (around 30 s/mm part thickness [61]). But all of them can be classified as flowable prepreg material. This is not an is-

sue, when having 100 % of mold coverage. However, these systems are limited when it comes to complex shapes and co-molding at the production of CoDicoFRTS components. The forces applied to the CoFRTS by the flowing DicoFRTS lead to deformation and displacement of the continuous-fibers during co-molding [16]. For complex shapes a draping step forming the CoFRTS prior to molding is essential [23, 25]. However, a flowable prepreg material leads to a relatively soft CoFRTS preform. This is disadvantageous for handling operations needed in between of draping and molding [18].

2.4 Draping of CoFRTS

For parts made from DicoFRTS a draping process step is not required as the material's flowability can fill cavities of high complexity during compression molding. However, to generate non-planar structures consisting of CoFRTS the material has to be draped. A flow of the CoFRTS inside the mold would be accompanied by an unwelcome deformation of the fibers.

The technologies used for draping of textiles or prepregs can be classified into manual draping, rigid tool based draping, robot based draping or draping by diaphragm:

- **Manual draping** is used for dry textiles and prepreg. It is widely spread and especially used for small parts or parts of high complexity [15]. The positioning of the CoFRTS can be assisted by laser projection systems [62]. It is mostly limited to woven materials because of their high formability (compare Figure 2.4) and reproducible draping mechanisms [15].
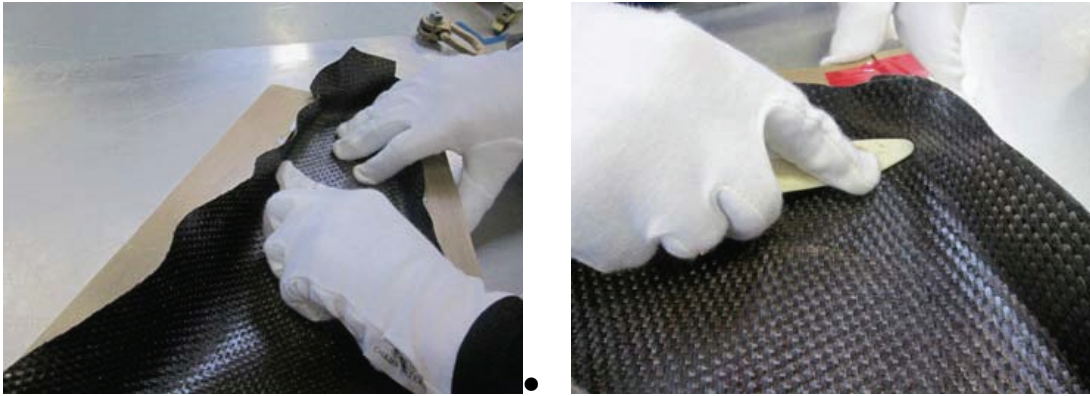
**Figure 2.4:** Manual draping of woven prepreg [15]

- **Rigid tool based draping** is capable of series production for large preforms of simple to medium complexity. Thus, it is applied in series production at *BMW*. Rigid tools are used to drape vehicle roofs out of fleece and woven fabric for the *i3* and the *M3* (compare Figure 2.5). [63]
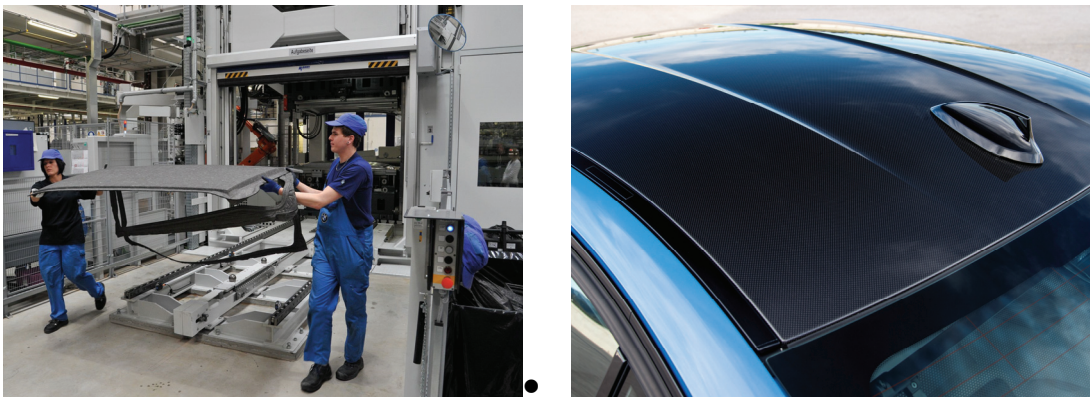
Figure 2.5: Rigid tool based draping at BMW
left: Draping of fleece for the i3 [64]
right: M3 roof made of impregnated woven textile [65]

To further increase the complexity, the tool can be divided into smaller, independently moveable units called stamps. This reduces fiber misalignment and wrinkling [66]. The corresponding process sequence is shown in Figure 2.6: As input serves the two-dimensional layup of the fabric, which is called stack. A heated draping belt supplies this stack (a) to the draping mold (b). In a next step the stack is fixed (c) and partly draped (d). When the mold is completely closed (e), the binder is cured. The output after demolding

(f) is a stable, three-dimensional preform ready for impregnation. Stamp draping is used, for example, to manufacture B-pillars for the *Lamborghini Huracán LP 610-4* [67].
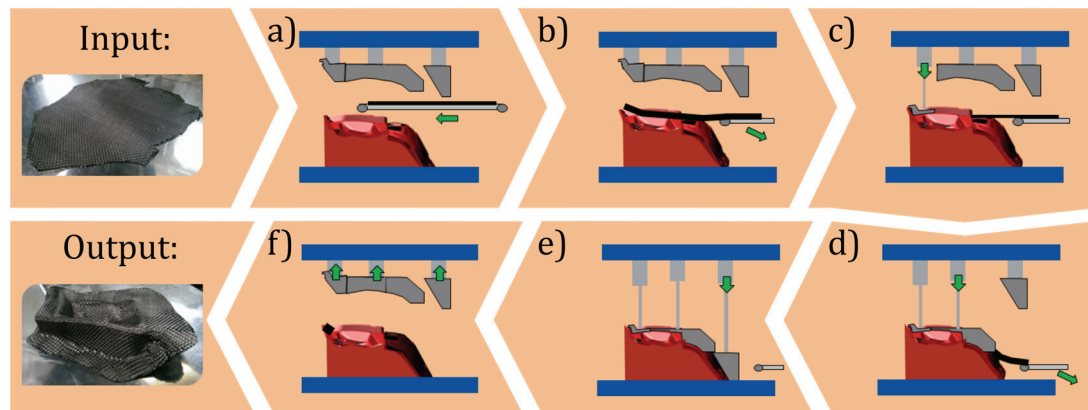
Figure 2.6: Process flow of stamp draping, according to [66]

- **Robot based draping** processes consist of a fiber placement system and a standard industrial robot as used in the automotive industry. The systems are capable of laying pre-impregnated continuous-fibers preferably on a negative mold half. The benefit in using robots rather than fixed machines is the low invest, proven technology and high flexibility [68]. Thus, there is a remarkable interest of the scientific society in this draping technology [69–71]. Commercial systems are for instance available from the companies *Coriolis Composites* or *M. Torres* with aerospace as their core market [15]. The disadvantage of this technology is the relatively slow layup and the limited capability of parallelization. Currently a maximum of four parallel fiber placement systems, providing a prepreg width of 150 mm each, are in use [15].
- **Draping by diaphragm** was developed based on the process of deep drawing of thermosets. Thus, it is characterized by a draping tool and one or two diaphragms covering or embedding a two-dimensional layup of prepreg. The forming is done by vacuum. To support interlaminar slip, the process is usually performed at elevated temperatures [15, 72].

Draping by diaphragm shows low invest [72], is very flexible and particularly well suited to form large geometries as well as undercuts [15, 72]. These are all advantages which cannot be provided by rigid tools.

2.5 Locally Continuous-fiber Reinforced DicoFRTS

In the field of thermoplastic FRP numerous results were published addressing the combination of short- or long-fiber reinforced thermoplastics with continuous-fibers pre-impregnated materials, such as organo-sheets [73], tapes [74] or wound structures [75]. In the field of thermosets, however, very few comparable research results are published. Figure 2.7 shows the achievements on the product side: GM installed the windshield surround on the 2003 Dodge Viper based on the combination of GF-, CF- and PCM to increase the part stiffness [22]. Moreover an abstraction of a suspension arm and a subfloor structure were presented which combine the stiffness and strength inherent in the prepreg with the geometrical stiffness by forming complex ribs with carbon fiber reinforced SMC [21, 76]. No details of molding conditions are published for the suspension arm. For the subfloor structure the flow of material inside the mold had to be minimized to keep the reinforcement's structure intact. Thus, the initial charge of SMC showed mold coverage of 99 % at tailored thickness following the thickness of the final part.

Figure 2.7: **Structural components made of CoDicoFRTS**
left: Windshield surround [22]
center: Suspension arm [21]
right: Subfloor structure [76]

1986 Mallick [77] described a benefit in tensile strength of CoDi-coFRTS plates compared to pure DicoFRTS plates. Furthermore he found decreasing tensile strength with decreasing mold coverage due to misalignment of the continuous-fibers because of material flow.

Akiyama [19, 20] addressed 2011 and 2013 draping of prepreg and co-molding with CF-SMC. For the prepreg, an epoxy resin system optimized for draping and compression molding was used. The flexural bending properties of SMC could be significantly increased by co-molding with prepreg, on specimen level. On part level a subfloor structure was manufactured by combining prepreg draped by a rigid tool with CF-SMC in compression molding (see Figure 2.8). Hereby, the CF-SMC forms ribs and includes a screw boss. Beginning with a production rate of 200 parts a month, the process shows an economic benefit against autoclave production and resin transfer molding (RTM). However, the complex cutting pattern and layup of the SMC before molding indicates, that a high flow of chopped fiber material would compromise the position and alignment of the uni-directional fibers.

**Figure 2.8:** CF-SMC mold coverage before co-molding and final part [19]

Wulfsberg et al. [23] reported 2014 of a significant improvement of the tensile strength when co-molding DicoFRTS with CoFRTS. However, the results are based on 2D plates only. They specify a fixation of the CoFRTS during the co-molding process as key parameter, which in an outlook of their research has to be developed in future.

In 2015, Gortner [78] introduced the process of co-molding unimpregnated fabrics with DicoFRTS. Using conventional DicoFRTS leads to

poor impregnation of the fabric (void content 9 %). By reducing the DicoFRTS viscosity the impregnation is improved. However, the remaining void content of 3 % and the modifications of the DicoFRTS needed, lead to unsatisfying mechanical properties of the CoDicoFRTS specimens.

2016, Pangboonyanon et al. [25] described a co-molding process as well. They conclude that a DicoFRTS mold coverage of 100 % is indispensable and draping of the CoFRTS improves the components quality (see Figure 2.9).
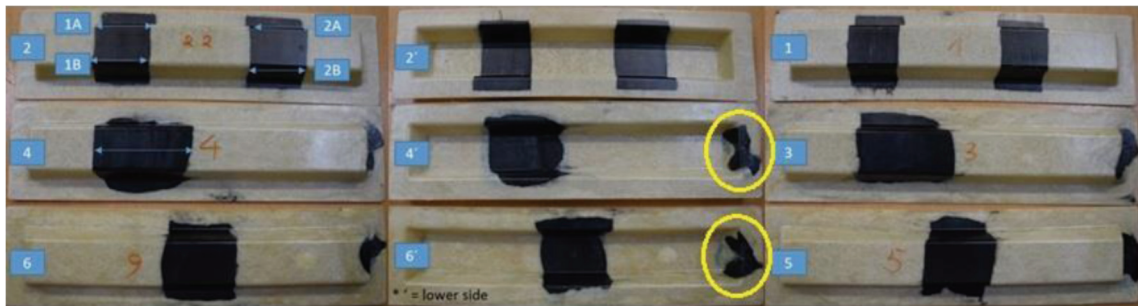
Figure 2.9:   **Co-molded components of different DicoFRTS (yellow) mold coverage [25]**
                            parts on top: 100 % mold coverage
                            other parts: 25 % mold coverage

Corbridge et al. [60] developed an analysis method in 2016 to quantify distortion of CoFRTS due to co-molding with DicoFRTS. Furthermore, the authors were able to significantly reduce fiber misalignment by advancing the degree of cure of the CoFRTS prior to co-molding. However, the staging reduced the interfacial properties.

2.6 Friction of CoFRTS to Mold

During co-molding with DicoFRTS the CoFRTS material is fixated by the hydrostatic pressure applied by the press which is transferred by the DicoFRTS material. Hereby, the friction coefficient between CoFRTS and mold defines the maximum displacement force. However, this friction coefficient has up till now been little examined.

Kim [79] used local patches of glass-fiber-reinforced prepreg in compression molding and compared the material flow with process simulations. He reports of a strong interaction of material flow to the mold-prepreg friction. However, he does neither indicate the molding conditions, nor the prepreg material.

Chen et al. [80] investigated the friction between carbon-fiber-reinforced prepreg and compression molds of different mold materials at different temperature and molding pressure. The results indicate a change of the frictional mechanism by changing the temperature. The molds surface roughness has great effect on the friction coefficient. Furthermore, the influence of temperature is higher than the influence of external pressure. However, the resin system was not varied. Thus, the results are limited to epoxy based prepreg.

2.7 Introduction to Magnetism

It is intended to use magnetic fields to manipulate the material behavior during the different process steps in FRP manufacturing. The following sections will give a short introduction into magnetism with focus on magnetism in the solid state.

In 1982 Lorentz [81] showed that there is a force F on a charge q moving with the velocity v through an electromagnetic field. Hereby, this electromagnetic field is characterized by the electric field E and the magnetic field H.

$$\boldsymbol{F} = q(\boldsymbol{E} + \boldsymbol{v} \times \mu_0 \boldsymbol{H}) \tag{2-1}$$

$$[\boldsymbol{F}] = \mathrm{N}$$

The force can be split into an electrical and magnetic proportion:

$$\boldsymbol{F}^{\mathrm{E}} = q\boldsymbol{E} \tag{2-2}$$

$$[\boldsymbol{E}] = \frac{\mathrm{V}}{\mathrm{m}}$$

$$\boldsymbol{F}^{\mathrm{H}} = q\,(\boldsymbol{v} \times \mu_0 \boldsymbol{H}) \qquad \text{(2-3)}$$

$$[\boldsymbol{H}] = \frac{\mathrm{A}}{\mathrm{m}}$$

A magnetic field H which is present in an area A results in a magnetic flux Φ. This flux depends on the magnetic properties of the medium within A. The medium is specified by its magnetization M and its permeability μ. In free space the permeability is defined by the physical constant μ_0 and the magnetization is zero. The corresponding magnetic flux is defined by [81]:

$$\boldsymbol{\Phi} = \mu_0 A \boldsymbol{H} \qquad \text{(2-4)}$$

$$[\boldsymbol{\Phi}] = \mathrm{V\,s} = \mathrm{Wb}$$

$$\mu_0 = 4\,\pi\,10^{-7}\,\frac{\mathrm{V\,s}}{\mathrm{A\,m}}$$

The magnetic flux density B, or magnetic induction, is given by [81]:

$$\boldsymbol{B} = \frac{\Phi}{A} \qquad \text{(2-5)}$$

$$[\boldsymbol{B}] = \frac{\mathrm{V\,s}}{\mathrm{m}^2} = \mathrm{T}$$

The link between magnetic field strength H and magnetic flux density B in free space results from (2-4) and (2-5):

$$\boldsymbol{B} = \mu_0 \boldsymbol{H} \qquad \text{(2-6)}$$

Summarized, common parameters to characterize magnetic fields are the magnetic field strength H, the magnetic flux density B and the magnetic flux Φ.

2.7.1 Materials in Magnetic Fields

According to (2-6), the relation between the magnetic field strength H and magnetic flux density B is linear for free space. If there is material within the magnetic field, the material will get magnetized itself. Its magnetization M may strengthen or weaken the external field.

This material behavior is dependent on the interaction between the external field, electrons of the atomic shells in the material and their spin [82, 83]. A detailed explanation of these phenomena can only be achieved by the help of quantum mechanics and can be found in e.g. [84, 85]. A more descriptive model is the so called molecular magnet, which is defined as the smallest magnetic unit inside a material. A molecular magnet operates as a dipole. The forces on his poles cause a moment, the magnetic moment. Areas of adjacent molecular magnets of the same orientation are called magnetic domains or Weiss domains [83] and are visualized in Figure 2.10.
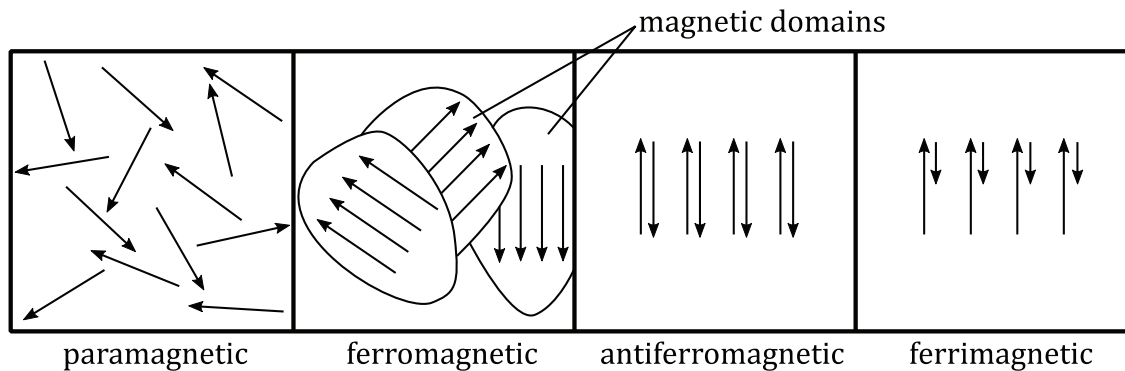
Figure 2.10: Magnetic domains and material classification

The configuration of the magnetic domains controls the magnetization M and thereby the material behavior within magnetic fields. Formula (2-7) is valid for any material other than free space [81]:

$$\boldsymbol{B} = \mu_0(\boldsymbol{H} + \boldsymbol{M}) \tag{2-7}$$

$$[M] = \frac{A}{m}$$

By introducing the relative permeability μ_r an alternative representation is found [82]:

$$\boldsymbol{B} = \mu_0\mu_r\boldsymbol{H} = \mu\boldsymbol{H} \tag{2-8}$$

The magnetic polarization J gives information about the strength of the molecular magnets as it considers only the part which the material delivers to the magnetic field [86]:

$$J = B - \mu_0 H = (\mu_r - 1)\mu_0 H \tag{2-9}$$

$$[J] = T$$

Thus, the magnetic polarization J is the ideal parameter to compare technical magnetic materials. Whereas the configuration of the magnetic domains is suitable for a general classification (compare with Figure 2.10):

- **Diamagnetism ($\mu_r < 1$):** Diamagnetic behavior occurs to elements with a full last shell of electrons [87]. An external field induces an electromotive force in the elementary current loops. This results in a circulating current inside the atom, which is by Lorentz law opposite to the external field [81]. The total magnetic field gets weaker [88]. The material is pushed out of the magnetic field. The phenomenon of diamagnetism is weak and often covered by other types of magnetism. Diamagnetism is more or less independent from temperature changes. Examples for diamagnetic materials are Cu, Bi, Au, Ag and H_2 [87] as well as CF-fibers [89, 90].
- **Paramagnetism ($\mu_r > 1$):** This type of magnetism occurs to not fully filled shells of electrons [87]. Without an external field the magnetic moments are randomly distributed. In the presence of an external field the magnetic moments are getting orientated according to this field. The total magnetic field gets stronger [88]. Thermal energy causes disordering and disturbs the ordering magnetic energy [81]. Thus, μ_r is related to the temperature. Examples for paramagnetic materials are Al, O_2, W, Pt and Sn [87].
- **Ferromagnetism ($\mu_r \gg 1$):** For ferromagnetic materials the magnetic moments are parallel orientated within magnetic domains of a size between 10 µm and 1 mm [87]. In absence of an external magnetic field the magnetic domains are orientated in such way that the internal magnetic field is balanced out. An external field is able to

reorientate the magnetic domains partly reversible and partly irreversible [87]. The resulting magnetic field is stronger than the original field. If the external field is removed the irreversible reorientation of the magnetic domains causes a staying magnetization of the material [88]. To neutralize the material an opposite magnetic field has to be applied. For some ferromagnetic materials it is possible to neutralize by heating the material up above a specific temperature. This temperature is called Curie temperature T_C. At T_C the material changes its phase and behaves paramagnetic [81]. Fe, Co and Ni are examples for ferromagnetic materials [91].

- **Antiferromagnetism ($\mu_r > 1$):** Contrary to ferromagnetic materials the magnetic moments of antiferromagnetic materials are pairwise antiparallel [92]. Thus, the magnetic moments compensate each other and the value of μ_r is small [93].By exceeding the Néel temperature (which is comparable to T_C for ferromagnetism) the material becomes paramagnetic [92]. MnO, NiO, CoO, CrF_3, FeF_3 and CoF_3 are examples for antiferromagnetic materials [93].

- **Ferrimagnetism ($\mu_r \gg 1$):** For ferrimagnetic materials the magnetic moments are arranged pairwise antiparallel but with different values of the partners. Thus, they are not able to compensate each other [92]. Below T_C the relative permeabilty is depending on the temperature. Exceeding T_C the material becomes paramagnetic [93]. Examples for ferrimagnetic materials are $NiFe_2O_3$, $CoFe_2O_3$ [87] and hexagonal ferrites $MeO\ 6Fe_2O_3$ (with Me: Ba, Sr, Pb) [93].

Formula (2-8) describes the permeability of a material in relation to the permeability of the free space. This is a convenient and practical way to describe magnetic properties of a material. Theoretically, the direct determination of the permeability μ would be the best factor to describe the $B = f(H)$ relation. But in practice, this is not expedient [81]:

- The relation between B and H is nonlinear in the predominant case. So a fix value for the permeability μ can give information only for a specified working condition.

- The magnetization M of the material is shape dependent.
- The magnetic properties of most materials are anisotropic. Thus, μ should be described as a tensor.

Therefore, it is useful to describe a technical material by its magnetization curve.

2.7.2 Magnetization Curve and Hysteresis Loop

The magnetization curve represents the relationship between the flux density B inside a material and an external magnetic field with the strength H. Figure 2.11 shows a typical magnetization curve for ferromagnetic materials starting with a fully demagnetized state (primary magnetization curve). This curve can be divided into several parts [81]:

- By applying a small magnetic field the domains with closest direction to the direction of the external field are expanding at the expense of other domains. This process is reversible – if the external field is removed the material returns to its ordinary state without hysteresis.
- For higher fields the changes are getting irreversible and the permeability reaches its maximum. The domain walls are moving partly abrupt. This can be made audible by connecting a speaker to a coil, which is wrapped around the material. The domain walls movement will generate voltage pulses in this coil. The resulting sound is called Barkhausen noise.
- When the magnetic field strength is further increased (above the knee point in Figure 2.11), the movements of the domain walls vanish and the magnetic moments are starting to rotate in direction of the external field. The permeability decreases.
- For an even higher magnetic field strength the magnetic moments are aligned according to the external field. The material reaches its saturation.
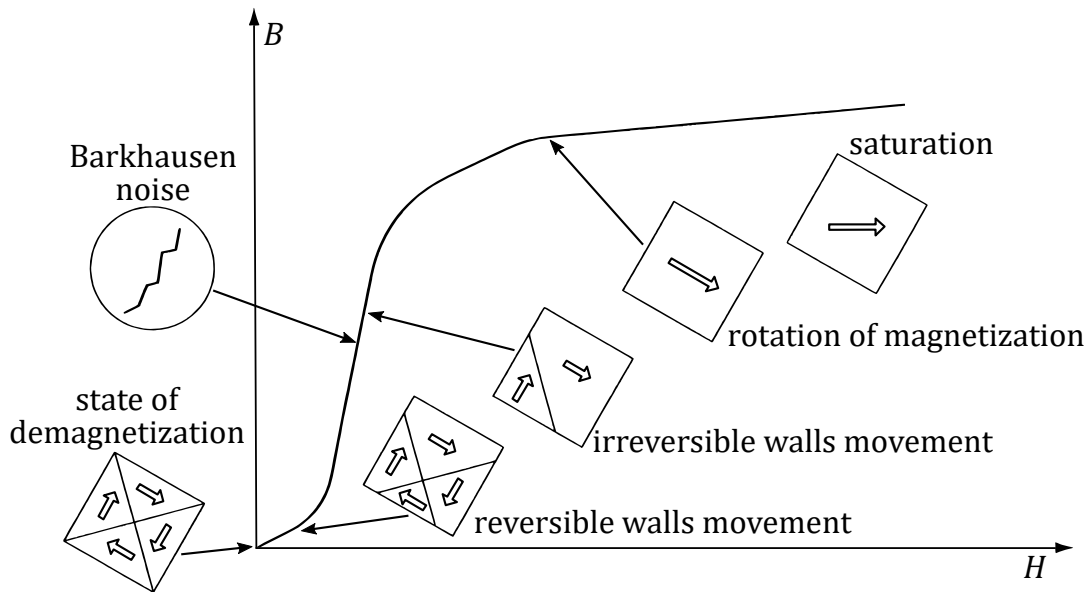
Figure 2.11: Primary magnetization curve of ferromagnetic materials, according to [81, 94]

Summarized, the dependency $B(H)$ is nonlinear for practically all ferromagnetic materials [81]. Therefore, the relative permeability μ_r is a function of H. Furthermore μ_r is dependent of the history of the material. By applying the field strength H to a fully demagnetized material the magnetic flux density B will behave according to the primary magentization curve shown in Figure 2.11 and reaches it saturation flux density B_S (see Figure 2.12). After removing the external field, the material remains magnetized with a residual or remanent flux density B_R. To obtain full demagnetization an opposed magnetic field has to be applied [81]. This field is called coercivity H_C.
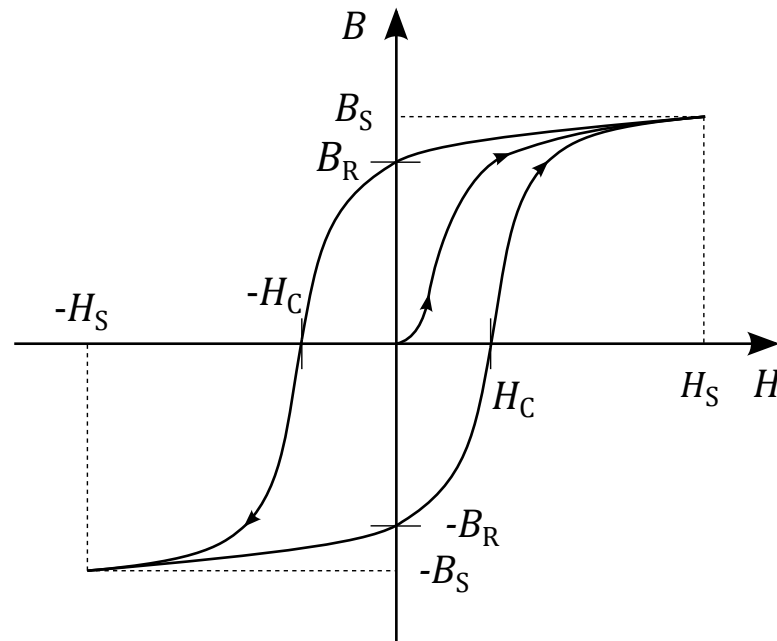
Figure 2.12: Hysteresis loop and characteristic points, according to [87, 88]

2.7.3 Magnetic Force

The force of repulsion or attraction of a magnet on any material is based on the difference in permeability at the corresponding interfaces. In the following the interface between iron ($\mu_r \sim 10^3$) and air ($\mu_r = 1$) is considered. For high leaps this force can reach high values and is interesting for technical applications. The force is perpendicular to the interface and anxious to maximize the conductivity. The consequence is a repulsion or attraction force. The energy required to generate this force is stored within the magnetic field and can be written as mechanical energy by the help of analytic mechanics and the method of virtual displacement [95]:

$$F = \frac{\partial W}{\partial x}$$
(2-10)

$$[W] = \text{J}$$

The energy density of the magnetic field W_m is equal to the product of the magnetic field strength H and the magnetic flux density B. Regarding the example shown in Figure 2.13, the volume of air V_A between

24

iron and permanent magnet (PM) is decisive for the stored energy. The height of the air gap is defined as δ, scattering effects are neglected [96]:

$$W_\text{m} = \frac{1}{2} B_\text{A} H_\text{A} V_\text{A} = \frac{1}{2} B_\text{A} H_\text{A} A_\text{A} 2\delta \qquad \textbf{(2-11)}$$

If the system is considered closed, the attraction force (also known as reluctance force or Maxwell force) can be calculated according to (2-10):

$$F_\text{m} = \frac{\partial W_\text{m}}{\partial \delta} = B_\text{A} H_\text{A} A_\text{A} = \frac{B_\text{A}^2 A_\text{A}}{\mu_0} \qquad \textbf{(2-12)}$$

Consequently the reluctance force is strongly dependent of the magnetic flux density in the air gap. For closer consideration of the flux density, Ampère's circuital law is introduced [97]:

$$\oint \boldsymbol{H} \, \mathrm{d}\boldsymbol{s} = l_\text{Fe} \frac{B_\text{EM}}{\mu_0 \mu_\text{r Fe}} + 2\delta \frac{B_\text{A}}{\mu_0} + 2h H_\text{PM} \qquad \textbf{(2-13)}$$

where

l_Fe is the total length of the iron parts

B_EM is the magnetic flux density of the electronic magnet (EM)

B_A is the magnetic flux density of the air gap

h is the height of the permanet magnets
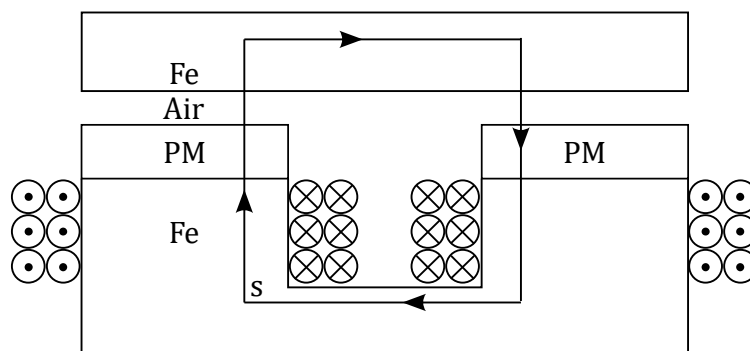
Figure 2.13: Path of integration for a setup of magnets

For more complex setups of magnets and three-dimensional calculations finite element method (FEM) software should be used. Mathe-

matical basis for such magnetic field simulations are the Maxwell equations (Ampère's circuital law is one of them but slightly modified).

2.8 Magnetic Manipulation of FRPs

State-of-the-art FRPs are paramagnetic and behave neutral in the presence of magnetic fields. There are at least two suitable possibilities to change this:

- If the reinforcing fiber is made of carbon, it is possible to conduct electrical current through the fiber. By exposing the current transmitting fiber to a magnetic field, the fiber experiences a force, called Lorentz force. This approach is already reported in literature: Delisle and Zacharias [98] describe a process for contactless draping of textiles by using the Lorentz force.
- The other possibility is to equip the FRP with diamagnetic, ferromagnetic or ferrimagnetic materials. Examples therefore can be found in literature, too: Strasser and Biber [99] report about a magnetic fixation concept of reinforcements during injection molding of thermosets. Hereby, the reinforcement shall contain ferromagnetic material. Krüger and Salkic [100] describe the procedure of draping of textiles containing additional ferromagnetic fibers by magnetic fields.

2.9 Introduction to Rheology

The natural science of rheology describes materials having properties described by any relationship between force and deformation. Hereby, the Newton-Stoke law and the Hooke law are well known models for limiting cases of rheology [101]. The rheological properties of a material can be described by the parameters viscosity η, elastic modulus E and shear modulus G [102]. In general, all materials occurring in nature show elastic and viscous behavior at the same time and are therefore viscoelastic [103].

2.9.1 Determination of Viscosity and Viscoelasticity

The viscosity η of a thermoset resin depends on temperature T, shear rate $\dot{\gamma}$ and the degree of cure c [61]. Furthermore added particles like $CaCO_3$ or fibers will affect the viscosity. Absolute measuring methods to determining η are typically based on the quotient of shear stress τ to shear rate $\dot{\gamma}$ [101, 103]:

$$\eta = \tau/\dot{\gamma} \qquad \textbf{(2-14)}$$

$$[\eta] = \text{Pa s}$$

$$[\tau] = \text{Pa}$$

$$[\dot{\gamma}] = \text{s}^{-1}$$

Usual laboratory devices for this purpose are the capillary viscosimeter and the rotational rheometer [101].

To determine the viscosity of fiber reinforced resins meant for compression molding the measuring volume of the laboratory devices are usually too small. They are incapable of handling a characteristic portion of the material. Furthermore the heating rates of the devices are too low to emulate process condition. Thus, several investigations were published to determine materials viscosity during processing by the help of molds and presses equipped with sensors [102, 104–111].

The investigation of viscoelastic material properties are performed by oscillation methods [101]. Due to very small deformations this method is able to characterize liquid as well as solid materials. Thus, it is ideal to measure resins during curing and oscillation measurements were chosen to characterize the resins in the following. The deformation is hereby described by the angular frequency ω. The complex shear modulus G^* is calculated as vectorial sum of storage modulus G' and loss modulus G''.

The complex viscosity η^* is then calculated as following [112]:

$$\eta^* = \frac{G''}{\omega} + \mathrm{i}\frac{G'}{\omega}$$

(2-15)

$$[\eta^*] = \mathrm{Pa\ s}$$

$$[G', G''] = \mathrm{Pa}$$

$$[\omega] = \mathrm{s}^{-1}$$

The quotient of loss modulus to storage modulus is defined as loss factor $\tan\delta$ [103]. The loss factor gives information about the portion of viscosity to elasticity and is central information for the processing of the material. At the moment G' is equal to G'' the gel-point for thermo-set materials is reached [103]. The ability for this precise determination of the gel-point is another benefit of the oscillation methods compared to rotational methods. After the gel-point is reached, the elastic properties of the material are dominant and from a physical side of view the term viscosity is incorrect from now on as the material has become a solid. For reasons of simplicity the following graphs will ignore this fact unless the shares of elasticity and viscosity are of interest.

2.9.2 Modelling of Viscosity

Cross [113] as well as Carreau [114] presented equations to describe the viscosity of pseudoelastic fluids. The equations are capable to describe the Newtonian like behavior of a resin at low shear rates and a power law behavior at high shear rates. Later, different modifications of these models were published [115]. In particular a transition parameter τ^* was introduced to achieve a soft transition region between the two behaviors. According to Dantzig and Tucker [116] the most applied models show a form like this:

$$\eta(\dot{\gamma}) = \frac{\eta_0}{1 + \left(\frac{\eta_0 \dot{\gamma}}{\tau^*}\right)^{1-n}} \qquad \textbf{(2-16)}$$

$$\eta_0 = \lim_{\dot{\gamma} \to 0} \eta(\dot{\gamma})$$

$$[\tau^*] = \text{Pa}$$

$$[n] = -$$

where η_0, n and τ^* are material constants.

To add temperature dependency to equation (2-16), η_0 can be expressed as a function of T based on an Arrhenius-type dependence [117]:

$$\eta_0(T) = S \exp\left(\frac{T_S}{T}\right) \qquad \textbf{(2-17)}$$

$$[S] = \text{Pa s}$$

$$[T_S, T] = {}^\circ\text{C}$$

where T_S and S are material constants. Hereby, T_S is a measure of the materials temperature sensivity.

2.10 Demarcation to State of Science and Technology

The process of co-molding of CoFRTS with DicoFRTS is rarely reported in literature. Hereby, the discrepancy between fundamental research

and projects on component level is remarkable. Especially, if one takes into consideration that this material class is commercially available since several decades.

The here presented work investigates the process of co-molding on different levels of complexity. This enables for the first time fundamental understanding of the key phenomena and their influence on the production of complex components. Furthermore, an alternative resin is introduced. This UPPH resin is rarely described in literature as well. There are no literature values describing the friction of an UPPH based prepreg to a mold. Due to two independent crosslinking reactions the resin provides a process window which is ideal for the first research hypothesis: the need of a chemical stable and high-viscous B-stage.

The second research hypothesis addresses the draping and fixation of the CoFRTS during co-molding. This is tackled by magnetic manipulation of the material. No publications are known describing this method for CoFRTS. Even more, fixation of CoFRTS during co-molding is only reported by staging of the CoFRTS [60], limiting flow of the DicoFRTS [18, 25] or both at the same time [19, 20]. While staging reduces the interfacial properties [60] and shows a narrow process window [20] the reduction of DicoFRTS flow takes away the materials main advantage: the great freedom of design.

The combination of the hybrid resin with a magnetic fixation concept is unique. An interdisciplinary approach is required to study and describe the phenomena during co-molding. Furthermore new characterization methods and material models are needed.

3 Material Development

The locally reinforcement of DicoFRTS with CoFRTS requires customized materials and new ways of processing. In particular, the matrix found in CoFRTS has to fulfill completely different requirements than the matrix of state-of-the-art DicoFRTS. Whereas formulations of the later optimize surface quality, paintability, flowability, flame retardancy, electrical insulation, filler content and/or density, the CoFRTS matrix formulation aims for a fixed position and alignment of the fibers during molding, adequate impregnation of high fiber volume fractions, heat resistance and excellent mechanical properties.

3.1 The Ideal CoFRTS Material

The ideal CoFRTS material shows sufficient stiffness during co-molding with DicoFRTS to prevent deformation and misalignment. The impact of DicoFRTS flow on the tensile strength of the CoDicoFRTS specimen is shown in Figure 3.1. Here, commercially available materials (*AMC-8593* and *AMC-8595* from *Quantum Composites*) are stacked and compression molded to three different types of plates: type 1 consists of five layers of DicoFRTS, molded with 50 % mold coverage under one-dimensional flow; type 2 consists of four CoFRTS sheets faced with one DicoFRTS of 50 % coverage on each side; type 3 consists of two layers of CoFRTS with facing DicoFRTS. For all plates, 0 ° is both, the direction of material flow and the direction of the CoFRTS fibers. The mold temperature is 145 °C; the final pressure is 85 bar. The specimen is prepared by water jet cutting and the testing is performed according DIN EN ISO 527-4 [118].
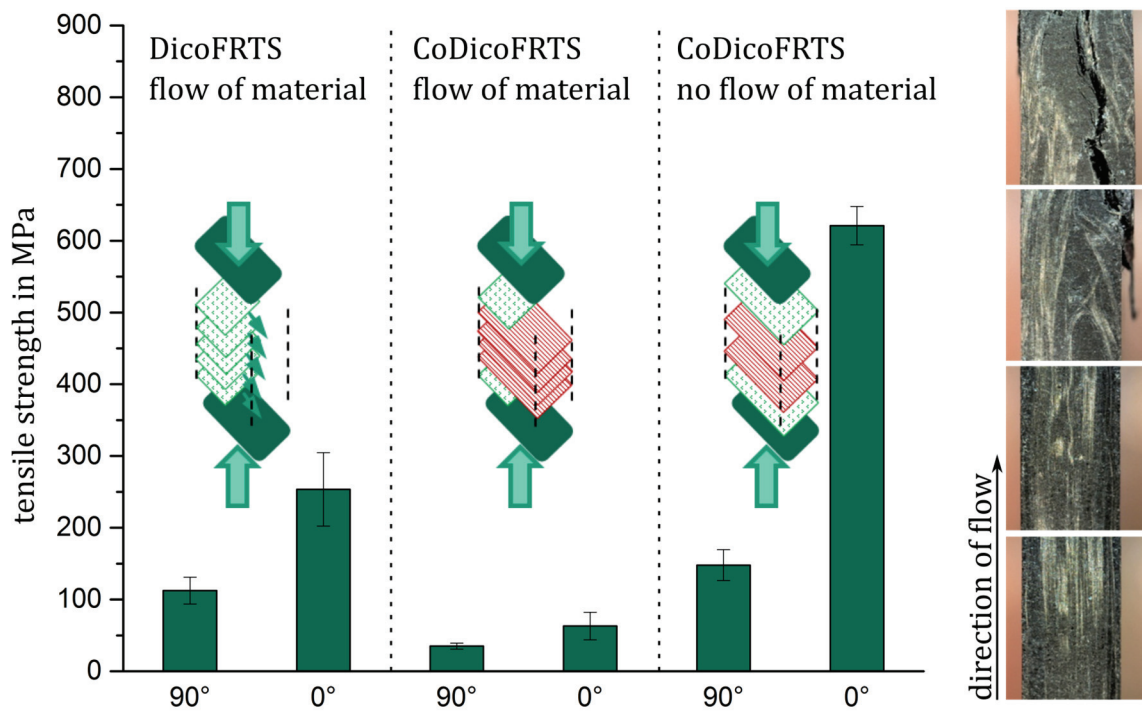
Figure 3.1: **Tensile strength as a function of layup and flow (*left*)**
Crack path of flown CoDicoFRTS 0° type 2 specimen (*right*)

The tensile strength for type 1 plates is inhomogeneous, due to fiber reorientation during flow. Type 2 plates achieve only a small fraction of their theoretical tensile strength. In fact, the continuous-fibers weaken the CoDicoFRTS, since the flowing DicoFRTS destroys the alignment of the CoFRTS. The continuous-fibers are forced into a turbulent and waved structure (compare to Figure 3.1, *right*). The crack propagates along those deformed wavy continuous fibers through the soft matrix. This results in poor tensile strength. Type 3 plates demonstrate the potential of CoDicoFRTS. While they are as strong as pure DicoFRTS (type 1) in 90° direction, they are almost 2.5 times as strong in the 0° direction. Moreover, the standard deviation in type 3 samples is smaller.

It is obvious, that for state-of-the-art resin systems a reinforcing effect can only be achieved by eliminating flow inside the mold. As DicoFRTS is known for its superior design freedom and capability of functional integration this limitation is not acceptable. When it comes down to local reinforcements the CoFRTS has to be fixed inside the mold to

prevent the material from displacement. This can be achieved by customizing the matrix of the CoFRTS.

The viscosity profiles of state-of-the-art MgO thickened UP or VE resins are optimized to produce cost effective highly filled GF-DicoFRTS with good flowability while molding (see Figure 3.2, a). However, for the production of CoFRTS those matrices are inappropriate because of their unsuitable viscosity profile.

The ideal matrix for the processing of CoFRTS delivers sufficient stiffness to the semi-finished material during co-molding with DicoFRTS to prevent the reinforcement fibers from misalignment. Thus, apart from mechanical properties, the most important characteristic of a matrix is its viscosity during the corresponding process steps (see Figure 3.2, b):

- To apply a homogenous and stable matrix film on the carrier foil a certain viscosity level is needed. At the moment the resin gets in contact with the fibers, the viscosity should be as low as possible to minimize the resistance against impregnation of the fiber by capillary forces. State-of-the-art matrices show a high initial viscosity, which is further increasing while applying and processing the matrix at the flat conveyor plant.
- Thickening usually takes several days resulting in a viscosity level of $\sim 10^5$ Pa s [9, 31]. A higher viscosity level of the semi-finished CoFRTS would be beneficial to the handling before molding. The very long thickening time inhibits from direct processing and makes quality assurance more difficult.
- The most important factor of influence is the viscosity drop of the matrix when placed in the hot mold before the radical polymerization dominates. MgO-thickened materials show a pronounced viscosity drop as this thickening mechanism is partly reversible under the influence of temperature [119, 120]. Hereby, the material gets so soft, that relatively small forces will lead to deformation and misalignment of the continuous-fibers, thereby compromising their reinforcing potential. Thus, a formulation is needed, which is not showing this decrease in viscosity during molding.

- For the production of geometries of higher complexity, a process window has to be found allowing to drape the CoFRTS (compare Figure 3.2, c).
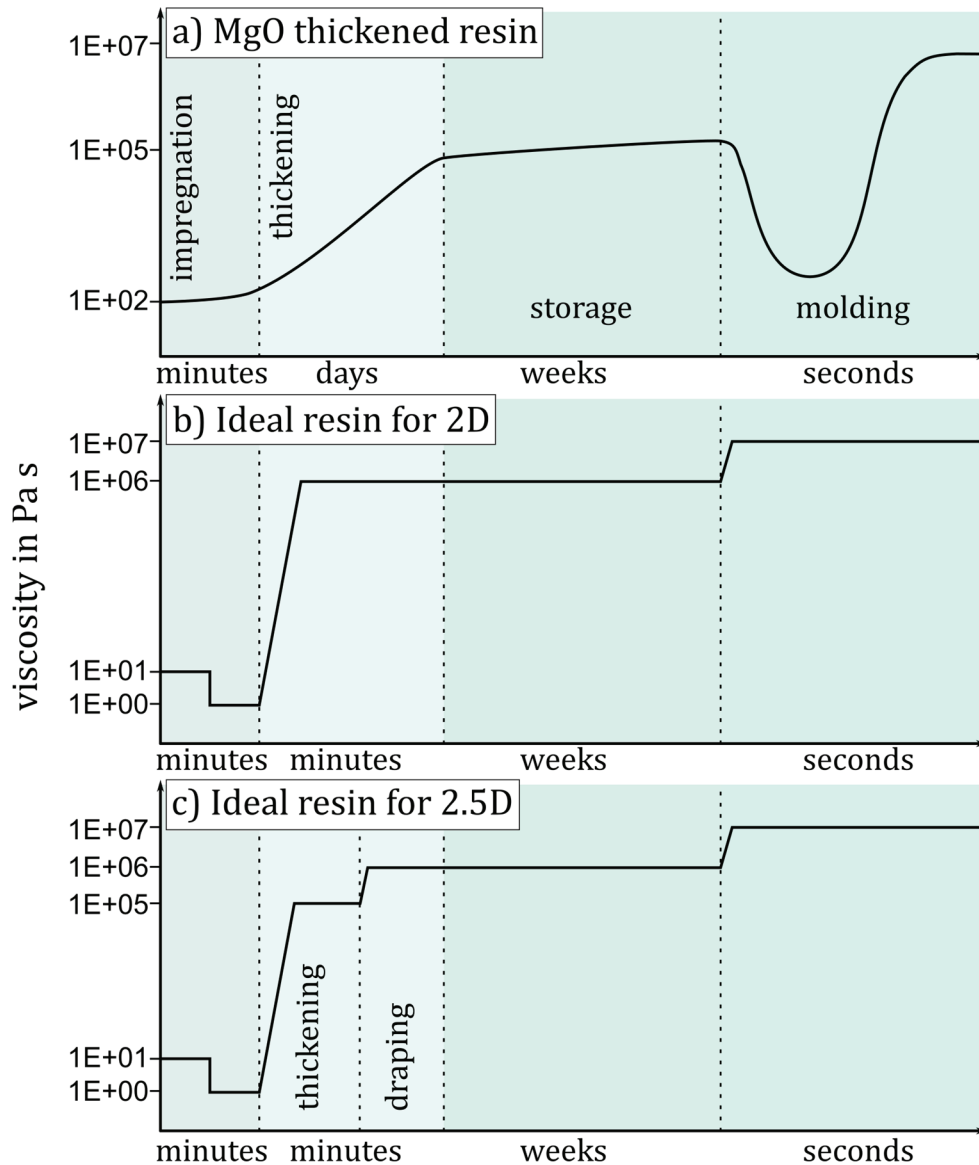
Figure 3.2: **Process steps and corresponding schematic resin viscosity**
a) Conventional MgO thickened SMC resin, according to [26]
b) Ideal resin viscosity for 2 dimensional CoFRTS
c) Ideal resin viscosity for 2.5 dimensional CoFRTS

The following sections will focus on the formualtion development of an alternative matrix for CoFRTS. The aim is to allow flow of the DicoFRTS inside the mold and to provide a fixation concept for very local reinforcements in CoDicoFRTS production.

3.2 The Ideal Fibers for CoDicoFRTS

For structural lightweight components, as considered here, glass and carbon fibers are of interest, because of their high specific mechanical properties [11]. Furthermore, the ideal fiber to reinforce the matrix must have an appropriate price to allow for cost efficient mass production.

Compared to steel, textile glass fibers are characterized by high tensile strength, low density [14] and medium stiffness at low costs [11]. They are the ideal raw material for the production of DicoFRTS components. Because of its flowability, the material is less dependent on the fibers stiffness. A design of corrugations and ribs achieves high geometrical stiffness of the structure. Furthermore the DicoFRTS can be used to integrate inlays, functions and to form complex shapes.

Carbon fibers, on the contrary, are showing very high stiffness in fiber direction at very low density [14]. However, their cost per kilogram is between 10 to 40 times higher than for glass fibers [9]. Thus, their application in mass production has to be limited to highly loaded areas or sections of small installation space – in other words to structural areas, to which the high stiffness inherent in the material is indispensable. Yet, the use of multifilament carbon fiber yarns of high yarn fineness, called heavy tows [14], has the potential to reduce raw material costs [121] and processing costs by increased material throughput.

The concept of co-molding enables the combination of these two fiber types in a cost effective way. Furthermore the ongoing improvements and production expansion of carbon fiber heavy tows [63, 121, 122] offer the chance to introduce thoroughgoing lightweight design in mass production. Both points are key factors for the success of the CoDicoFRP material class.

3.3 Physical Manipulation by Means of Magnetic Fields

To enable physical manipulation of the CoFRTS ferromagnetic or ferrimagnetic substances can be added to the thermosets matrix. The influence of such particles on the manufacturing process is examined within this section. Finally, a particle type is found which is compatible to the manufacturing process.

3.3.1 Comparison of Ferromagnetic and Ferrimagnetic Particles

In the context of processing the substance needs to meet the following requirements:

- Ability for accurate dosing
- Chemical and thermal stability
- No influence on crosslinking reaction of the thermoset
- Homogenous dispersability
- Stable dispersion within the resin

The particles of interest show significant higher density than common fibers or resin system. Furthermore, an added particle could act as a defect inside the FRP. Therefore, and in the context of structural lightweight design, additional properties are needed to ensure good mechanical properties of the material:

- Small size of particles
- High specific magnetic permeability

Within this framework eight substances are considered. Their product names and corresponding data-sheet information are listed in Table 3.1. To determine the particles best suited for processing of CoFRTS, a test stand is designed and constructed according to Figure 3.3. Hereby, the particles to be investigated are dissolved (dissolver type *5BCu2-042* by *VMA-Getzmann*) in a bucket of UP resin (*PALAPREG PREMIUM G 22-01 LE* by *DSM)*. The total weight of the mixture is set to 200 g and kept constant for all tests. The bucket is placed on a solid state magnet

and the maximum force peak to separate bucket from magnet (pull-off force) is measured five times in a row. Then, the force peaks are adjusted by the weight force of the setup and plotted depending to the weight fraction of the ferromagnetic or ferrimagnetic substance. Furthermore the test procedure is repeated after seven minutes, as the processing of the mixture to CoFRTS will take five to ten minutes. The resulting absolute pull-off force in relation to particle content diagrams can be found in Figure 3.4. Here each measurement point is shown with the corresponding standard deviation. However, the deviation is too small to be visible for some measurements.

Table 3.1:   Ferro- and ferrimagnetic particles for further evaluation

Product name	Molecular formula	Density in g/cm^3	Avg. grain size in µm	B_R in mT	H_C in kA/m
Diafe 5000	Fe	7.8	5		
Diafe 6000	Fe	7.8	4-7		
Diafe 7500	Fe	7.8	≤75		
SF-500	$SrFe_{12}O_{19}$	5.11	1.40	196	123
OP-56	$SrFe_{12}O_{19}$	5.11	1.05	190	130
Maniperm S17	$SrFe_{12}O_{19}$	5.1	>20	164	104
Maniperm S19	$SrFe_{12}O_{19}$	5.0	>20	162	100
Bayferrox 318m	Fe_3O_4	4.6	0.2		
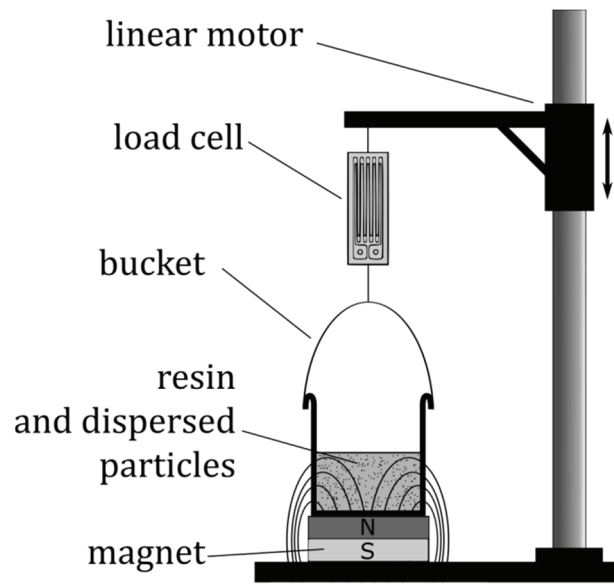
Figure 3.3: **Test stand to determine specific attraction force and dispersion stability of ferromagnetic and ferrimagnetic materials**
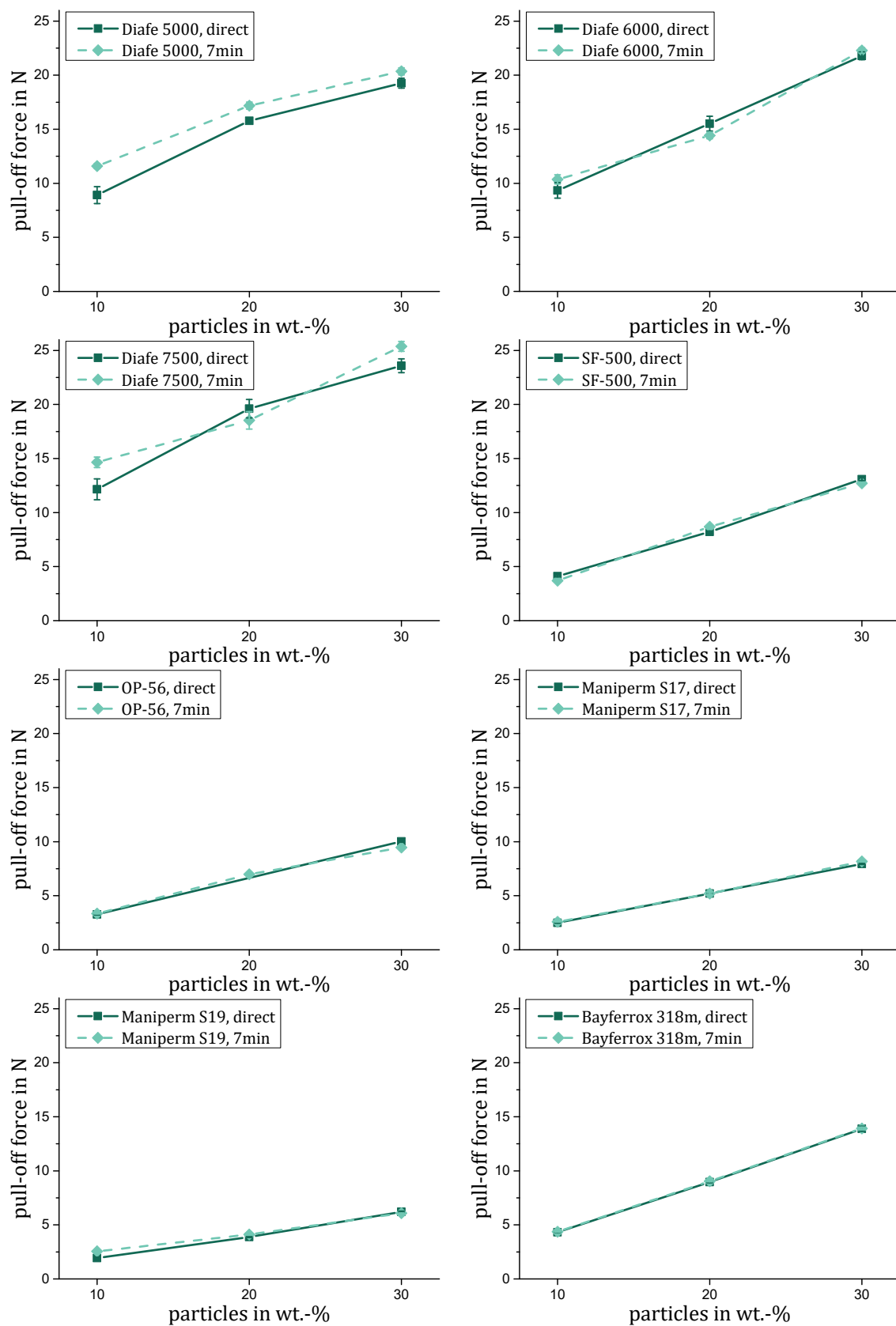
Figure 3.4:   Pull-off forces in relation to particle content

To compare the particles suitability for the processing of CoFRTS, characteristic values can be calculated from the curves shown in Figure 3.4. Each value is an indicator for a specific requirement:

- **Homogenous dispersability:** Gudmundsson et al. [123] report of a near linear dependency of saturation magnetization to magnetic medium content. A linear approximation of the measuring points generated directly after mixing enables to calculate the intersection of this straight line with the y-axis and the corresponding standard deviation. For homogeneous dispersed particles the linear approximated line should start at the origin. Consequently the y-axis intersection should be equal to zero. The discrepancy to this value is a measure of the dispersion quality.
- **High specific permeability:** The pitch of the linear approximation and the absolute value of the pull-off force are measures of the specific permeability of the mixture. The higher these values are the higher is the specific permeability.
- **Stable dispersion with resin:** By calculating the discrepancy of the pull-off force directly after mixing from the force needed after seven minutes a measure for the dispersion stability is found. In an unstable dispersion the particles will separate from the resin to be found either at the bottom of the bucket or at the top of the resin. This will result in a higher pull-off force for the first case or in a lower force for the second case. For a stable dispersion the force will be constant and consequently the discrepancy should be equal to zero.

Figure 3.5 displays these characteristic values for all investigated substances. All Diafe materials show a high straight line pitch. This could either be based on a high permeability of the substance or on inhomogeneous dispersability. However, the high value for "intersection with y-axis" indicates inhomogeneous dispersability. *Diafe 6000* material behaves slightly different than the other Diafe materials. It shows high pitch, too, but the standard deviation of all values is low and the dispersion seems to be very stable. Unfortunately this material is no long-

er in production. All other materials showed better results for the process related parameters but lower values for the specific permeability.
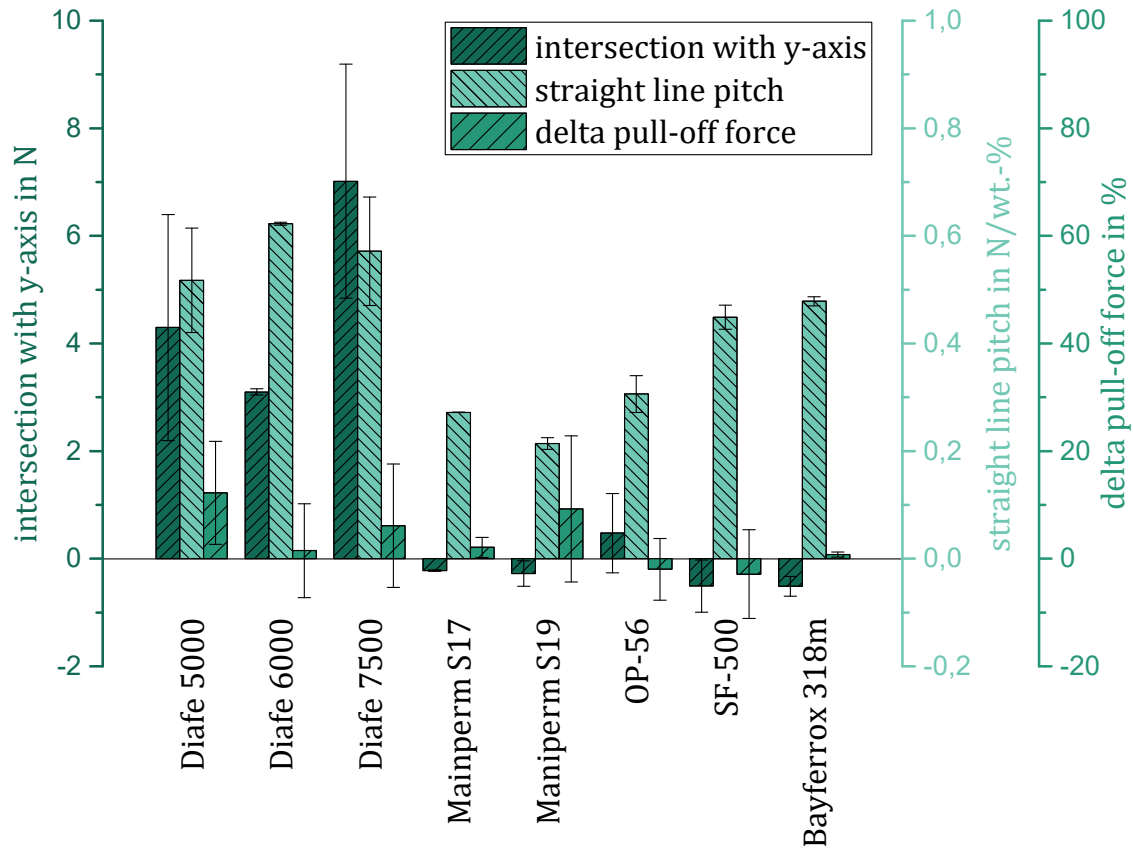
Figure 3.5: **Characteristic values of mixtures to evaluate suitability for CoFRTS manufacturing**

A scanning electron microscope (SEM) is used to evaluate the particles' size and shape of ferromagnetic and ferrimagnetic particles which differ in their molecular formula (see Figure 3.6). The *Diafe 5000* material shows a spherical shape at a size of some microns. Particles of *Maniperm S17* have a cuboid shape and single particles are smaller than the 20 μm specified in the data sheet. Furthermore the material tends to agglomerate. The *SF-500* material consists of platelets with a diameter of around 1 μm. *Bayferrox 318m* shows spherical particles with a diameter in the nanometer scale and a tendency for agglomeration.
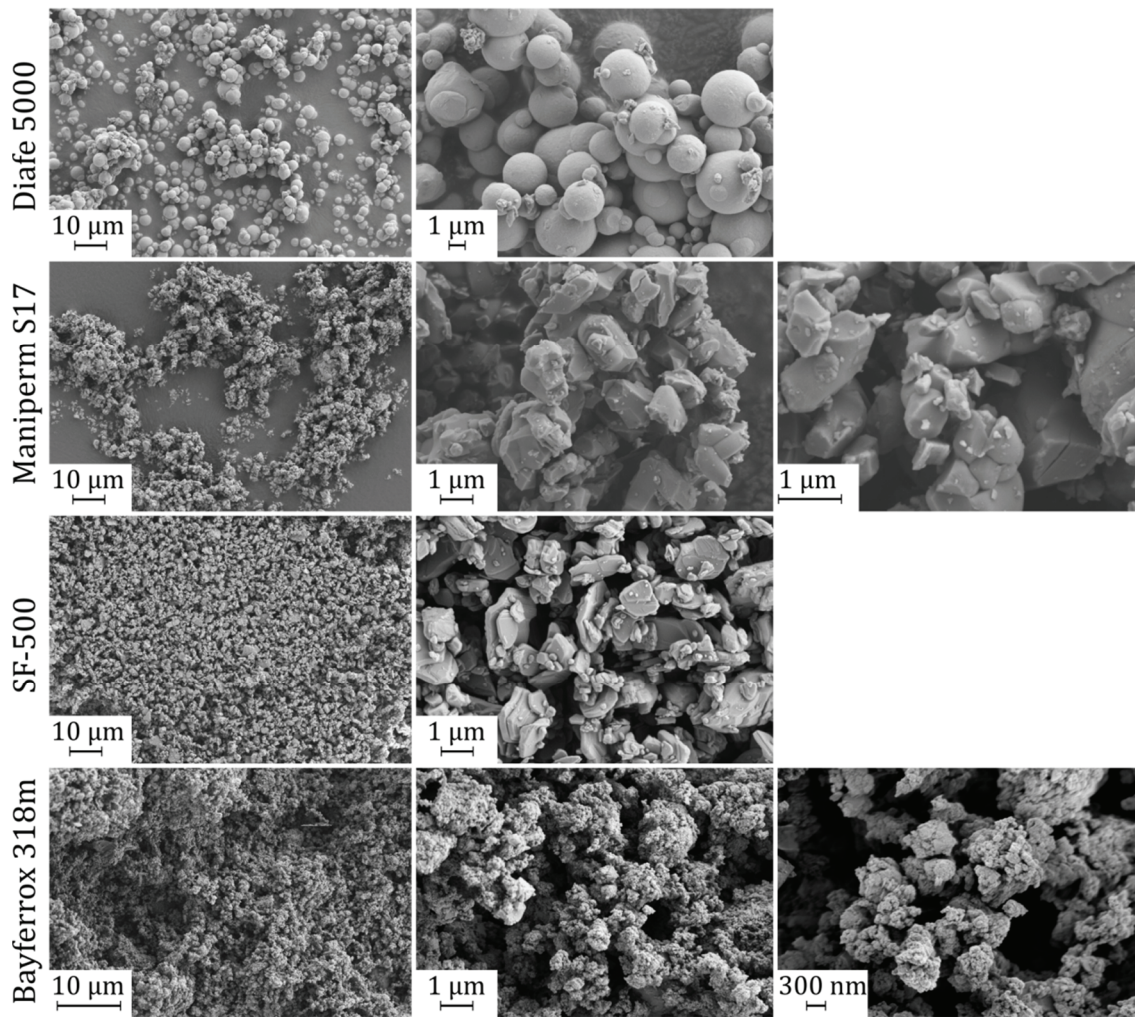
Figure 3.6:   SEM images of ferromagnetic and ferrimagnetic particles

The particle's radius has a large influence on the suspension's stability, if there is a difference in density between the dispersed particles and the medium [124]. For a small particle radius the Brownian diffusion is able to overcome the effect of sedimentation induced by the gravity force. This applies, if the following condition is fulfilled [125]:

$$k_B T > \frac{4}{3} \pi r^3 \Delta \rho g h \qquad \textbf{(3-1)}$$

$$k_B = 1.38064852 \ 10^{-23} \ \text{J/K, according to [126]}$$

$$[T] = K$$

$$[r, h] = \text{m}$$

$$[\Delta\rho] = \text{kg/m}^3$$

$$\text{g} = 9.81 \text{ m/s}^2$$

where k_B is the Boltzmann constant, T is the absolute Temperature, r is the particle radius, $\Delta\rho$ ist the density difference between particle and medium, g is the acceleration due to gravity and h is the height of the container.

If equation (3-1) is not valid the gravitational forces are dominant and will lead to a sedimentation rate v according to Stoke's law [125, 127]:

$$v = \frac{2r^2\Delta\rho\text{g}}{9\eta} \qquad\qquad \textbf{(3-2)}$$

$$[v_0] = \text{m/s}$$

$$[\eta] = \text{Pa s}$$

where η ist the viscosity of the medium.

Using the values of Table 3.1 in combination with an absolute temperature of 293 K, a resin density of 1050 kg/m³ and a container height of 0.03 m, equation (3-1) is valid for the *Bayferrox 318* material, but not for *DIAFE 5000* material. The reason is the higher particle size and the higher density ratio of the *DIAFE 5000* material. Thus, the Brownian diffusion for a suspension of *Bayferrox 318* is higher than the gravity force and no sedimentation occurs. According to the measurement results shown in Figure 3.5, there is also no sedimentation when exposed to an additional force induced by the magnetic field.

In contrast, particles of *DIAFE 5000* material will sediment according to equation (3-2), due to gravity. The sedimentation rate is about $2 \cdot 10^{-18}$ m/s when dissolved in a resin of $\eta = 900 \cdot 10^{-3}$ Pa s.

For further investigations the most promising material is chosen with *Bayferrox 318m*. The magnetite delivers best results in terms of processing. It shows a homogeneous and stable dispersability at a high

straight line pitch. Its spherical particle shape is beneficial to achieve low viscosity levels of the particle/resin mixture. This is essential for adequate fiber impregnation, when it comes to high fiber volume contents. Also *Bayferrox 318m* shows a homogeneous and stable dispersability at a high straight line pitch. However, the absolute values of the pull-off force are found in the midrange of the investigated materials, whereas the specific permeability is best for *Diafe 6000*. Unfortunately this material is no longer in production.

3.3.2 Characterization of Magnetite

For the processing of CoFRTS the chosen material has to be further characterized. The molecular formula of *Bayferrox 318m* (supplied by *Lanxess AG*) is Fe_3O_4, which is mineral magnetite. It is chemically stable as the iron is already oxidized. Figure 3.7 shows magnetite's molecular structure and the position, orientation and value of the single magnetic spin moments. Hereby, the Bohr magneton μ_B is a physical constant and describes the magnetic moment of an electron. As the spin moments are antiparallel and of different value, they cannot compensate each other. Thus, magnetite is a ferrimagnetic material.
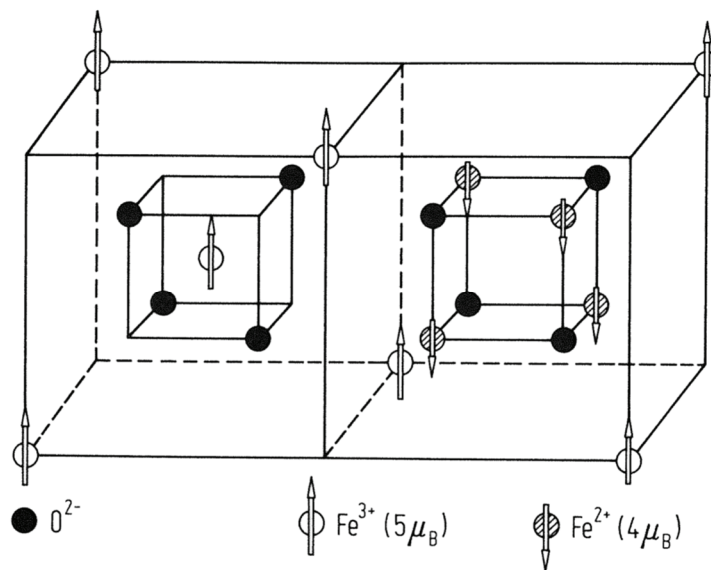
Figure 3.7: **Molecular structure and spin structure of Fe_3O_4 [84]**

The magnetic properties of a FRP to be manufactured in future times are dependent on volume percentage (vol.-%) φ of magnetic particles inside the material. The dosing during mixing of the individual components is done gravimetrically. Thus, the density of magnetite is needed to calculate its volume fraction. Also the particles' volume is needed to characterize its magnetic properties. As the bulk density of powders differs from its particle density a helium-pyknometer is used for measurement. Hereby, the density is measured by the help of the ideal gas law and the known weight of the sample. The device (*Pycnomatic ATC* by *Porotec* and *Thermo Fisher*) delivers an average value of $\rho = 4.459 \ \frac{\text{g}}{\text{cm}^3}$ at $T = 20\,°\text{C}$.

As basis for the simulation of magnetic fields magnetization curves are needed. Literature values are rare. In most cases only a saturation polarization J_s is mentioned. So Steinmetz and Hayden [128] report $J_s = 0.47 - 0.59\,\text{T}$, Svobada [129] reports $J_s = 0.55 - 0.61\,\text{T}$ and Rosensweig [130] publishes $J_s = 0.56\,\text{T}$ for magnetite. As the magnetization shows a strongly nonlinear behavior those values are not sufficient. To measure this characteristic a vibrating sample magnetometer (VSM) can be used. Within [131] magnetization curves of magnetite are shown generated by the help of an VSM (type *7404* by *Lakeshore*). But the measured magnetic polarization saturation J_s is smaller than 0.2 T. This differs strongly from the reported values. The discrepancy is based on a failure of the volume used to transform the measured magnetic moment of the VSM into magnetization. Here the volume of the sample chamber was used instead of the volume of the sample itself. As magnetite in powder form has significant lower bulk density than particle density, measurements of [131] cannot be used.

Thus, new measurements of the magnetite *Bayferrox 318m* have to be initiated, ideally temperature dependent. The available VSM of the type *PPMS EverCool II* by *LOT-QuantumDesign GmbH,* located at their branch in Darmstadt, is equipped with superconducting electromagnets at a temperature lower than 4.2 K. Yet, the sample can be heated up to 400 K which corresponds to 127 °C, rounded. Thus, the VSM is able to

measure temperature and magnetic field dependent magnetic moments. Those can be converted into curves of the magnetic flux B and polarization J. As processing of the FRP is done at elevated temperatures and the magnetic properties of magnetite are dependent thereof, measurements at 80 °C and 127 °C were performed. Figure 3.8 shows on the left side the flux density B, the polarization J and their difference at $T = 80$ °C. Here B gives information about the actual flux density in the sample, $B - J$ is the theoretical flux density present in free space without any sample. Thus, J describes the flux density, which the magnetite adds to the measuring volume und is therefore ideal to characterize technical magnetic materials. Figure 3.8 (right) shows magnetic polarization curves for two temperatures. At $T = 80$ °C a saturation of $J_s \approx 0.39$ T and at 127 °C a saturation of $J_s \approx 0.37$ T is measured. The expected temperature dependency is therefore confirmed. As the literature values were measured at room temperature the present curves are plausible.
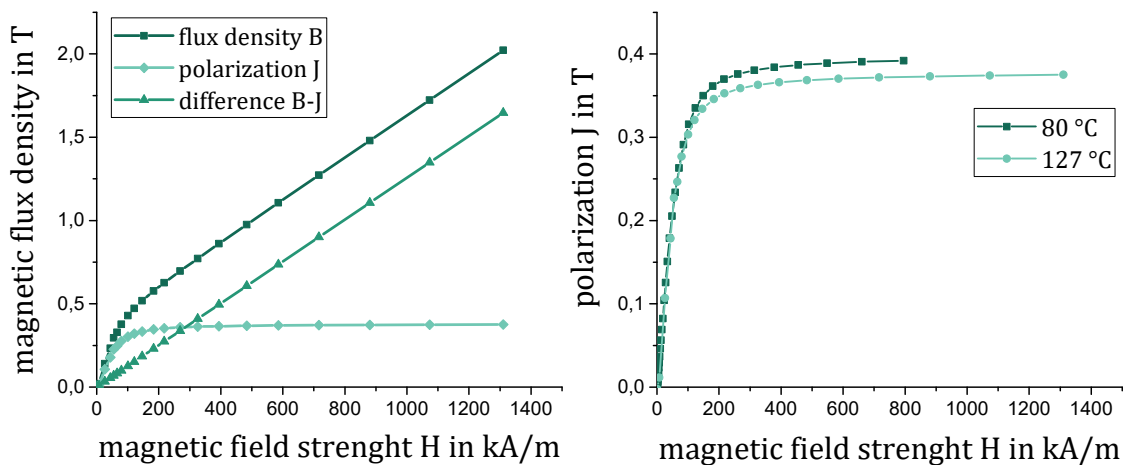
Figure 3.8: **Magnetic properties of Bayferrox 318m**
left: Flux density, polarization and their difference at 127 °C
right: Polarization at 80 and 127 °C

The final CoFRTS will contain only a fraction of magnetite. The magnetic properties of the entire compound can be calculated according to [123] by multiplication of the polarization curves shown in Figure 3.8 (right) with the actual vol. $-\%$ of magnetite φ. In the following this will be called the volume based modell (ModV):

$$J_{\text{ModV}}(\varphi, H) = \varphi\, J(\varphi = 100\%, H) \qquad\qquad \textbf{(3-3)}$$

$$[\varphi] = \text{vol.} -\%$$

This linear model is only valid, if the other components of the composite behave neutral in magnetic fields. This is given for the polymer as $\mu_r \approx 1$ [132]. The CF-fibers behave diamagnetic and $\mu_r = f(H)$ is furthermore strongly dependent from production (precursor type and heat treatment [90]) as well as the orientation of the graphite layers [89]. However, compared to the ferrimagnetic magnetite this influence on the total magnetic properties of the compound should be negligible small [133].

Another approach is the empiric model presented by D. J. Carlson in 2005, which is used to describe established magnetorheological (MR) fluids [134]:

$$J_{\text{CAR05}}(\varphi, H) = C_1 \varphi^{1.133}\left(1 - e^{(-C_2 \mu_0 H)}\right) \qquad\qquad \textbf{(3-4)}$$

$$[C_1] = \text{T}$$

$$[C_2] = \text{T}^{-1}$$

Values for C_1 and C_2 can be found by the help of a least-square error fit. For the polarization at a temperature of 127 °C, C_1 is 0.3701 T and C_2 is 12741.6813 T^{-1} at $\bar{R}^2$ of 99.4. The power of the magnetic particle content φ is constant and defined as 1.133 and therefore nonlinear.

In the interest of simplification, equation (3-3) will be used for the first dimensioning of the process. Later, to describe the forces acting during co-molding, an improved model will be presented.

3.4 Chemical Modification

Besides the physical modification of the matrix with magnetic fields, a formulation has to be found, which provides processing windows according to Figure 3.2.

This shall be achieved by applying an alternative thickening chemistry. This section introduces a 2-step-curing thermoset and describes the formulation development needed to manufacture CoFRTS.

3.4.1 Unsaturated-Polyester-Polyurethane-Hybrid resin

The 2-step-curing resin to be used is an Unsaturated-Polyester-Polyurethane-Hybrid (UPPH). The resin formulation is made of two main components A and B, which in turn consist of different chemicals:

Component A:
- (1) **Resin:** Polyester polyol dissolved in styrene (*Daron 41*, by *aliancys*)
- (2) **Water desiccant:**
  - (2.1) N-Butyl-2-(1-ethylpentyl)-1,3-oxazolidine (*Incozol 2*, by *Incorez*)
  - (2.2) Zeolite (*UOP L-Powder*, by *UOP*)
- (3) **Mold release agent:** *BYK-P 9085*, by *BYK*
- (4) **Inhibitor:** 10 % poly benzoquinone (pBQ) dissolved in methyl methacrylate (MMA)
- (5) **Accelerator:** Metal carboxylate (*Borchi Kat 0243*, by *borchers*)

Component B:
- (6) **Chain extender:** Di-isocyanate (MDI), (*Lupranat M 20 R*, by *BASF*)
- (7) **Initiator:**
  - (7.1) Organic peroxide (*Trigonox 117*, by *AkzoNobel*)
  - (7.2) Organic peroxide (*Peroxan BEC*, by *Pergan*)

Mixing component A with component B results in a low viscous liquid, which first reaction step will start to react immediately (see Figure 3.9). Only by using a heat stable initiator (7) the two reaction steps can be separated. Otherwise both reaction steps would occur in parallel.

The first reaction step is performed between the MDI (6) and hydroxyl functional groups of the resins backbone (1). The consequence is a

chain extension by urethane linkage showing a rubber-like B-stage. This condition is around one order of magnitude higher in viscosity than MgO thickened resins and enables to produce semi-finished CoFRTS with high stiffness. The reaction time can be shortened by introducing an accelerator (5) and elevated temperatures.

The second reaction is initiated by the organic peroxide (7) at even higher temperatures (90 °C to 110 °C). There crosslinking of the extended chains with styrene takes place. This radical polymerization results in a rigid and 3-dimesional cross-linked thermoset.
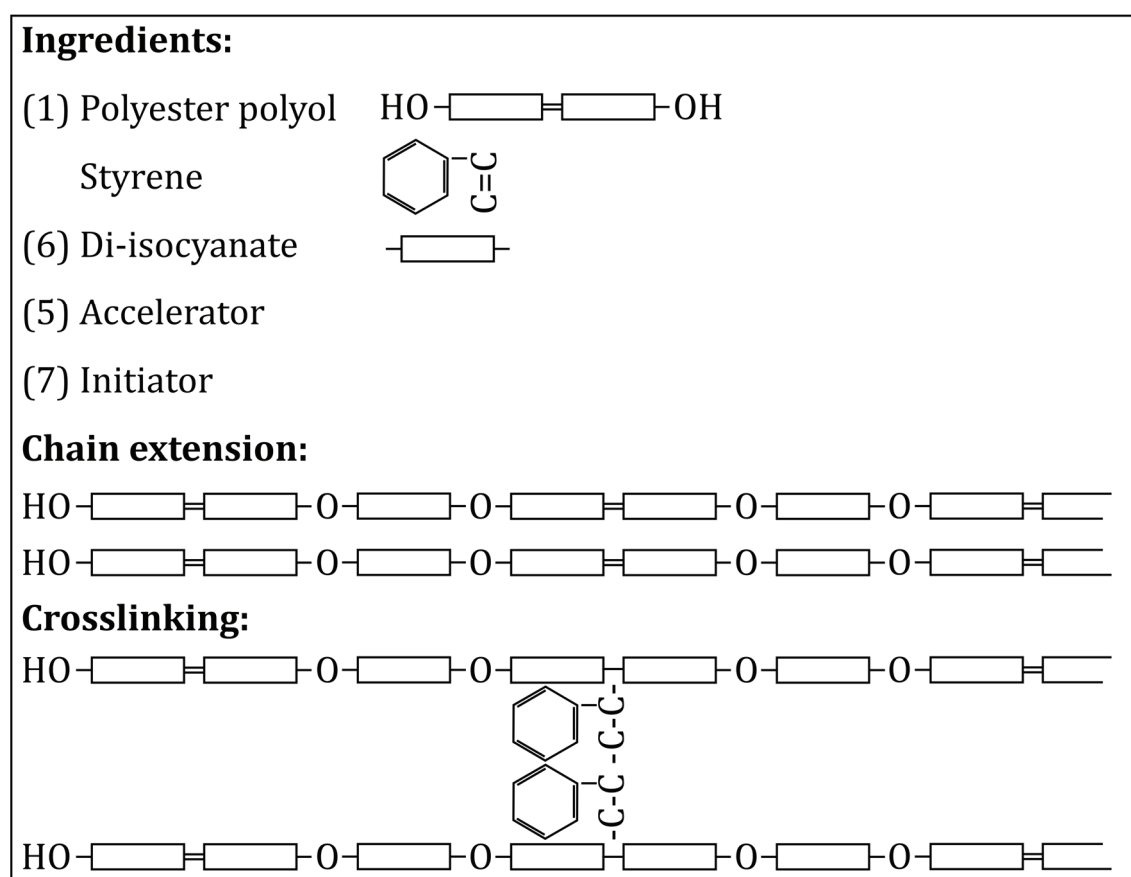
Figure 3.9:   UPPH chemistry

3.4.2 UPPH and Water

According to the data sheet [135] the resin contains up to $0.1\ wt. -\%$ of water. As Figure 3.10 shows isocyanate reacts in the presence of

water to instable carbamic acid. This rapidly loses carbon dioxide to form a primary amine [136]. Considering the low molecular mass of water compared to polyester polyol even a small amount of water will have substantial impact on the reaction sequence and the final polymer structure [137].

$$RNCO + H_2O \longrightarrow \left[R-\overset{H}{N}-\overset{O}{\underset{}{C}}-OH \right] \longrightarrow RNH_2 + CO_2$$
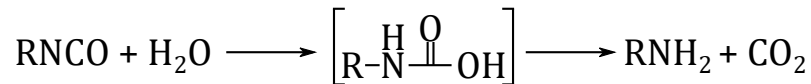
Figure 3.10: Reaction of isocyanate with water, according to [136]

The consequences of water for the process are accordingly:

- Formation of voids consisting of carbon dioxide within the UPPH
- Less urethane linkage resulting in reduced B-stage viscosity

To avoid this mechanism the water can be absorbed (*UOP L-Powder*) or chemically bonded (*Incozol 2*). To find the desiccant type and ratio best suited for the UPPH resin specimens of different formulations (shown in Table 3.2) are produced. The ingredients of the formulation are given in parts per hundred resin (phr). The preparation of the specimens is done according to the following sequence:

1. Mixing of the formulation at 300 rpm and below 30 °C with a dissolver type *5BCu2-042* by *VMA-Getzmann*
2. Casting the formulation into a form of 70 mm in diameter and 20 mm in height
3. Hardening at 100 °C for 12 h in an oven type *UT 6420* by *Heraeus GmbH*
4. Cutting of cross-section
5. Polishing of cross-section
6. Microscopy of cross-section

Table 3.2: **Formulations of different desiccants (in phr)**

	0	I_0.5	I_1	U_1	U_2.5	U_5
Daron 41	100	100	100	100	100	100
Incozol 2	0	.5	1	0	0	0
UOP L	0	0	0	1	2.5	5
pBQ 10%	.3	.3	.3	.3	.3	.3
Peroxan	1	1	1	1	1	1
MDI	25	25	25	25	25	25
BorchiKat	.2	.2	.2	.2	.2	.2

The resulting microscopy pictures are shown in Figure 3.11. The reference formulation without any desiccant exhibits a great number of blowholes and cracks. For an *Incozol 2* amount of 0.5 phr both, blowholes and cracks, are decreasing in number. For 1 phr there are no failures visible. However, *Incozol 2* affects an increase in viscosity with a high gradient already at mixing. Furthermore this behavior is not reproducible.

1 phr of *UOP-L* results in a cross-section with very few blowholes and without any cracks. Further increasing of the *UOP-L* amount eliminates the blowholes at the expense of a stronger tendency for the formation of cracks.

As a result of this investigation *UOP-L* is chosen as desiccant for the manufacturing of CoFRTS. Unless otherwise stated an amount of 1.5 phr will be used. *Incozol 2* seems to act as a catalyst for the first reaction step of the UPPH resin and is thereby not applicable.
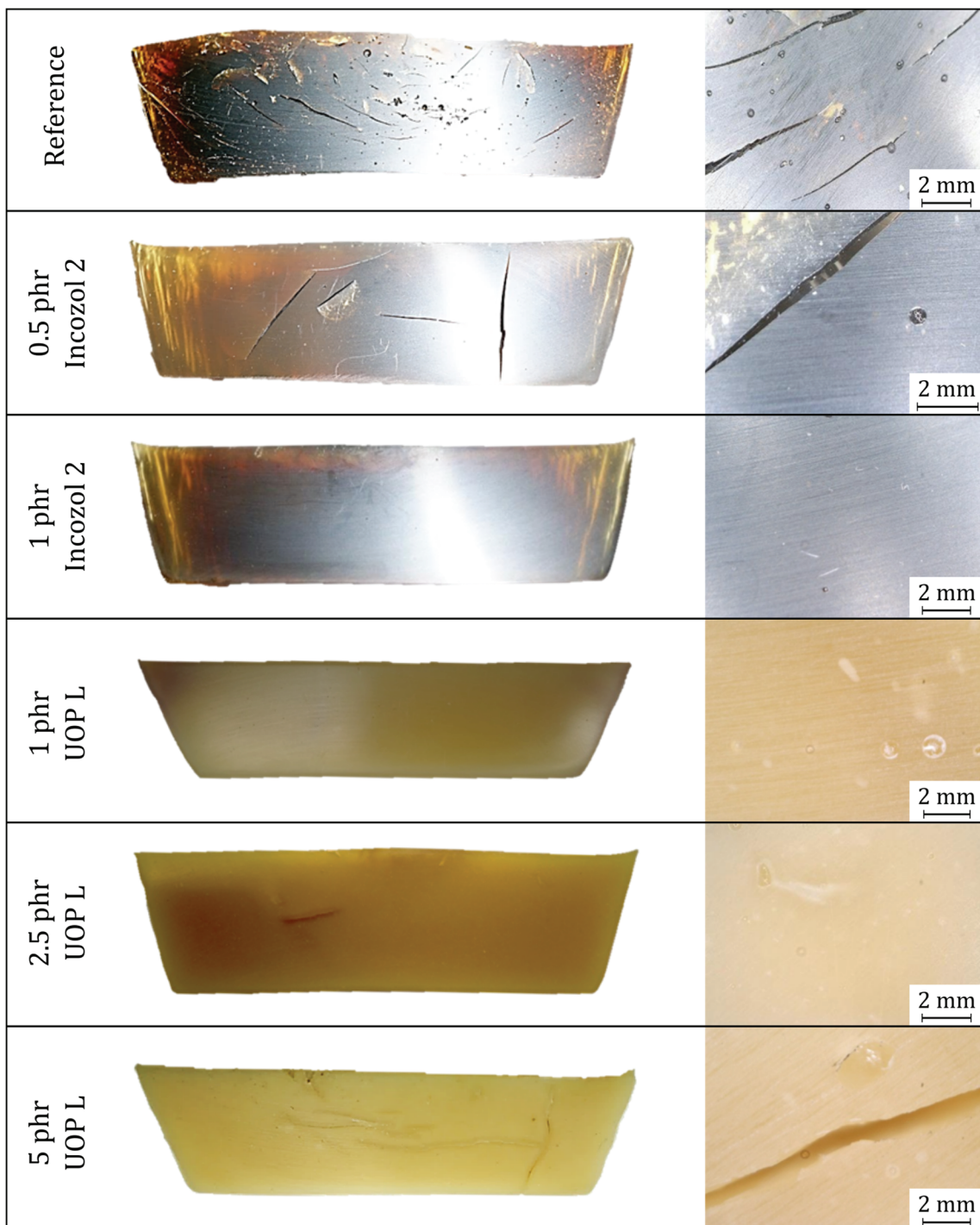
Figure 3.11: **Cross-sections of UPPH of different desiccants**

3.4.3 Viscosity of UPPH

Each process step needs a certain range of viscosity (compare Figure 3.2). The goal of the current section is to adjust the UPPH resin to these processing windows. Furthermore the influence of individual components on viscosity is of interest and hence investigated. For this purpose oscillation viscosity measurements are performed.

Experiment set-up and expectations:

Formulations according to Table 3.3 are mixed with a dissolver *5BCu2-042* by *VMA-Getzmann*. The components are added in the order they appear in the table. As the resin is highly reactive after mixed with the accelerator, the mixing is done directly beside the rheometer. The period between start of mixing with accelerator and start of the viscosity measurement is hereby fixed to 140 s.

Table 3.3:   Formulations for viscosity measurements (in phr)

	V2	V3	V5	V6	V7	V8	V9	V10	V11	V13
Daron 41	100	100	100	100	100	100	100	100	100	100
UOP L	1.5	1.5	1.5	1.5	1.5	1.5	1.5	1.5	3.5	1.5
pBQ 10%	.3	.3	-	.6	.3	.3	.3	.3	.6	.3
Peroxan	1	1	1	1	1	1	1	1	1	1
Bayferrox	-	-	-	-	-	-	37.5	75	37.5	-
MDI	25	25	25	25	25	20	25	25	25	25
BorchiKat	.15	-	.15	.15	.075	.15	.15	.15	.15	.15
Temp. profile	1	1	1	1	1	1	1	1	1	2

As rheometer a *MCR 501* by *Anton Paar* is used. The measurement method is set to oscillation at a constant frequency of 1 Hz. The temperature profiles are specified according to the requested viscosities and the operating range of the manufacturing lines at the single process steps (compare Figure 3.12, Table 8.1 and Table 8.2 in the appendix).
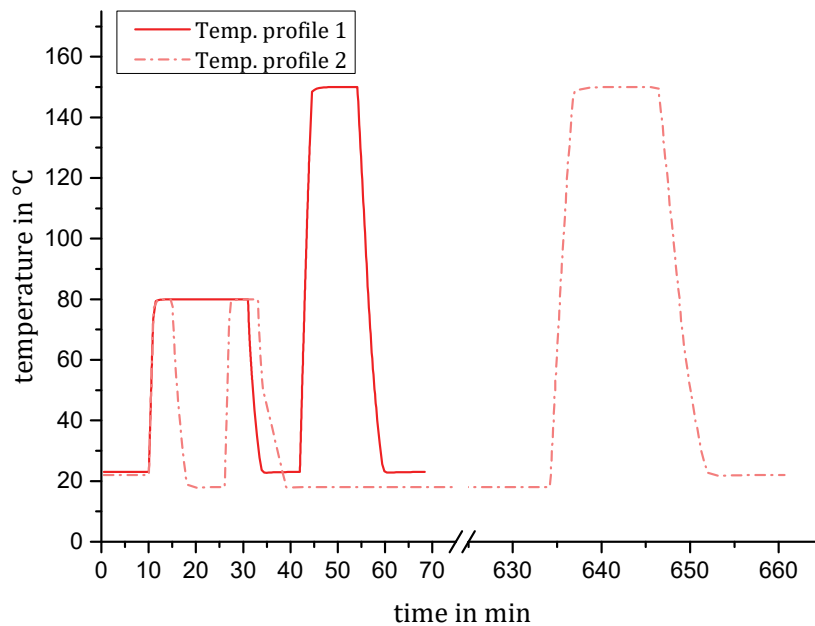
Figure 3.12: Temperature profiles for viscosity measurements

Temperature profile 1 is designed for the production of flat and single curved (2D) reinforcements:

- **$0 - 10$ min, RT:** This time window is needed to mix all components, to transfer the matrix to the flat conveyor plant and to apply a thin film of resin on the carrier foil. This is done at room temperature. Constant viscosity is beneficial for constant film height.
- **$10 - 31$ min, $80\,°\mathrm{C}$:** The temperature is raised for two reasons. Firstly the elevated temperature leads to a drop in viscosity because of higher mobility of the polymer chains. This supports the impregnation of the reinforcing fibers by means of capillary forces. Secondly temperature is accelerating the first reaction step to achieve a stable B-stage. As both effects occur simultaneously, but at different velocity, the temperature increase should be as fast as possible. A high heating rate results in a high drop of viscosity (see Figure 3.13).
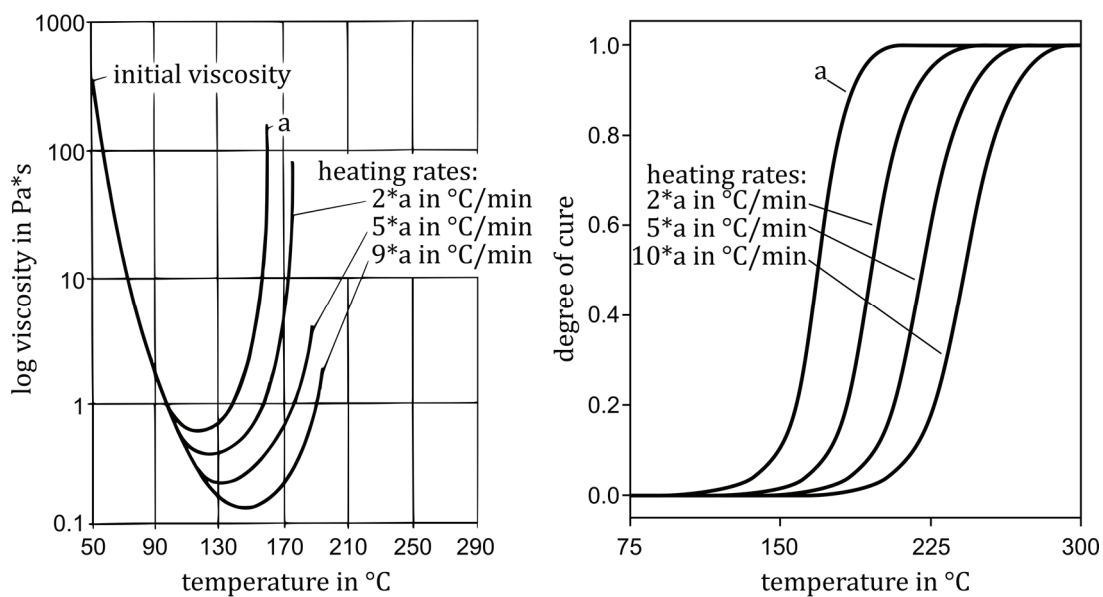
Figure 3.13: Heating rate dependency of thermoset resins
left: On viscosity, according to [138]
right: On degree of cure, according to [139]

- **31 − 41 min, RT:** The UPPH gets cooled down to room temperature again. The viscosity of the B-stage is measured, when the viscosity profile is showing a gradient near zero. In CoFRTS production cutting and handling operations can be done.

- **41 − 68 min, 150 °C:** The temperature is raised to 150 °C and hold constant for 10 min before cooled down to room temperature again. This simulates molding conditions of the CoFRTS, whereas the fast heating rate of thermal conduction in the mold is not fully realizable by the rheometer. Raising the temperature leads to increased polymer chain movability and radical polymerization at the same time. Thus, the viscosity profile is comparable to the process of B-staging, but higher in absolute values. However, a drop in viscosity will lead to a misalignment of the continuous-fibers during co-molding and therefore has to be minimized.

Temperature profile 2 is designed for the production of double curved reinforcements (2.5D). There is a need for an additional draping step in the process chain. Thus, there are differences compared to temperature profile 1:

- **10 − 15 min, 80 °C:** The first temperature increase is shortened compared to profile 1. It is intended to see, if there is the possibility to pause the first reaction step before complete B-staging of the UPPH resin.

- **15 − 26 min, 18 °C:** The aim is to achieve a CoFRTS, which is high viscous enough for handling and cutting, but flexible enough for the draping step. The process window therefore is ≈ 10 min in direct processing. To achieve more constant viscosity thereby the material is cooled down to 18 °C. This is equal to the temperature of the available permanent cooling circuit in the laboratories.

- **26 − 33 min, 80 °C:** The second heating phase is provided to complete the first reaction. This will be done at the draping-tool, which is intensive in invest and should therefore not be occupied for too long. The time needed to achieve the full B-stage should be short.

- **33 − 634 min, 18 °C:** This time is intended for storage of the reinforcement until molding. Constant viscosity is preferred.

Temperature profile 1 is used for experiments V2 to V12 and profile 2 is used for experiment V13. The average standard deviation of temperature profile 1 for the considered experiments is 0.19 °C at a maximum standard deviation of 0.57 °C. Thus, the profiles shown in Figure 3.12 are set as reference for the illustration of all measurement results. The following viscosity measurements are one-time measurements and were only repeated if the outcome was not plausible.

Accelerator:

BorchiKat 0243 is added as accelerator for the first reaction step. It shows high impact on the viscosity profile (see Figure 3.14).

Without accelerator (V3) the viscosity drops from 1.6 to 0.02 Pa s when exposed to 80 °C. The first reaction step is not completed during the first heating phase of 20 min. At 150 °C the viscosity drops again to 0.5 Pa s.

For a *BorchiKat* content of 0.075 phr (V7) the viscosity drops from 17 to 1.3 Pa s. The first reaction step is mostly done after 8 min, when

evaluated by using the tangent method [103]. The B-stage shows a final viscosity of $3.8 \cdot 10^5$ Pa s at room temperature.

Adding 0.15 phr of accelerator (V2) leads to a viscosity decrease from 93 to 6.7 Pa s. The B-stage is achieved after 5 min with a viscosity of $5.3 \cdot 10^5$ Pa s.

The behavior at molding conditions of V2 and V7 is similar. The viscosity drops to $1.4 \cdot 10^5$ Pa s, when exposed to 150 °C and the curing time is ≈ 7 min.
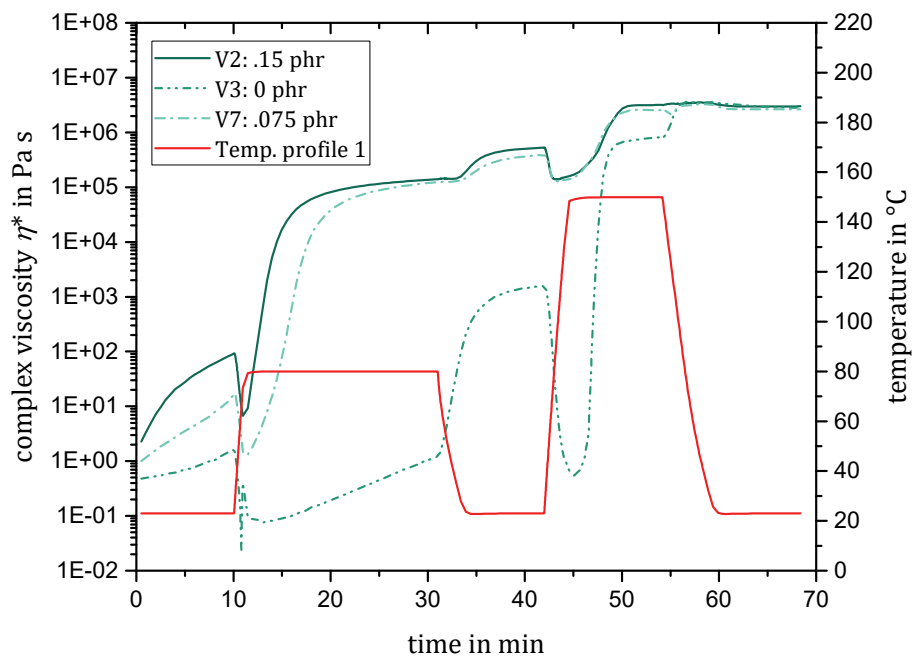
Figure 3.14: Influence of accelerator on viscosity

Chain extender:

Hydroxyl functional groups of the resins backbone and the MDI are forming the B-stage by chain extension. Therefore, the influence of MDI amount is limited to the first reaction step. When reducing its amount from 25 phr (V2) to 20 phr (V8), a shorter average chain length is achieved.

The initial viscosity of the formulation with reduced MDI amount is slightly lower than the reference formulation as MDI has a higher viscosity than the resin (see Figure 3.15). The drop from 38 to 2.4 Pa s in viscosity, when exposed to 80 °C, is therefore shifted, too. As fewer reaction partners are available for the first reaction step the B-staging occurs within 7 min compared to 5 min for V2. The final B-stage and drop at molding conditions are lower in viscosity as well: $2.4 \ 10^5$ and $0.85 \ 10^5$ Pa s compared to $5.3 \ 10^5$ and $1.4 \ 10^5$ Pa s.
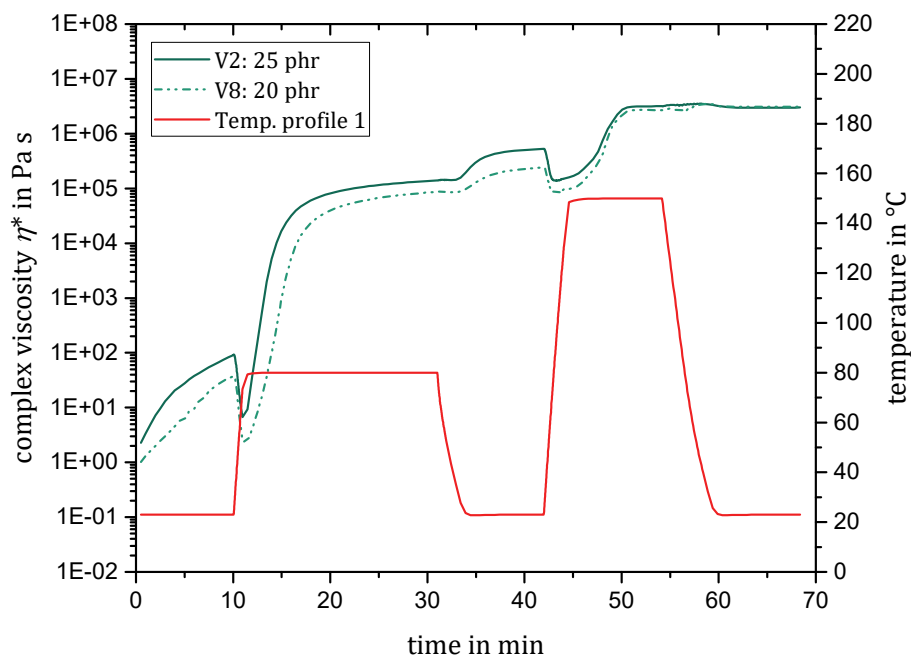
Figure 3.15: Influence of MDI on viscosity

Inhibitor:

pBQ is added as inhibitor of the radical polymerization to improve the materials storability. Figure 3.16 shows the expected increase in reaction time for higher pBQ ratios at molding conditions. Indeed it also indicates an influence on the first reaction step. The reaction time for B-staging increases from 5 to 8 min, when adding 0.6 phr instead of 0.3 phr of pBQ.
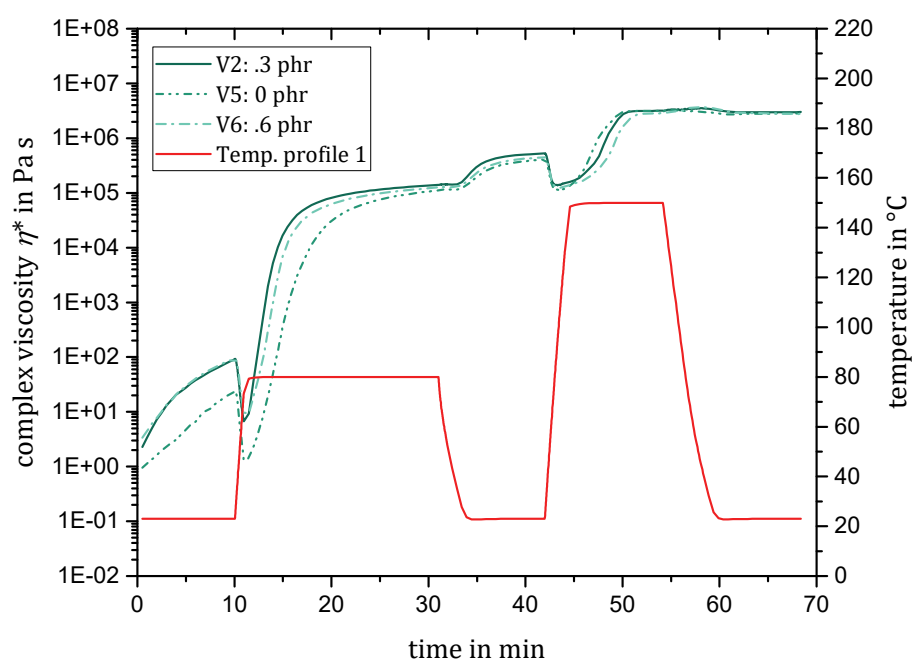
Figure 3.16: Influence of pBQ on viscosity

Magnetite:

When adding magnetite (*Bayferrox 318m*) to the UPPH resin, the B-staging behavior of the matrix is getting unreproducible. The cured samples show voids after the measurements. Thus, there is a strong suspicion, that the magnetite contains water, which is further reacting with the MDI at the loss of carbon dioxide. A measurement of the matrix viscosity in the presence of dispersed gas voids is not possible. Adjusting the formulation by an increased water desiccant amount the UPPH containing magnetite behaves like the reference formulation (see Figure 3.17, V2 and V11). However, it is showing a slightly higher initial viscosity (6 compared to 2 Pa s) as both, *UOP L* and *Bayferrox,* are additives in powder form.
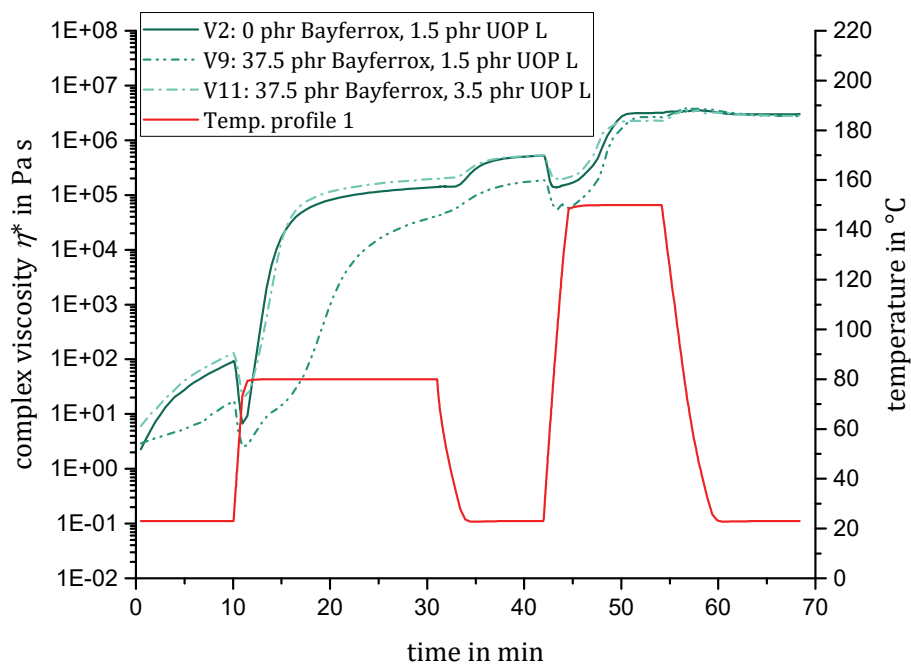
Figure 3.17: Influence of improved magnetite formulation on viscosity

Suitability for draping:

Figure 3.18 shows the influence of a change in the temperature profile on the viscosity. V2 and V13 are based on an identical formulation. By splitting the first heating phase and introducing a cooling phase, the first reaction step can be paused before completion, at least for the period of some minutes. This results in an UPPH resin viscosity of $0.43\ 10^5$ instead of $5.3\ 10^5$ Pa s for the fully completed B-stage. In this condition impregnated CoFRTS material should be stiff enough for cutting and handling and flexible enough for draping. Raising the temperature again leads to the same viscosity level than for temperature profile 1. The second reaction step can be fully separated from the first one as storage of the material for 10 hours at 18 °C does not lead to an increase in viscosity. The illustrated loss of viscosity over the storage period (70 min to 620 min) does not describe the material behavior but a loss in contact of the permanently oscillating plate to the sample
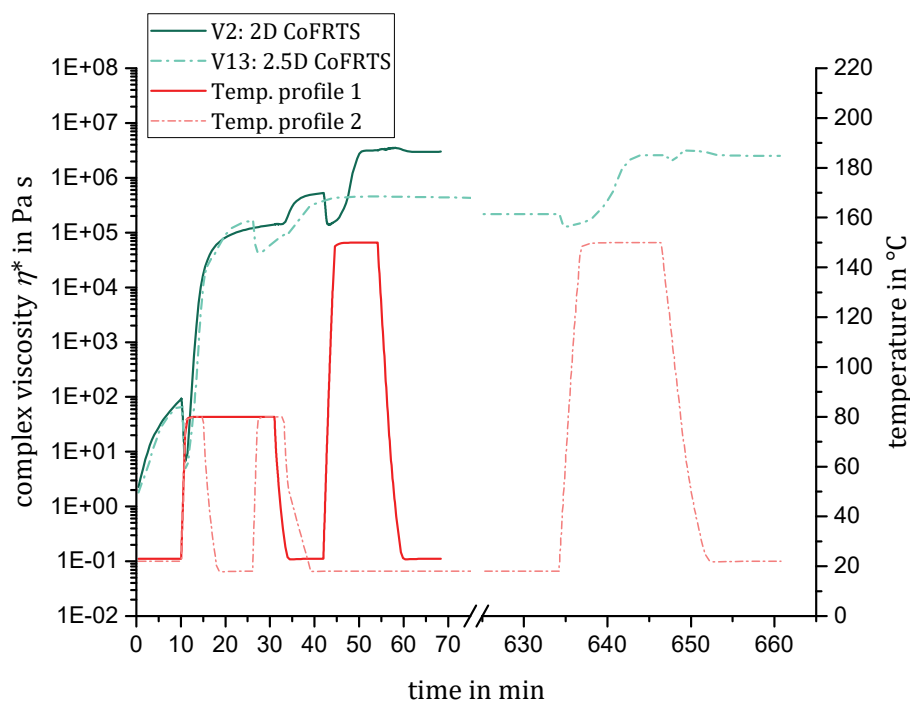
Figure 3.18: **Suitability of the UPPH for draping**

Conclusions:

Investigations at temperature profile 1 were made for the basic development of the matrix formulation in terms of the viscosity profile. Temperature profile 2 was used as validation of this development for the suitability of processing more complex reinforcements.

The major influence factor on the viscosity profile is the accelerator content. A high amount is leading to a fast reaction time of the polyurethane linkage, but also to a high viscosity within the process window intended for impregnation. 0.15 phr of *BorchiKat 0243* is considered as a suitable value for the production of CoFRTS. However, a reduction of the time period between mixing of components and impregnation as well as an increased heating rate is required for a sufficient impregnation of the fibers. This can be achieved by using a two-component equipment in order to apply the matrix on the line (see Chapter 4).

The supplier of *Daron 41* recommends a MDI content of 25 phr. A reduction by 5 phr results in a longer reaction time and a lower final viscosity level for the first reaction step. Thus, the recommended amount is chosen.

The inhibitor of the radical polymerization (pBQ) also affects the B-staging. However, an amount of 0.3 phr of the 10 % solution does not show a negative effect and is chosen as reference. The ability to provide a shelf-life of at least 10 hours of the B-staged matrix is demonstrated by Figure 3.18.

Despite of adding magnetite (*Bayferrox 318m*) to the formulation nearly the same viscosity profile can be achieved than for the pure UPPH resin. A possible acceleration of the chemical reactions by the iron oxide as mentioned in [140] has not been observed. Nevertheless the amount of water desiccant UOP L has to be adapted to the amount of magnetite according to the experimentally developed formula:

$$(UOP\ L\ addition) = \frac{4}{75}\ (Bayferrox\ 318m\ addition) + 1.5\ \text{phr}\ \textbf{(3-5)}$$

$$[UOP\ L\ addition] = \text{phr}$$

$$[Bayferrox\ 318m\ addition] = \text{phr}$$

Figure 3.19 shows storage modulus G', loss modulus G'' and loss factor $\tan\delta$ for the developed formulation V2. The gel point is reached after 2.5 min at 80 °C. After this point the elastic properties of the material are dominant and the impregnation of the fiber must already be completed. The material is now ready for cutting, handling and draping operations.
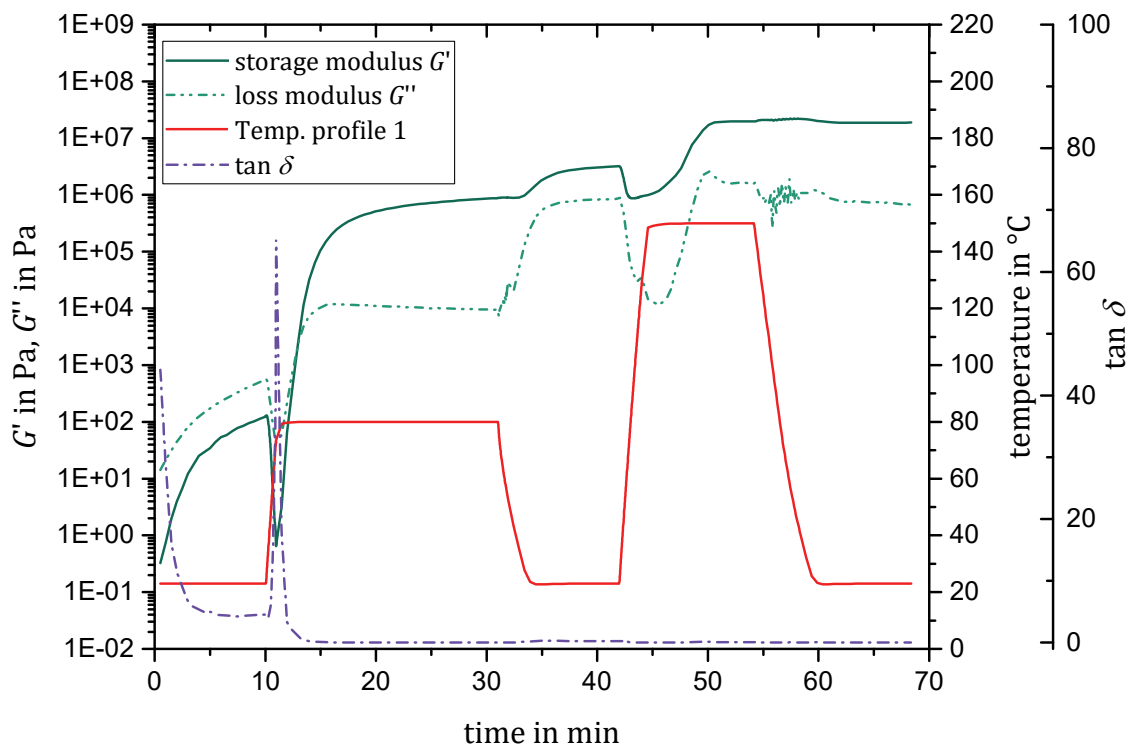
Figure 3.19: Elastic and viscous behavior of formulation V2

To conclude, the viscosity profile of the developed formulation can be plotted against the ideal viscosity profile presented in the introduction of this chapter (see Figure 3.20).
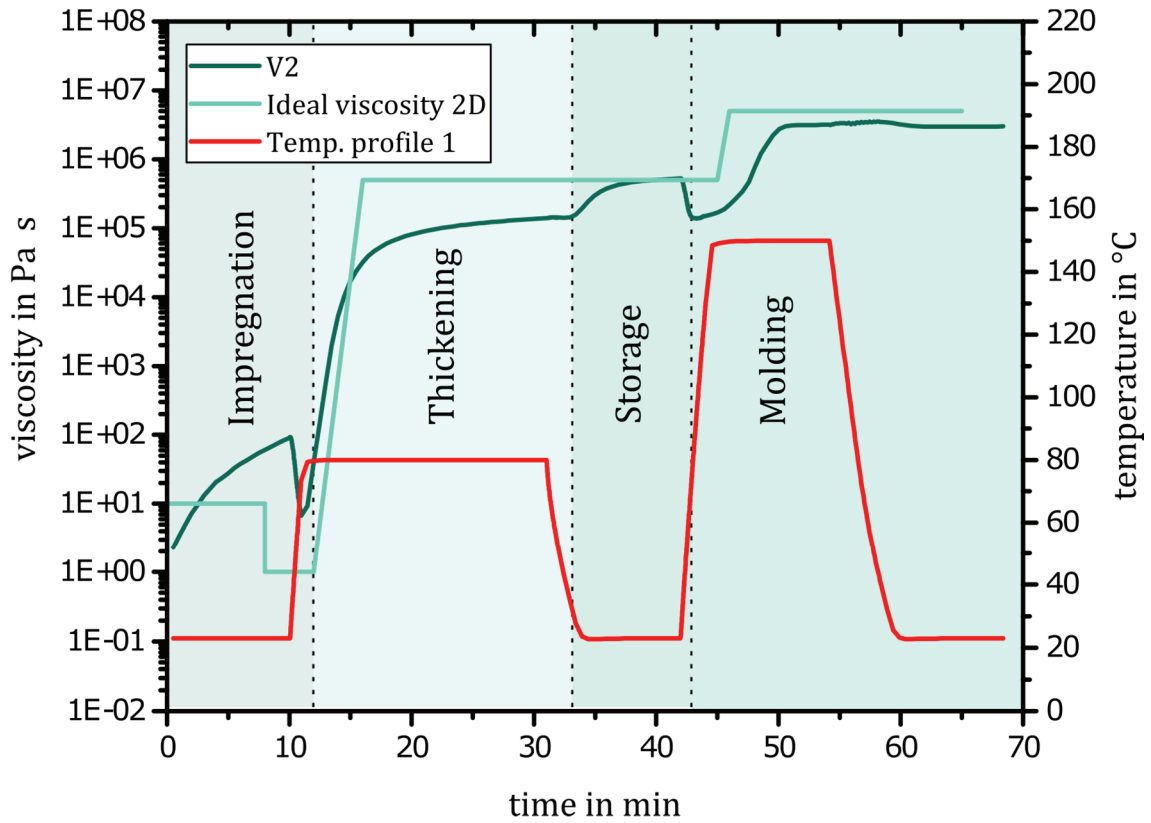
Figure 3.20: **Comparison of the viscosity profile of the ideal matrix and the complex viscosity of formulation V2**

It's found that formulation V2 is suitable for the direct processing of CoFRTS and will be set as reference for further trials. The formulation is shown in Table 3.4 with respect to the range of changes in amount of the single ingredients.

Table 3.4: **Developed CoFRTS formulation, amounts in phr**

Daron 41	100
UOP L	1.5 to 9
pBQ 10%	.3
Peroxan	1 to 1.2
Bayferrox	0 to 139
MDI	25 to 27
BorchiKat	.1 to .15

4 Process Development

To evaluate the co-molding process concept on the one hand and the corresponding materials used on the other hand, samples of different complexity have to be produced. The basic mechanical properties of the DicoFRTS and the CoFRTS are determined with specimens taken from flat plates. The basic mechanisms of co-molding are investigated by locally continuous-fiber reinforced DicoFRTS plates, as well. To validate the found co-molding mechanisms for more complex parts a section of an automotive subfloor is used (compare Figure 4.1). Here, the draping of the CoFRTS is investigated by using the geometry of the cross beam. The cross beam is the sub-preform of the subfloor structure showing the highest complexity, including corners.
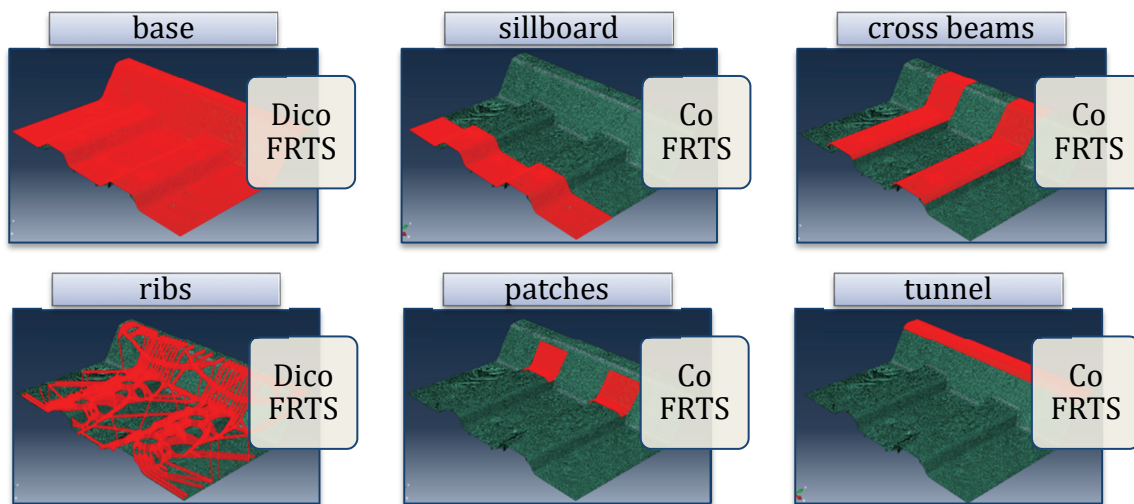
Figure 4.1: **Terminology and material classes of tailored subfloor structure**

4.1 Semi-finished Materials

The processing of semi-finished continuous-fiber reinforced material differs from the processing of the discontinuously reinforced ones. Fibers, matrix and required material amount are dissimilar in general. Therefore, the production is done on separate lines. Compare Table 4.1

for the specifications of the manufacturing lines available at Fraunhofer ICT.

Table 4.1:   Fraunhofer ICTs CoFRTS and DicoFRTS lines

		DicoFRTS line	CoFRTS line
Working width	mm	800	300
Line speed	m/min	1.5-9	.3
Surface weight	kg/m²	1-3	.5
Max. output	kg/min	21	.045

4.1.1 Production of Semi-finished DicoFRTS

The individual components for the matrix of DicoFRTS are mixed by the help of a dissolver type *F11ML4-305* by *VMA-Getzmann*. If required, this can be done under vacuum. In a further step the compound is produced with an industrial flat conveyor plant type *HM-LB-800* by *Schmidt & Heinzmann* (Figure 4.2). Additional to the basic configuration the device supplies a second chopper to manufacture CF-DicoFRTS and five heating zones to improve fiber impregnation.

Figure 4.2:   Modified flat conveyor plant *HM-LB-800*

4.1.2 Production of Semi-finished CoFRTS

The components of the UPPH resin used for the CoFRTS are prepared by a dissolver type *5BCu2-042* by *VMA*-Getzmann. The result is the A- and B-premix as found in the previous section. The premix is then

filled into two-chamber-cartridges (type *AC 400-04-10-01* by *Sulzer*) at the volume proportion 4 : 1 and stored cooled until production. The application of the resin on the line (shown in Figure 4.3) is made by the help of an automated dosing device (*PowerPush 7000MP*). Hereby, the final mixture of component A with component B is generated directly at the doctor box by a static mixing head (*MCH 06-32 T*) flange-mounted to the dosing device. This enables for constant and reproducible application of the resin film on the silicone coated paper at a low degree of cross linking and therefore low viscosity. In a next section of the line the UD-fabric is deposited on the resin film. The compound is then sandwiched by the help of another silicon coated paper and optionally guided through several facing impregnation rollers. Afterwards, the material can first be heated up and then cooled down to either accelerate or slow down cross-linking reactions.
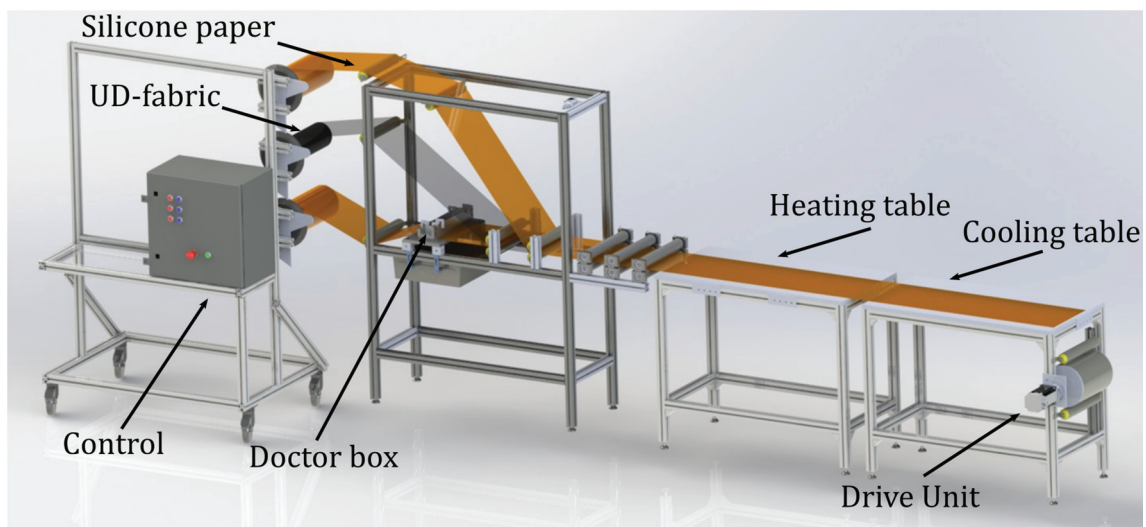
Figure 4.3: **Laboratory impregnation line for CoFRTS, according to [141]**

An exemplary temperature profile of the CoFRTS material manufactured by this procedure is shown in Figure 4.4. Here, the heating rate respectively the cooling rate is the first derivative of the temperature by time. As the line achieves cooling rates of $\approx 100\,°C/min$ at a line speed of 0.3 m/min only a small part of the cooling table is needed to prevent further cross linking. Thus, the cooling table is also used to cut

the material. Finally, the prepreg is stored for the next process steps of optional draping and molding.
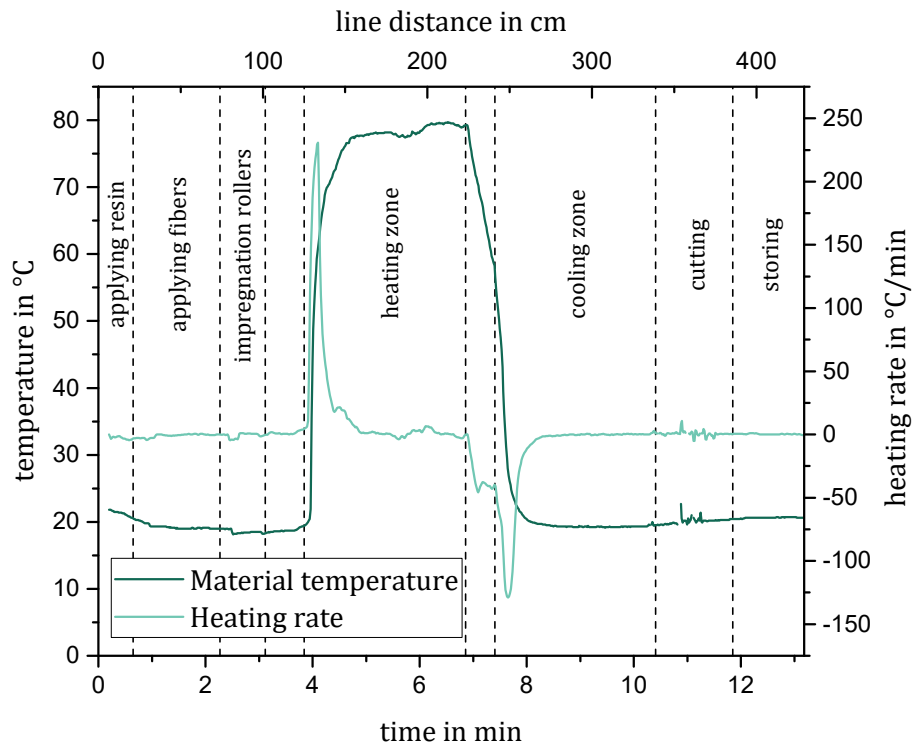
Figure 4.4: **Temperature profile and heating rate during manufacturing CoFRTS**

4.2 Draping

The CoFRTS material, manufactured by impregnation of the UD-fabric, has to be prepared for molding. First of all the material is cut according to the final dimensions of the reinforcement at product level. If a specific layer structure or more than one layer is needed, the cut CoFRTS has to be stacked accordingly. Furthermore the CoFRTS has to be draped prior to molding to realize complex shapes.

The UPPH resin system with its 2-step-curring offers the possibility to manufacture CoFRTS preforms of stable geometry at a shelf-life of several months without the need of cooling. To achieve this, the degree of cure of the first reaction must fit the single process steps. The material must be dry enough for cutting but tacky enough for stacking. Afterwards the resin has still to be viscous to be deformable without any spring back. After draping, the first reaction step has to be completed to give the material sufficient stiffness for further handling operations. Thus, the draping mold should be heatable to increase reaction velocity and decrease cycle time.

Hereafter, three different concepts of draping CoFRTS reinforcements for the subfloor-structure shown in Figure 4.1 are introduced.

4.2.1 Manual Draping

For manual draping of the reinforcement structure a negative mold of aluminum is used (see Figure 4.5, left). A scheme of the process is shown in Figure 4.6: previously cut and stacked rectangular patches are positioned manually on the negative mold (a). A compression molded part is used as upper mold (b). By manually combining the two molds the forming of the CoFRTS is achieved (c). Hereby, the upper mold can be moved freely by the operator to prevent wrinkles. Clamp units apply pressure on the material (d). Furthermore, the negative mold provides heating channels (Figure 4.5, right).
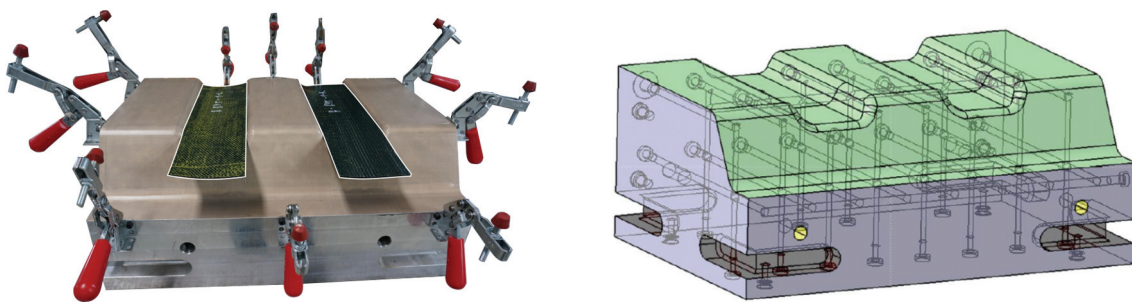
**Figure 4.5:   Negative mold for manual draping
left: Mold with CoFRTS patches and clamping units
right: CAD picture showing the internal heating channels**
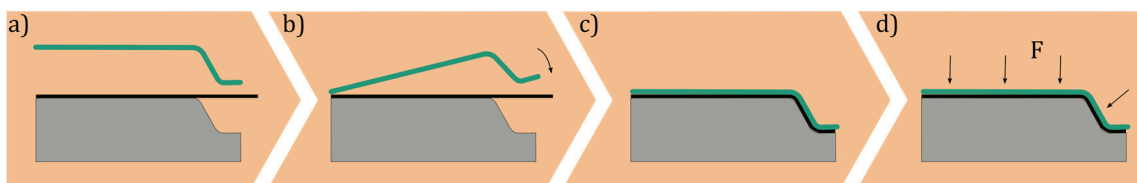
Figure 4.6:   Scheme of the manual draping process

4.2.2 Stamp Draping

For stamp draping the same negative mold is used then for manual draping (Figure 4.7, left). This mold is mounted in the *Preform Center* manufactured by *Dieffenbacher GmbH* and located at *Fraunhofer ICT*. In this case the Preform Center is equipped with 6 stamps (Figure 4.7, right). The process is shown schematically in Figure 4.8: the material is placed manually on the negative mold (a). The stamps are draping the CoFRTS sequentially and provide controlled pressure (b-d). The negative mold can be heated during this process.
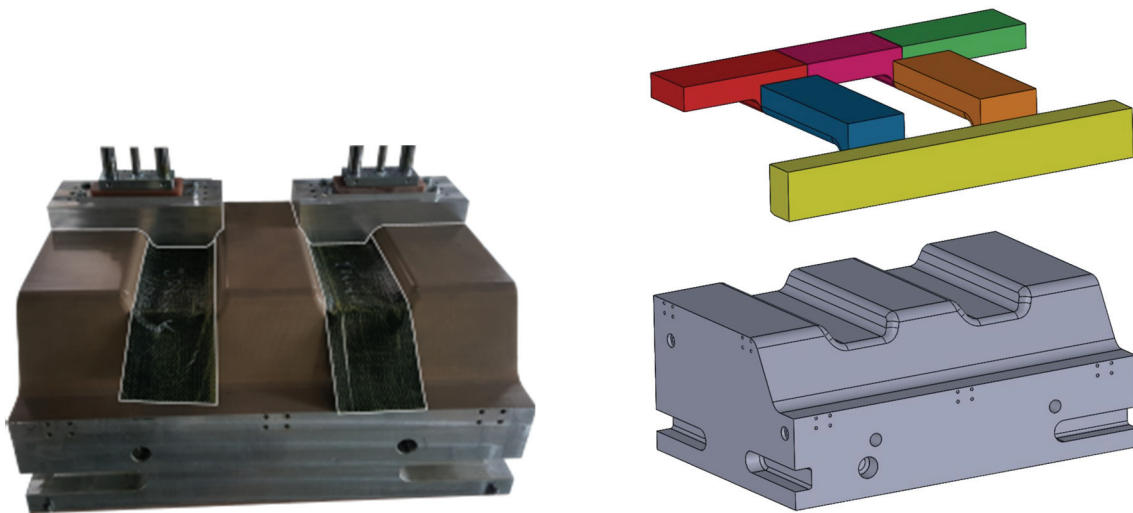
Figure 4.7: **Mold for stamp draping**
left: Negative mold with CoFRTS patches and two stamps
right: CAD picture visualizing the layout of the stamps
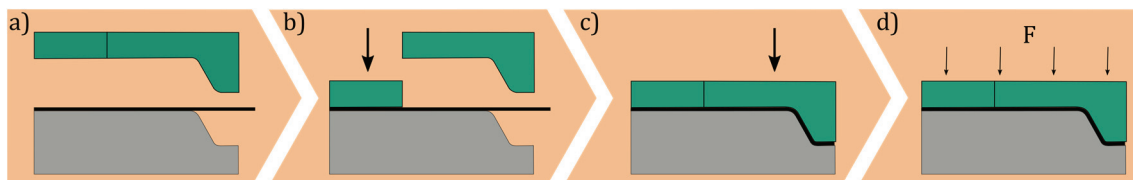
Figure 4.8: **Scheme of the stamp draping process**

4.2.3 Magnetic Draping

CoFRTS material containing magnetite can be draped using magnetic fields. For this purpose a device was developed within the framework of a master thesis (Bauer, S.: Draping by means of magnetic forces to manufacture sub-preforms for structural SMC-components). The device shown in Figure 4.9 is equipped with moveable Neodymium magnets to provide the magnetic field. Neodymium magnets are rare-earth magnets made of a neodymium, iron and boron alloy and therefore also called NdFeB-magnets. They are the strongest commercially available permanent magnets [1]. Thus, they are ideal to apply high forces at limited installation space. The magnetic draping device is not able to drape the whole reinforcement structure. It is limited to the most complex part - the double curved cross beam. Two parts of this sub-preform can be manufactured simultaneously. Figure 4.10 shows the schematic draping process: first the material is placed manually on the device (a). In a next step PMs are moved according to a programmed sequence to achieve the first curvature along the cross beam (b). The second curvature is generated by lifting a part of the mold (c, d). The mold surface is heatable by electrical heating cartridges. An upper mold is not required for this draping concept.
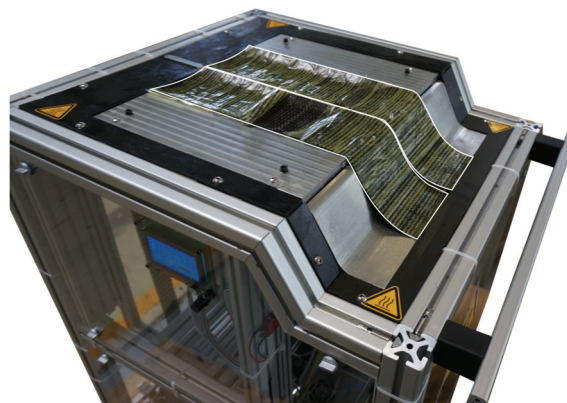
Figure 4.9:   Device for magnetic draping
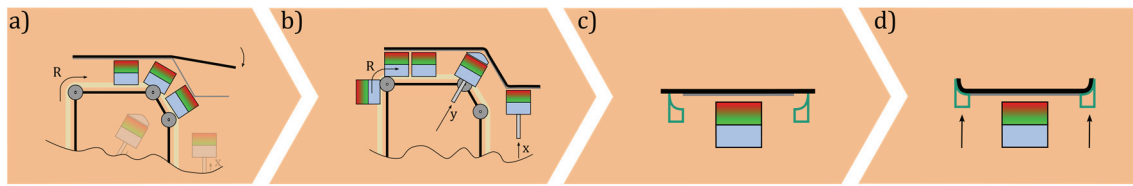
Figure 4.10: Scheme of the magnetic draping process
         a), b): Side view
         c), d): Frontal view

4.3 Molding

Hydraulic *Dieffenbacher* presses are used for compression-molding of plates or parts. The *COMPRESS PLUS DCP-G 3600/3200 AS* offers a maximum molding force of 36 000 kN, the *DYL 630/500* offers 6 300 kN. Both presses are able to control the parallelity of stamp in relation to the cavity.

4.3.1 Molding of Plates

The mold shown in Figure 4.11 is used to manufacture plates for basic research and material characterization. The steel mold is designed to operate with several technologies and part geometries. In the SMC-plate setup it comes with a flash face of 70 mm height, seven pressure sensors (*6167A* by *Kistler*) in the cavity and the possibility to change the geometry by inlays. Both, lower mold and upper mold frame, are heatable by oil circuits. The molded plates are 800 mm in length and 250 mm in width. The plate thickness is the result of weight and density of inserted material and therefore variable.

thermal insulation
upper mold frame
stamp
shot-pot plug
changeable flash face
inlay
guiding
lower mold
thermal insulation
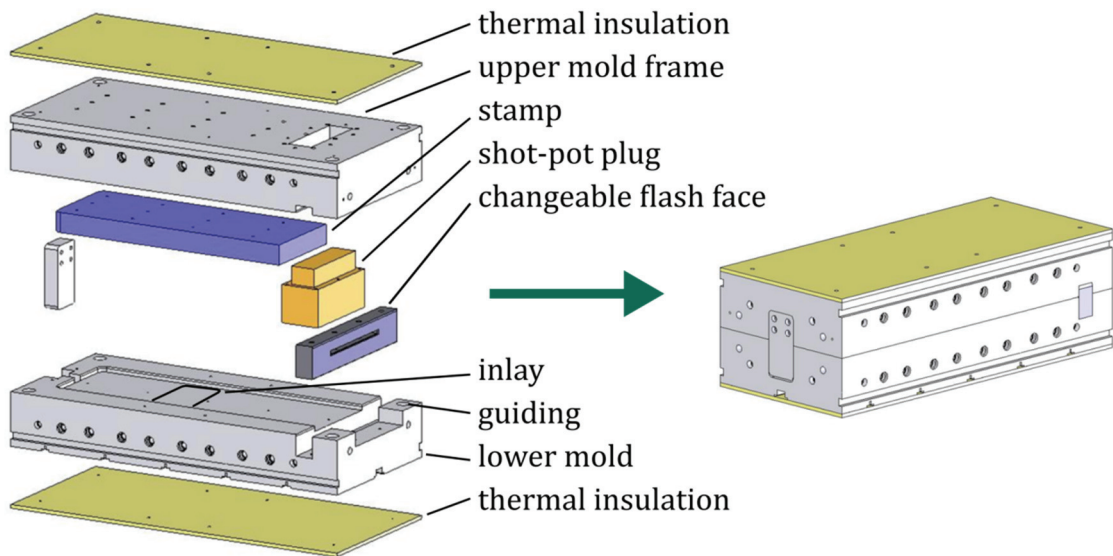
Figure 4.11: Terminology and technical structure of the plate mold

4.3.2 Magnetic Fixation Concept

The cavity of the plate mold provides an installation space of $230 *$ $230 * 20 \text{ mm}^3$ to mount custom inlays (Figure 4.11). This space is used to equip the mold with permanent magnets (PMs) to enable a fixation of CoFRTS by magnetic fields during co-molding with DicoFRTS. The local reinforcements have a size of 220 mm in length and 25 mm in width. The PMs ought to be mounted at the backside. So they are not visible in the mold cavity and do not have contact with the material and there will be no marks visible on the final product.

NdFeB 40UH rare-earth magnets are chosen to supply the magnetic field. Hereby, the value 40 indicates the energy product (magnetic flux output per unit volume) and the letter combination UH specifies the maximum operating temperature to 180 °C. The dimensions of these PMs can be realized according drawing.

To maximize the fixation force acting on the CoFRTS reinforcement the finite element simulation software FEMM for magnetic fields is used. Parameters of the optimizations are:

- Amount of PMs
- Size of PMs
- Orientation of PMs magnetization

The optimization is performed in the following steps (compare Figure 4.12): a simplified model is designed by the help of computer-aided design (CAD) software (*SolidWorks* by *Dassault Systems*). The model includes actual magnet setup, inlay, reinforcement and steel mold. The reinforcement is designed with a thickness of 0.31 mm. This coresponds to the thickness of one layer CoFRTS having 60 wt. $-\%$ of carbon fibers. A characteristic two dimensional cross-section of the model is then exported to the drawing interchange file format (DXF). This DXF is then imported and parameterized within FEMM. FEMM comes with a material library, which has the chosen PM NdFeB 40 already listed. This library is extended at the basis of the $B(H)$ measurements shown in Figure 3.8 for various FRP with different magnetite content using equation (3-3). In a next step the model is meshed and computed. The result is analyzed by calculating the total attraction force of magnet(s) to FRP and by review of the visual output of magnetic field density on homogeneity. The optimization target is a combination of maximum fixation force and a magnetic field of high homogeneity in the reinforcement. This procedure is repeated, until the improvements become negligible small.

The optimization leads to a PM setup of 15 cuboidal magnets with alternating magnetization. One single magnet has a pole area of 25 mm by 12 mm and a height of 15.4 mm. The distance between two magnets is 15 mm.

For this setup and an FRP-magnetite content of $\varphi = 5.16$ vol. $-\%$, computations at different stamp distance were performed. The simulation results show a change in attraction force during closing the mold

(see Figure 4.13). Maximum fixation force of 2.1 N is achieved at a stamp distance of 2.81 mm (Figure 4.13, c). This corresponds to a magnetic flux density within the reinforcement of ≈ 0.6 T. Without stamp the attraction force is only 1.3 N (Figure 4.13, d). A completely closed mold results in a minimum of fixation force (Figure 4.13, b).The corresponding false-color images visualize, how the approaching stamp changes the magnetic field strength inside the reinforcement. As the change in attraction force is significant, the stamp distance has to be taken into account for calculating the actual attraction force on the CoFRTS.
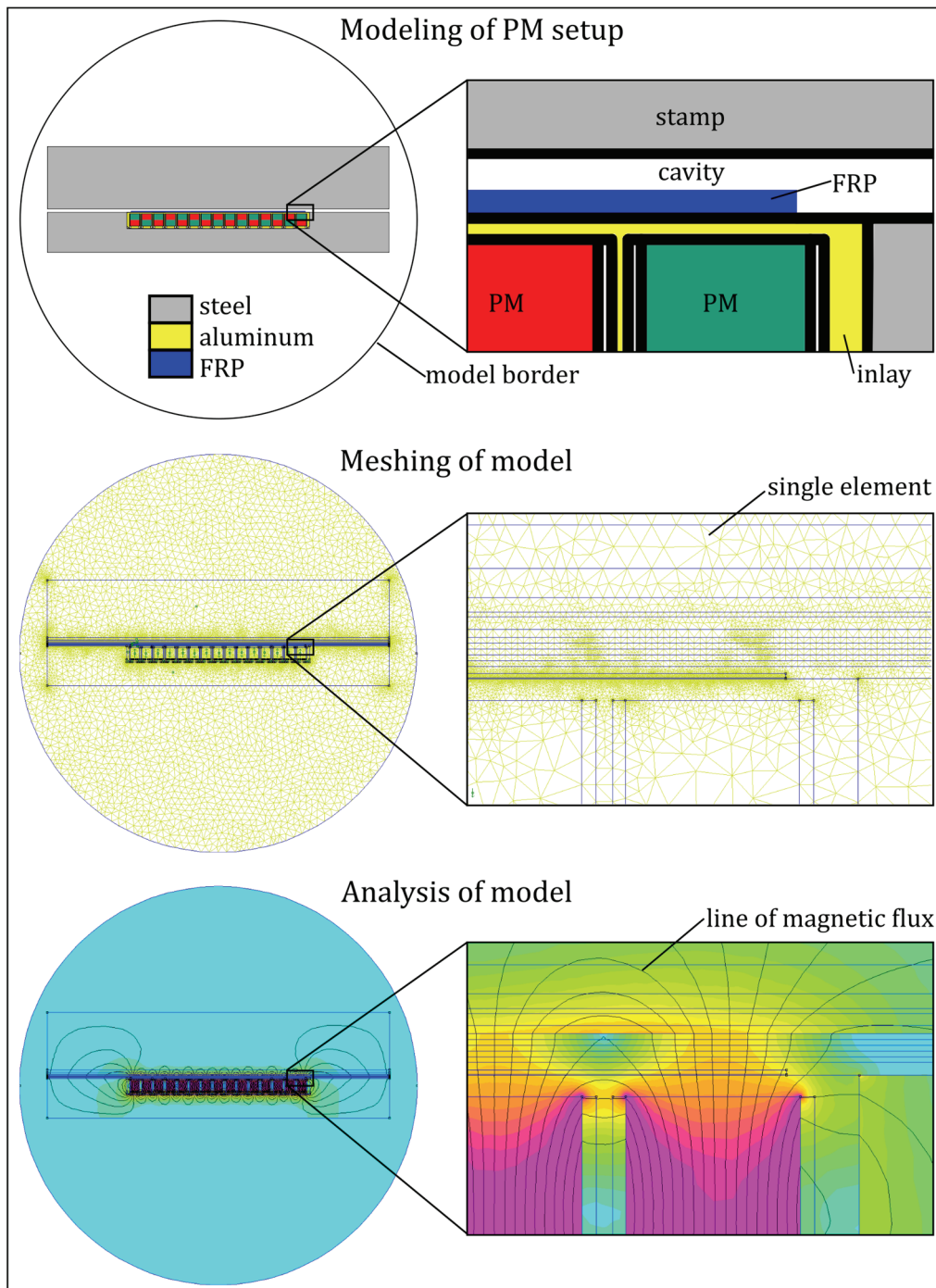
Figure 4.12: Attraction force optimization sequence
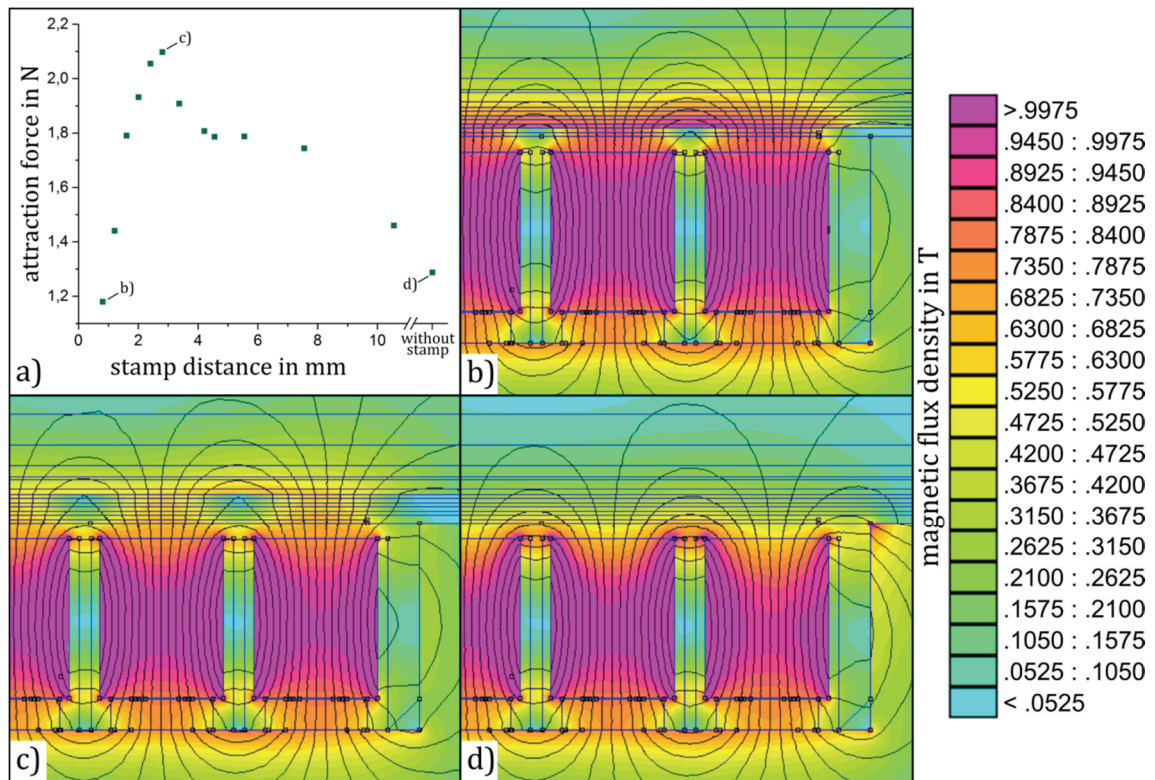
Figure 4.13: FEMM simulation results
a) Attraction force for different stamp distances
b) Magnetic flux density B at a distance of 0.81 mm
c) Magnetic flux density B at a distance of 2.81 mm
d) Magnetic flux density B in the open mold

In addition to a maximized fixation of the reinforcement, the inlay has to withstand the forces applied to it during molding without plastic deformation. Two conflicting goals arise in this context:

- The inlay has to be made of a paramagnetic material to be transparent to the magnetic field. Tool steel, the usual mold material, shows high values in yield strength, but is ferromagnetic.
- The PMs have to be very close to the cavity to maximize the attraction force. Thus, the mold material separating cavity from magnet has to be as thin as possible.

  To deal with this issue, finite element simulations (*SolidWorks* by *Dassault Systems*) are performed regarding the structural integrity of the inlay alongside the simulations optimizing the magnetic behavior.

As inlay material the high-strength aluminum alloy AlZnMgCu1.5 is chosen because of its high yield strength ($Rp_{0.2} \geq 360\,\text{N/mm}^2$ [142]) and paramagnetic behavior. The internal mold pressure is specified to 200 bar. The target is to reduce the wall thickness until a maximum von-Mises-stress of 240 N/mm² is reached. This corresponds to a safety factor of 1.5 against plastic deformation. Design studies with more than 200 simulations led to the design shown in Figure 4.14. By introducing a radius into the edges of the pocket meant for the PM (Figure 4.14, b) the inlay shows homogenous values for the von-Mises-stress (Figure 4.14, c). Thus, the wall thickness of the aluminum separating the PMs from the cavity could be reduced to 1.5 mm.
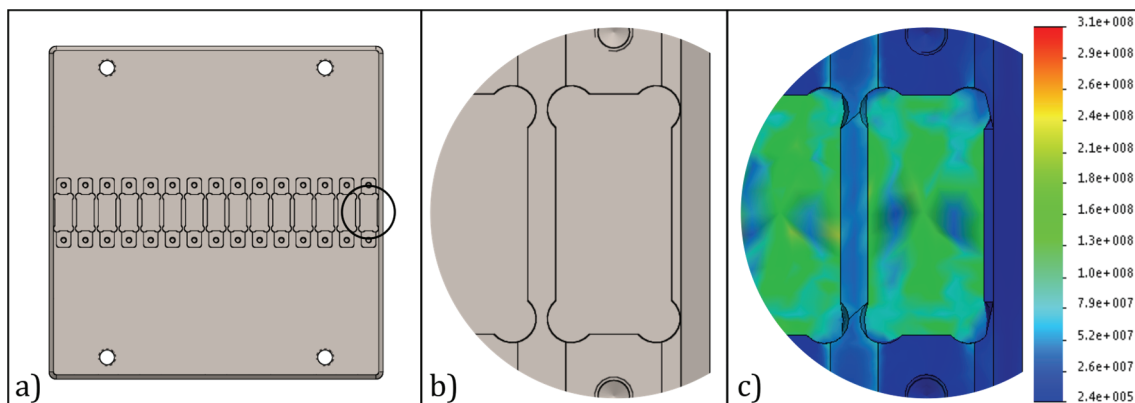
Figure 4.14: **Final design of the PM inlay**
a) Total bottom view
b) Detail bottom view
c) False color image of von-Mises-stress in N/m²

4.3.3 Molding of Parts with Complex Structure

Parts of complex geometry are molded with the subfloor mold (Figure 4.15). This mold is supplied by the public funded project *MAI qfast* [18] and designed and manufactured by *Siebenwurst Werkzeugbau GmbH*. The steel mold is heatable up to 180 °C by six water circuits and can be used for thermoplastic and thermoset processing. The stamp provides two inlays containing the rib geometry (Figure 4.15, stamp, green) and

ejector pins (Figure 4.15, stamp, blue). The mold is manufactured with flush faces (10 mm at 1 °, 30 mm at 10 °) allowing for net shape production and variable part thickness (min. 1 mm). The projected size of the part is 600 mm in length, 400 mm in width and 110 mm in height.
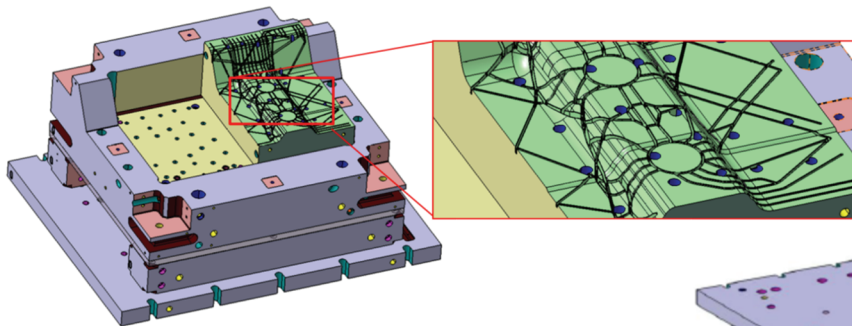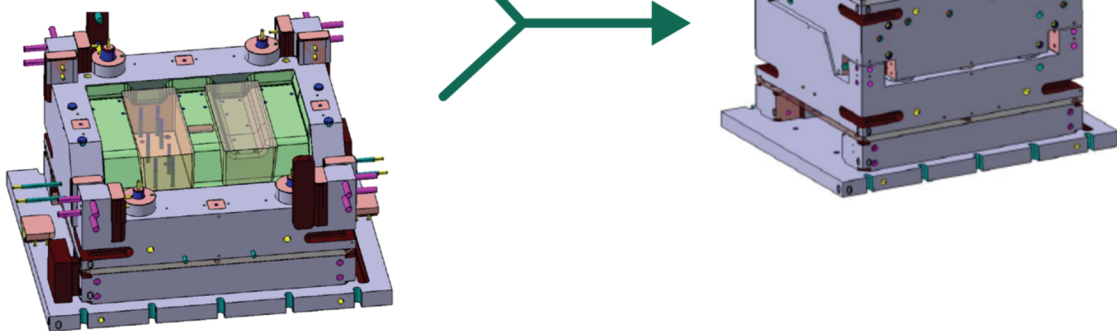
Figure 4.15: Technical structure of the subfloor mold

A fixation of the reinforcement structure inside the mold shall be achieved by a geometrical form fit of reinforcement to mold. There is no separate fixation concept included like it is the case for the molding of plates.

5 Characterization & Modelling

The previous sections fixed the materials, formulations, manufacturing conditions and processing conditions for the creation of parts made of CoDicoFRTS. Content of the present section shall be to characterize the CoFRTS more deeply with the objective to be able to describe the effects and mechanisms during co-molding. This is crucial for a sufficient understanding of the complex process of co-molding. The investigations are performed at the level of plates and but also at the level of complex components. Figure 5.1 gives an overview how the single characterization methods interact to finally validate the concept of co-molding.
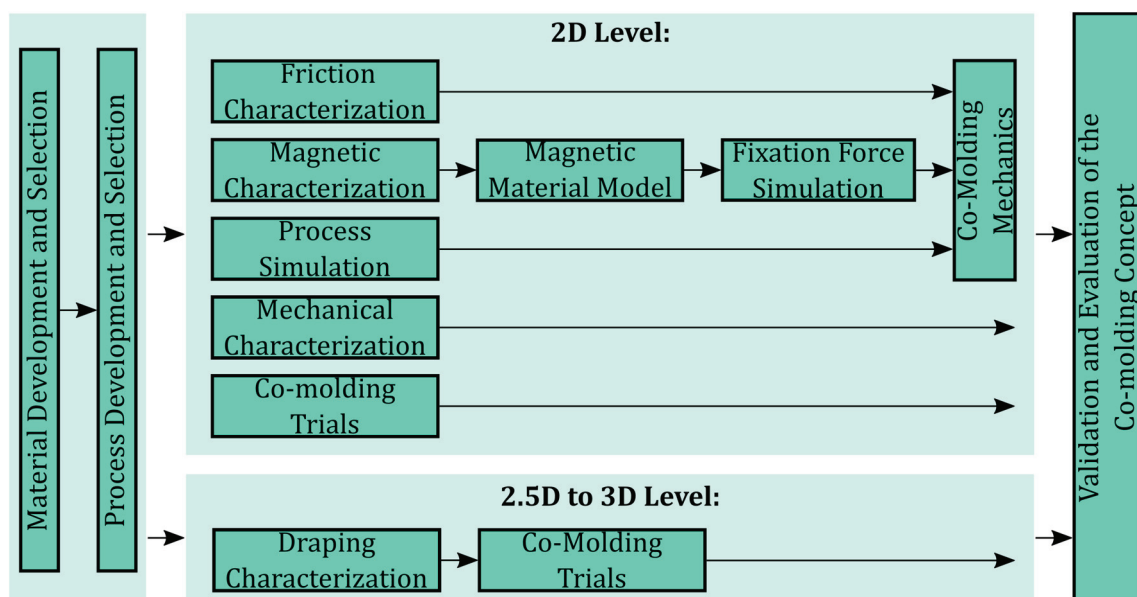
Figure 5.1:   Approach of this thesis

5.1 Characterization of Friction

Besides gravity, there are two forces fixating the CoFRTS during co-molding. One is the hydrostatic pressure applied by the press, but transferred by the DicoFRTS material. The other is the attraction force applied by the optional magnets. None of both acts directly against the direction of the displacement force applied by the flowing SMC. Fric-

tion is needed to transfer the force. Thus, the friction between the CoFRTS and mold has to be investigated in detail.

There are several parameters, that could possibly affect the friction coefficients for static friction μ_{St} and dynamic friction μ_{Dy} of CoFRTS materials at the surface of a mold:

- Temperature
- Displacement parallel or perpendicular to fiber direction
- Content of fillers, like magnetite

5.1.1 Methodology

The international standard in measuring the friction of polymers (ISO 8295 [143]) is performed only at room temperature, in contrast to the American standard (ASTM D1894-14 [144]). The measuring procedures of these standards, as well as the apparatus of type *2810-005* by *Instron,* were basis for the modifications described in the following to closely fit conditions during draping and co-molding.

One part of the friction pair is a heatable plate of aluminum. As other part CoFRTS material is fixed underneath a sled (200 g in weight) by the help of double-faced adhesive tape (compare Figure 5.2). Therefore, several different CoFRTS materials were produced. As reference a UP based CoFRTS (formulation: material 1 in Table 8.6 on page 143) and a UPPH based CoFRTS (Table 8.3 on page 140) are used. Additionally, UPPH-CoFRTS material of different magnetite content φ were produced (0, 2, 3.7, 6.5 and 8.7 vol. $-\%$). All UPPH based materials were then stored for several months at 18 °C to surely achieve a stable B-stage without starting the radical polymerization. The UP based material was thickened for three days at 29 °C and stored for eleven days at 18 °C before the measurement. The sample size is 63 mm in fiber direction and 50 mm perpendicular to it. The fiber direction is according to the testing direction. The resin rich surface of the sample was placed towards the other friction partner.

The sled is connected by a cable via a pulley with a load cell of 10 N. According to ISO 8295 [143], the cable should accomondate a spring, when measuring the static friction coefficient. This compensates the inertia of mass of the sled. When measuring the dynamic friction coefficient, the connection between sled and load cell should be rigid to reduce slipstick behavior. Designing the process using μ_{St} could lead to a labile equilibrium. The static friction could be overcome by force peaks during co-molding. Furthermore an once initiated movement of the reinforcement would not be stoppable. As the outcome of the investigations described here should serve as input to design fixation mechanisms, a conservative and fail safe approach is preferred. Thus, the focus is set to determine the dynamic friction coefficient μ_{Dy}. Therefore, a rigid steel cable is used. The behavior of the material, when the force is built up, is displayed in the graphs, nevertheless. Hereby, it must be considered, that potentially occurring peaks in the frictional force will be intensified by the inertia of mass of the sled. Calculation of the static friction coefficient will be omitted obviously.

To perform a measurement, the sled is equipped with CoFRTS and placed on the aluminum table. The sled is then pulled 5 to 15 mm to overcome influences generated by misaligned placement. After a total contact time of 10 s between CoFRTS and aluminum, the measurement is started.

The motion inducing the friction process is set to 100 mm/min and realized by a universal testing machine. The measurement is stopped after a movement of 70 mm. Each experiment is repeated at least five times.
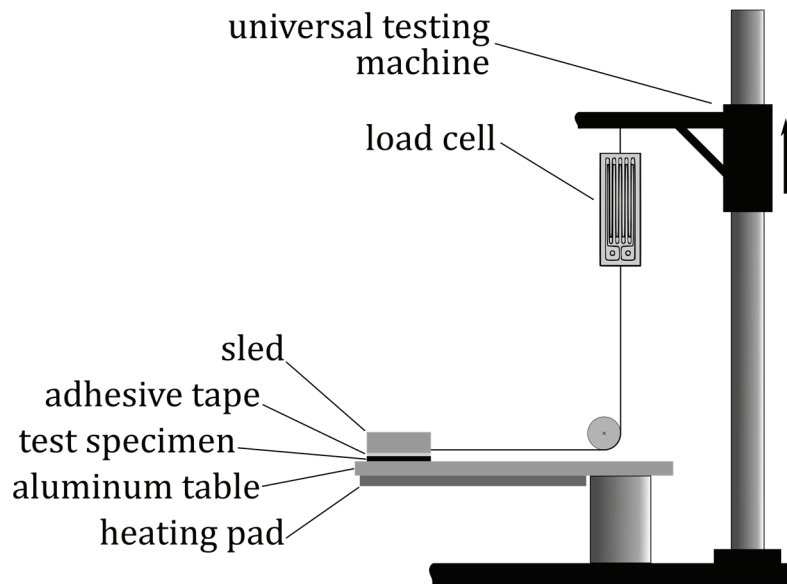
Figure 5.2: **Test stand to characterize friction between CoFRTS and mold**

The dynamic coefficient of friction μ_{Dy} is calculated according to [143] using the equation:

$$\mu_{\mathrm{Dy}} = \frac{F_{\mathrm{Dy}}}{F_{\mathrm{p}}} \tag{5-1}$$

$$\left[F_{Dy}, F_{p}\right] = \mathrm{N}$$

where the dynamic frictional force F_{Dy} is the average force between 10 and 70 mm [143]. The normal force F_{p} is calculated from the mass of sled, adhesive tape and prepreg using earth gravitational acceleration to 2.015 N. Deviations in the weight of the prepreg are small compared to the mass of the slide ($\approx$ 0.1 %) and are therefore neglected.

5.1.2 Results and Discussion

Frictional force to distance diagrams of the reference materials are shown in Figure 5.3 for three different temperatures and two resin systems. The dark line represents the average of the measurements. The bright area around it displays the standard deviation.

Obvious is the strong temperature dependency of the materials in general. UP-CoFRTS shows slipstick behavior only at room temperature or at long measurement distances (Figure 5.3 (top, left) and Figure 5.5). For UPPH-CoFRTS this behavior is only visible at an aluminum table temperature of 80 °C (Figure 5.3. (middle, right)).

When viewing the enlarged beginning of the curves (Figure 5.3), the expected peak in frictional force, determining the static coefficient of friction μ_{St}, is very pronounced for UP based materials. For UPPH-CoFRTS there is no peak, except for measurements at room temperature.

Due to the positioning procedure before measuring, the cable is pre-loaded while the sled stands still until a total contact time of 10 s expires and the measurement is started. As a result, the frictional force of UP-CoFRTS starts at a specific value, which describes the preloaded system (Figure 5.3, left). Whereas for UPPH based material viscoelastic behavior can be observed, which is dependent of the temperature. At room temperature it behaves elastic (Figure 5.3 (top, right)), at 150 °C it behavious viscous (Figure 5.3 (bottom, right)). For 80 °C the behavior is viscoelastic (Figure 5.3 (middle, right)).
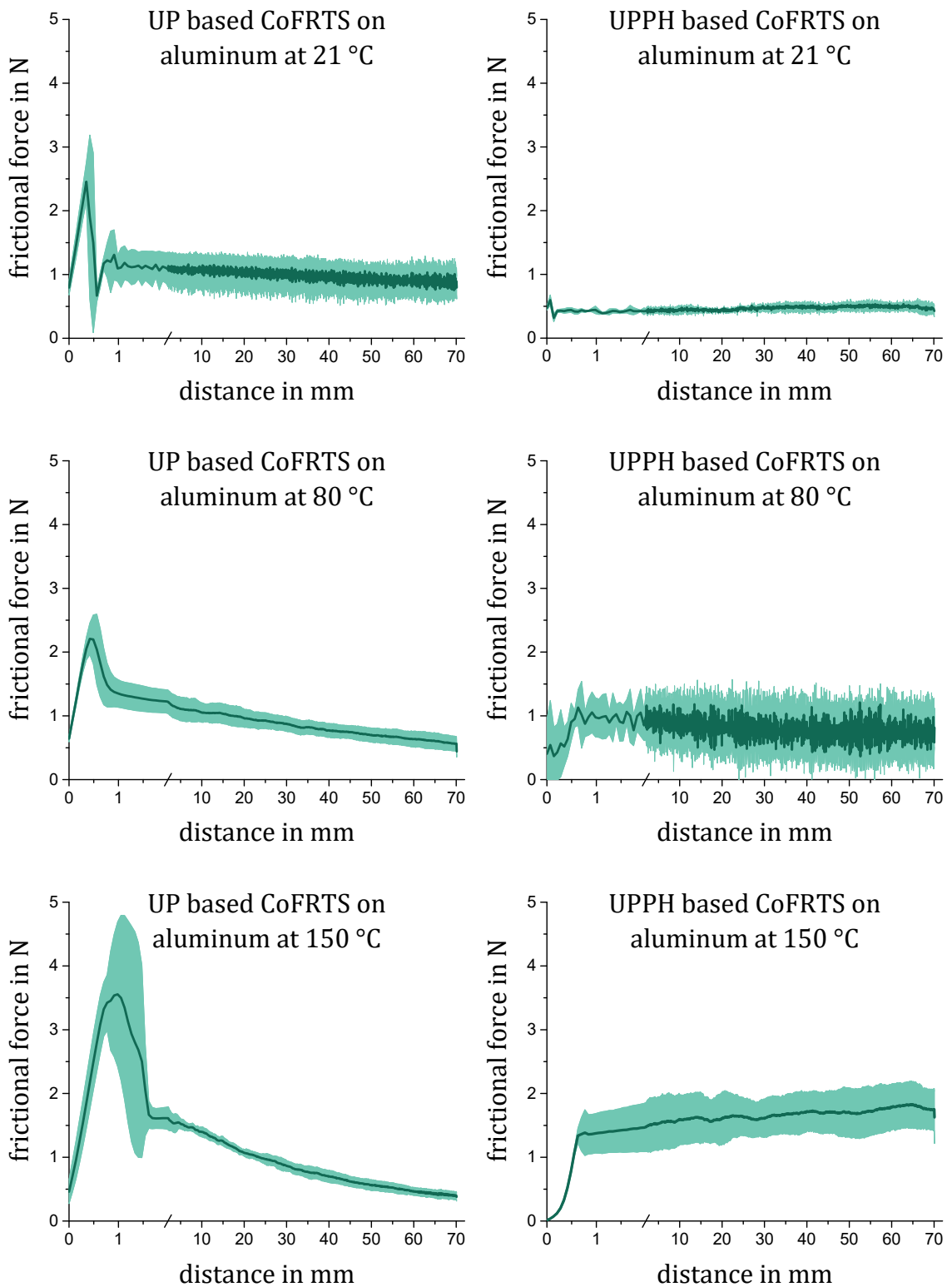
Figure 5.3: **Frictional force of the reference materials on aluminum at different temperatures**

The dynamic coefficient of friction is calculated using Formula (5-1) for UPPH-materials according to [143], see Figure 5.4, left. For UPPH-CoFRTS of different magnetite content φ the results are shown in Figure 5.4, right. To design fixation concepts inside a mold, $\mu_{\text{Dy UPPH}}$ can be expressed as a function of φ:

$$\mu_{\text{Dy UPPH}}(\varphi, T = 150\,°\text{C}) = \mu_{\text{Dy UPPH 0}} + A\mathrm{e}^{R_0 \varphi} \tag{5-2}$$

with:

$$\mu_{\text{Dy UPPH 0}} = 0.52644$$
$$A = 0.31236$$
$$R_0 = -88.088$$
$$\bar{R}^2 = 0.87012$$
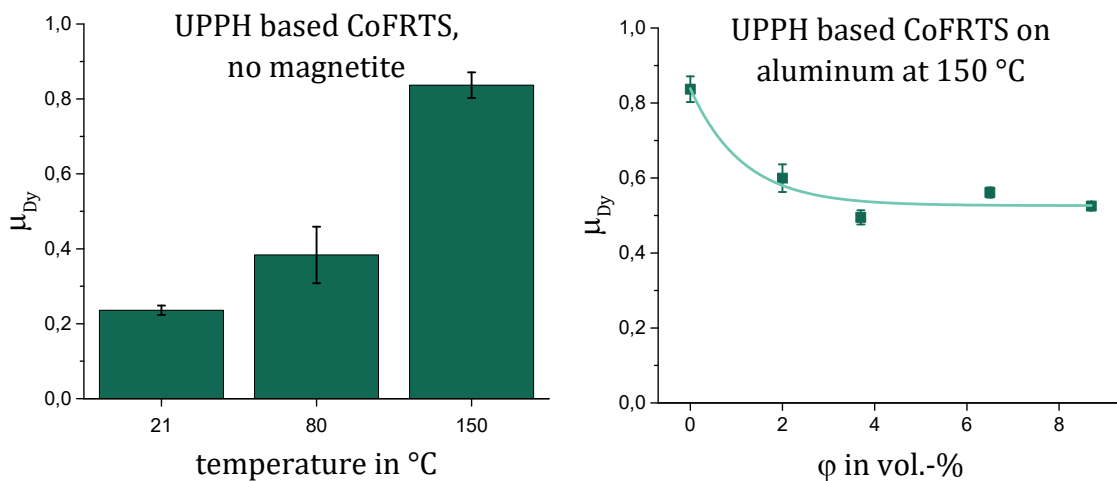
Figure 5.4: **Dynamic friction coefficient of UPPH based CoFRTS**
left: Influence of temperature
right: Influence of magnetite content

The frictional force of UP-CoFRTS is not constant within the evaluation range (10 to 70 mm) for elevated temperatures (compare Figure 5.3). This is probably caused by the major drop in viscosity, which is characteristic for MgO thickened resin systems. The lubricant layer serves as sliding film and reduces the friction. To investigate this effect the total measuring length was increased from 70 to 120 mm (see Figure 5.5). At ≈ 80 mm the frictional force converges. Thus, the evaluation range

is changed (80 to 120 mm) for UP resins system at elevated temperatures. The so calculated dynamic friction coefficient for UP based CoFRTS is $\mu_{\text{Dy UP}} = 0.139$ at a deviation of 0.0189.
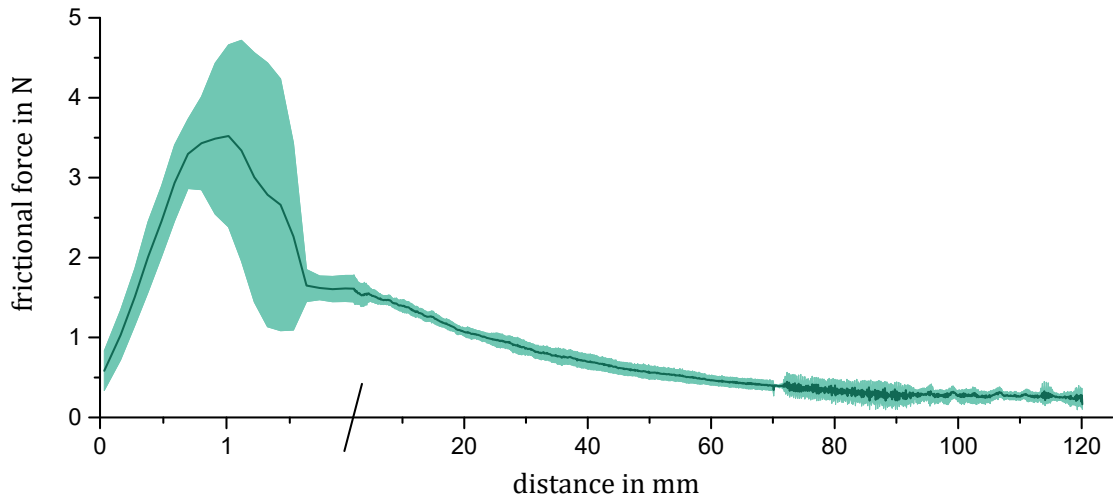
Figure 5.5:   **Frictional force of UP based CoFRTS on aluminum at 150 °C**

To investigate the influence of fiber orientation additional measurements were performed. Therefore, the test specimens were fixed with fiber direction perpendicular to measuring direction. According to Figure 5.6 there is no influence of fiber orientation for UP based materials. For UPPH-CoFRTS the influence is small.
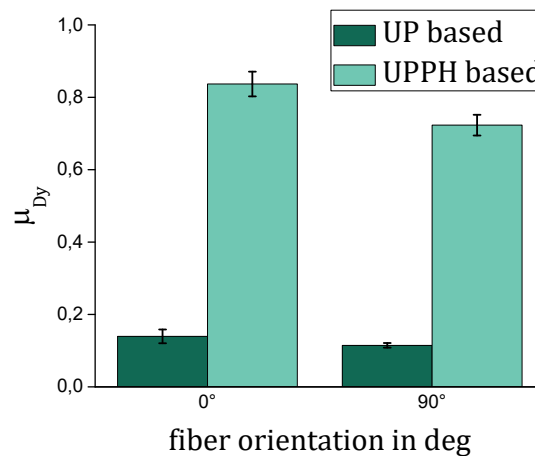
Figure 5.6:   **Dynamic friction coefficient of CoFRTS on aluminum at 150 °C influence of resin system and fiber orientation**

In summary, the resin systems frictional properties show strong dependency of temperature. The influence of fiber orientation is small or even negligible. To design fixation concepts, μ_{Dy} was determined. For UPPH-based materials μ_{Dy} is described as a function of the magnetite content φ.

5.2 Mechanical Characterization

The performance of the developed UPPH CoFRTS (Table 8.3 on page 140) is evaluated in regard to two commercially available VE based CoFRTS materials. The mechanical characterization is performed with compression molded plates of 100 % mold coverage and solely continuous layer structure. The molding parameters were set according to the manufacturers' data sheets (mold temperature 150 °C; molding velocity 1 mm/s; molding pressure $80 - 120$ bar; thickness related molding time $45 - 60$ s/mm). The specimen preparation is done by the help of water jet cutting. Strength, stiffness and ductility of the material were determined in fiber direction (0°) and perpendicular to it (90°) based on the following load cases:

- Tension (DIN EN ISO 527-5 [118])
- Compression (DIN EN ISO 14126 [145, 146])
- Bending, (DIN EN ISO 14125 [147])
- Impact (DIN EN ISO 179-1 [148])

The radar graphs shown in Figure 5.7 and Figure 5.8 summarize the measured material properties. Hereby, manufacturer 1 is set as reference (100 %). The individual standard deviations for each parameter are not displayed for the benefit of clarity. Detailed information about specimen geometry and number of repetitions, about test settings and achieved absolute values, including their deviation, can be found in the annex (Table 8.4 on page 141).
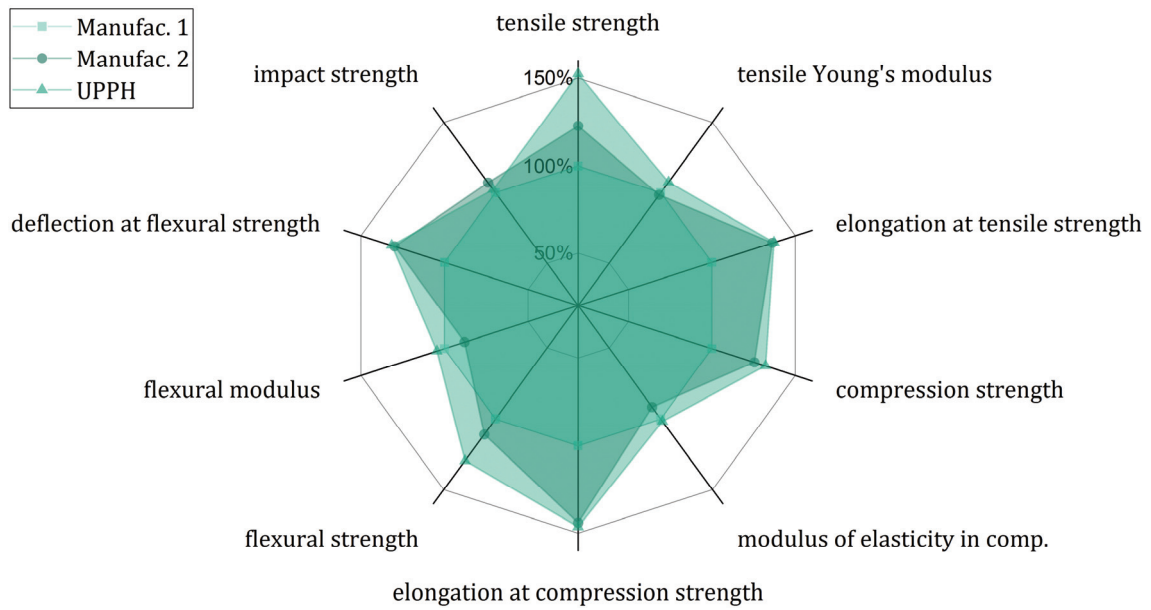
Figure 5.7: **Comparison of UPPH CoFRTS to commercial CoFRTS in fiber direction**

In fiber direction, the UPPH CoFRTS achieves the highest mechanical properties for every load case except of impact strength (see Figure 5.7). This is remarkable, as the UPPH resin is reinforced by a low-priced 50 k carbon fiber in contrast to the more expensive 12 k carbon fiber used for both commercial materials. Especially the value for the tensile strength is outstanding, if one considers that tensile strength and modulus in 0 ° direction are considered to be dominated by the mechanical properties and the content of the fiber, as it is widely reported [149–154]. In pursuit of this logic, the difference in fiber content of the CoFRTS shown in Table 5.1 would be able to explain the superior properties of the UPPH CoFRTS, but not the difference between manufacturer 1 and manufacturer 2.

Table 5.1: **Fiber weight content of the CoFRTS materials**

Material	Fiber content in wt. −%	Measuring method	Source
Manufac. 1	60	ISO 1172	data sheet
Manufac. 2	55	not specified	data sheet
UPPH	64.2 ± 2.7	according to [155]	18 specimens

More recent literature [156] reports, that the tensile strength of CoFRTS is dependent of the matrix's elongation at break, at least for a specific area of tensile stress. This is caused by the anisotropy of the carbon fiber. The fiber shows several orders of magnitude difference in strength, when measured parallel or perpendicular to fiber direction. The perpendicular strength is only two to three times higher than the strength of the resin. Thus, a crack in the matrix will not stop at the interface and tear the fiber [156]. Therefore, the matrix properties should also be considered. Within this work this is achieved by measurements perpendicular to fiber direction. An overview of the results is shown in Figure 5.8.
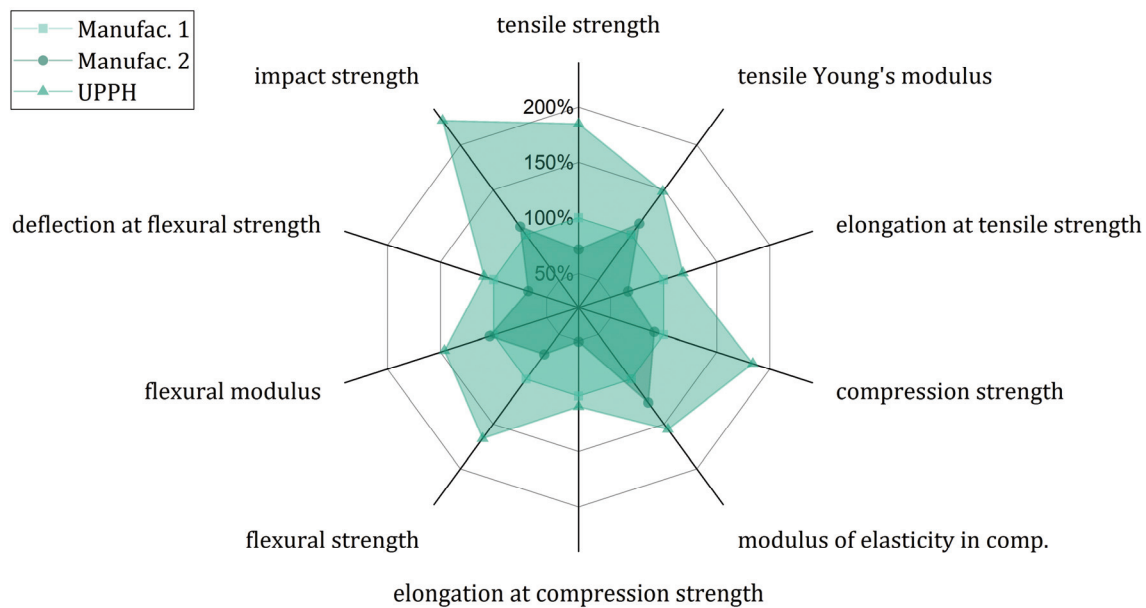
Figure 5.8: **Comparison of UPPH CoFRTS to commercial CoFRTS perpendicular to fiber direction**

In 90° direction, the UPPH CoFRTS shows the highest mechanical properties for each load case. The Charpy impact strength is more than two times higher compared to both commercial systems.

Remarkable is the discrepancy in tensile strength of manufacturer 1 to manufacturer 2. The 23 % higher value of manufacturer 2 in 0 ° direction can neither be explained by fiber content (which is 5 wt. −% lower

than for manufacturer 1) nor by the matrix dominated properties in 90 ° direction (29 % lower tensile strength compared to manufacturer 1). Thus, the reason must be searched for in the carbon fiber and sizing properties of manufacturer 2. Unfortunately, the exact type of fiber is unknown for the commercial systems. So this conspicuousness cannot be examined more thoroughly.

Adding magnetite to the formulation shown in Table 8.3 allows the CoFRTS to behave ferrimagnetic, but this will also affect the mechanical properties of the matrix. To investigate this behavior, UPPH-formulations of different magnetite content were used to produce continuous carbon fiber reinforced plates (mold coverage 100 %; mold temperature 150 °C; molding velocity 1 mm/s; molding pressure 120 bar; molding time 120 s). Specimens (l=230 mm; b=25 mm; h=2 mm) were cut by water jet and tested perpendicular to fiber direction following DIN EN ISO 527-5 [157] (testing velocity=2 mm/min; clamping distance=150 mm; measurement length=100 mm). The results are shown in Figure 5.9.
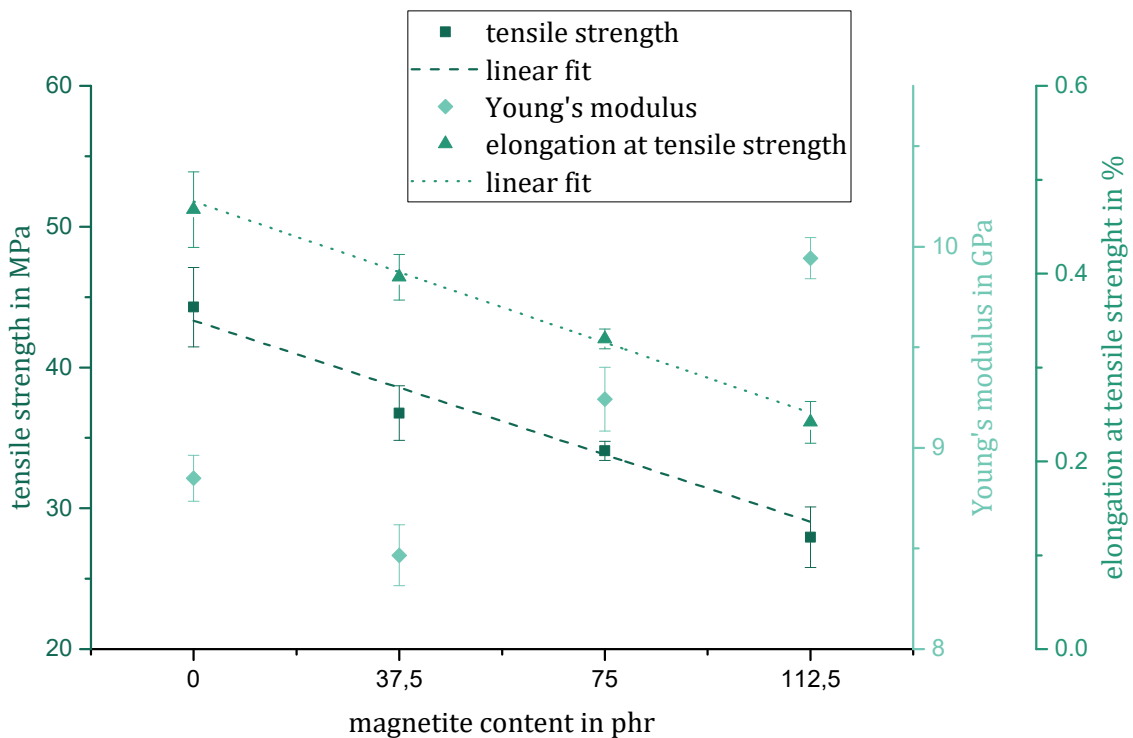
Figure 5.9: **Influence of magnetite content on tensile properties, 90 °**

For a high magnetite content of 125.5 phr, the tensile strength in 90 ° direction drops by 37 %, the Young's modulus rises by 12 % and the elongation at tensile strength drops by 48 %. So there is a clear dependency of magnetite content to mechanical properties. This dependency is negative and near linear for tensile strength ($R^2 = 0.93$) and elongation at tensile strength ($R^2 = 0.99$). For the Young's modulus the dependency is nontrivial but positive, at least for amounts higher than 75 phr of magnetite.

To conclude, the developed UPPH CoFRTS delivers best in class mechanical properties compared to commercial VE-materials, even using a low-priced carbon fiber. Although added magnetite influences the mechanical behavior of the matrix, the impact in absolute values is small for low amounts of magnetite and negative effects can be predicted.

In addition, investigations were performed to compare the UPPH-CoFRTS to Epoxy based prepregs, which are ordinarily considered as a higher class of material having high raw material costs [158]. The outcome of this investigation was published in [17]. It demonstrates that the UPPH CoFRTS reaches the same level in mechanical performance, compared to epoxy based systems using the same carbon fiber. All these results confirm the theoretical considerations made up for formulation and process development.

5.3 Magnetic Characterization

As the general basis to predict the magnetic fixation force, the developed CoFRTS has to be characterized regarding its magnetic properties in relation to magnetite content and temperature. Therefore, measurements with a VSM type *MPMS3* at *LOT-QuantumDesign GmbH* in Darmstadt are performed. Samples of ≈ 2 mm height and 11 mm in diameter are cut by water jet. Afterwards the samples are milled to powder using a centrifugal mill type *ZM 100* produced by *Retsch*. Then, a fraction of ≈ 1 g is filled into a specimen holder. Magnetite content φ

in vol. −% and fiber content in wt. −% are calculated at the basis of rectangular samples of 160 mm ∗ 85 mm out of the same plate, data sheet values and processing parameters. An overview about the specimen regarded in this section can be found in the Annex (Table 8.5 on page 142).

Beside the new magnetization curve of the FRP, the influence of magnetite content φ, process temperature, and remaining magnetization caused by previous process steps are of interest. Thus, measurements of the magnetic hysteresis are performed at a magnetic field strength H of $\approx \pm 1200$ kA/m at three selected temperatures, which occur in handling, draping or molding operations:

- **21 °C** for handling operations performed at room temperature
- **78 °C** for draping operations as the draping mold-half is heated to 80 °C
- **127 °C** for molding operations as this temperature is the limit of the measuring device. The compression mold is heated up to 150 °C

Between the measurements of different temperature the specimen is neutralized according to [81] by applying an oscillating and decreasing magnetic field.

The results of the coercivity measurement can be found in Table 5.2 and Figure 5.10.

Table 5.2: **Values of the coercivity H_C for different temperatures and magnetite content**

$\boldsymbol{\varphi}$ in vol. −%	$\|H_C\|(T = 21 \text{ °C})$ in kA/m	$\|H_C\|(T = 78 \text{ °C})$ in kA/m	$\|H_C\|(T = 127 \text{ °C})$ in kA/m
8.7	1.1	.87	.68
5.6	.67	.57	.44
3.1	.41	.31	.23
0	.0063	.0054	.0047
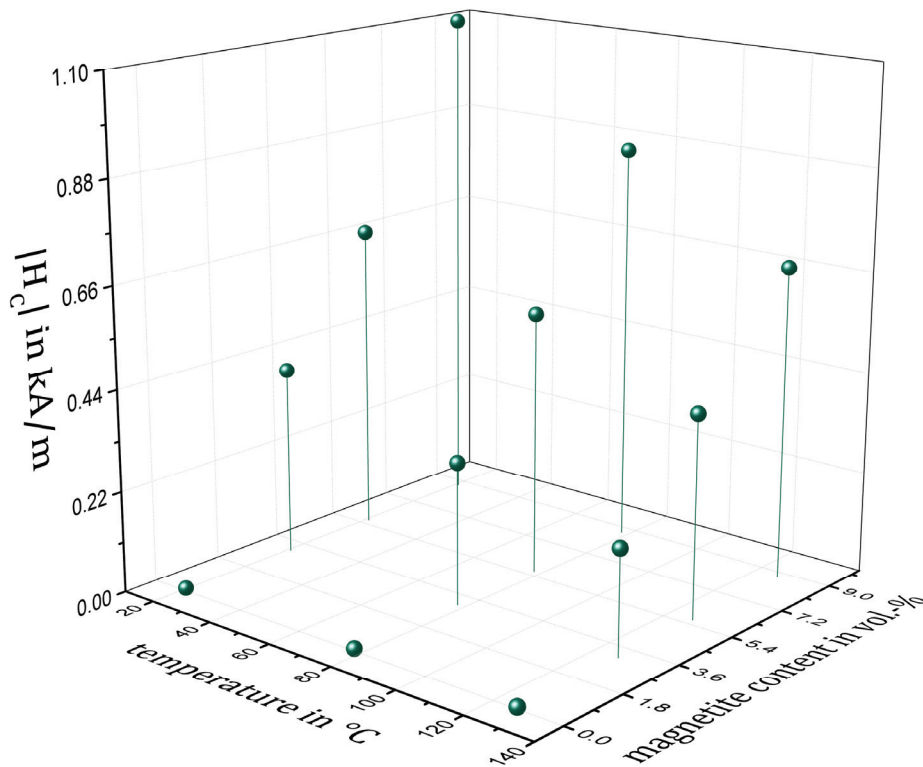
Figure 5.10: Coercivity as a function of temperature and magnetite content

For a FRP without magnetite the coercivity is near zero. $|H_C|$ increases with rising magnetite content and $|H_C|$ decreases with increased temperature. However, the measured coercivity is low compared to the applied field for all temperatures. Accordingly, the remaining magnetization of the CoFRTS caused by draping or fixation will be low and is therefore neglected. Thus, only the initial magnetization curves will be considered in the following.

The initial polarization curve of CoFRTS containing 56 wt. $-\%$ of carbon fibers without magnetite is shown in Figure 5.11.
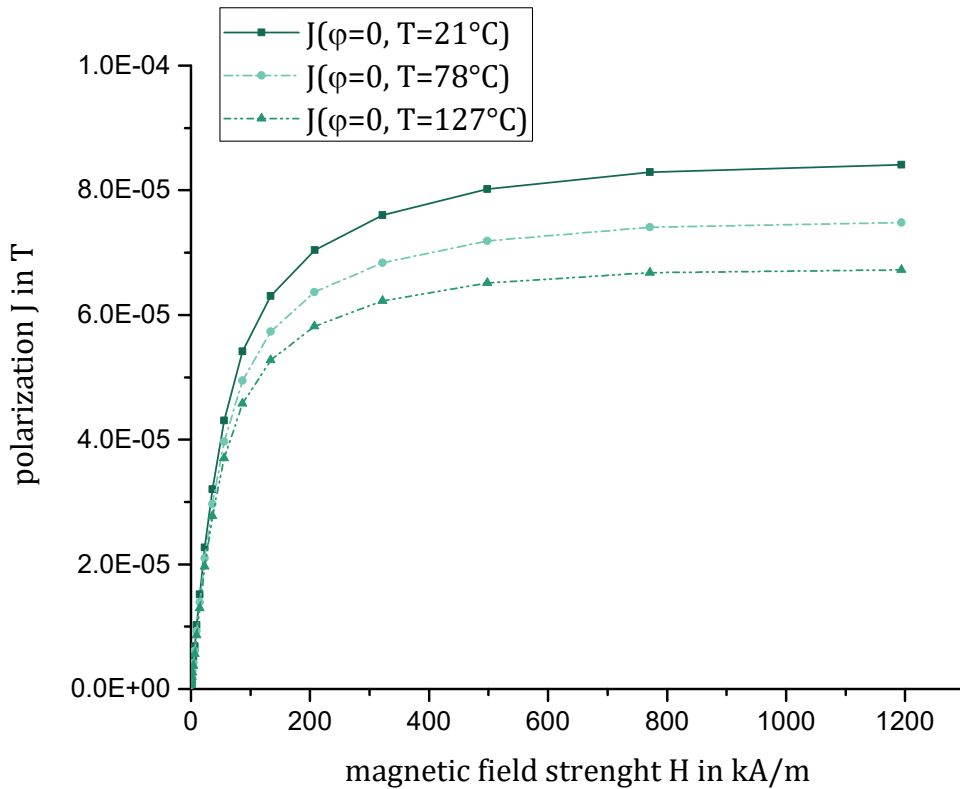
Figure 5.11: Initial polarization of FRP without magnetite

The polarization is increasing with decreasing temperature. For $T = 21\,°C$ the saturation polarization J_s is equal to $8.29046\,10^{-5}$ T. The value for J_s is positive for all regarded temperatures.

This means in consequence that the material behavior for the total CoFRTS is not diamagnetic. This is not expected as literature describes polymers as neutral [159, 160] in magnetic fields and carbon fibers as diamagnetic [89, 90]. The discrepancy could be based in contaminants such as metallic particles introduced by abrasion of the equipment used for mixing, impregnation, molding and milling of the material. Still J_s is small especially compared to FRP containing magnetite.

The initial polarization curves of CoFRTS containing magnetite are shown in Figure 5.12.
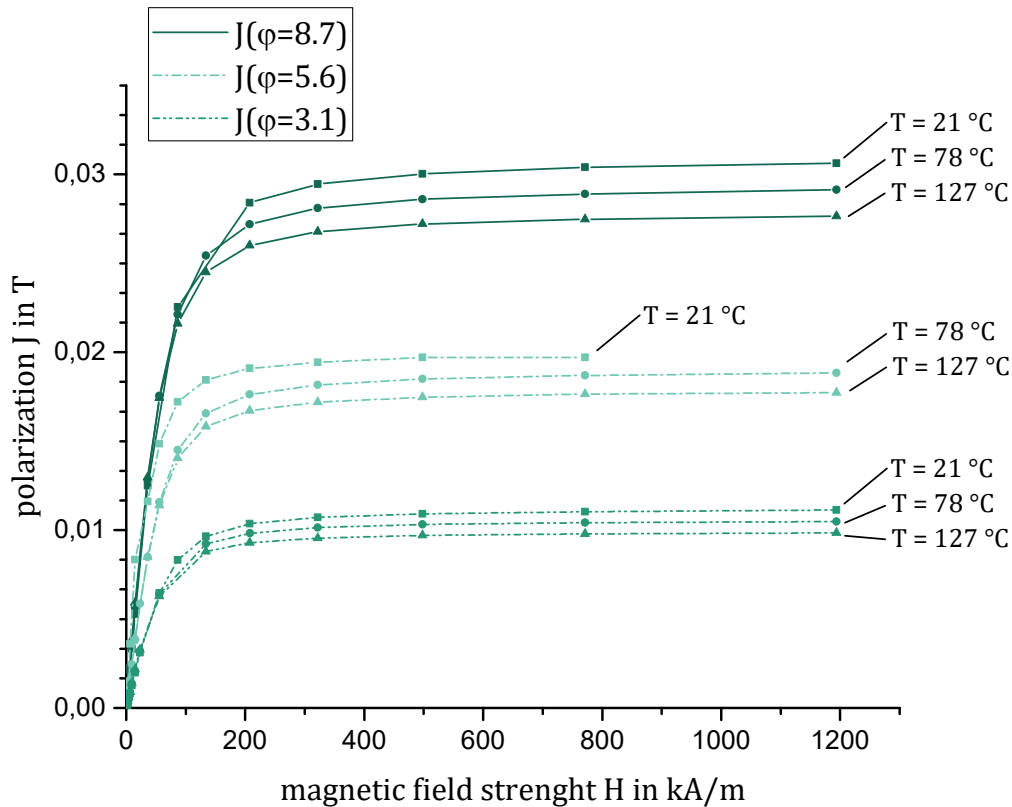
Figure 5.12: Initial polarization of FRP containing magnetite

The saturation polarization is increasing with rising magnetite content and decreasing with increased temperature. The measurements are plausible and will be used to model the material behavior in magnetic fields in the following.

5.4 Modelling of Magnetic Properties

To define a CoFRTS formulation able to withstand the forces applied by co-molding for an actual application, the magnetic properties of the material have to be predictable as a function of external field, magnetite content and temperature. Equation (3-3) was used in the previous chapter to dimension the equipment of the process chain. This linear model considers the magnetite content and is based on two measurement series of pure magnetite at $T = 80\,°C$ and $T = 127\,°C$. Figure 5.13 (left) displays the match of this model with the measured values at $127\,°C$. The model shows the same curve characteristic, but overesti-

mates. Starting from an external field strength of 150 kA/m the model shows a relative error of $\approx 16\,\%$ for all three investgated magnetite contents.

An alternative empiric model was introduced with equation (3-4). Figure 5.13 (right) shows its match with the measurements. Again the characteristic of the curve is reproduced accurately but this time the model is underestimating. The absolute error is almost constant for all measurements. Thus, the relative error increases with decreasing magnetite content from $\approx 18\,\%$ for $\varphi = 3.1$ vol.$-\%$ to $\approx 27\,\%$ for $\varphi = 8.7$ vol.$-\%$.
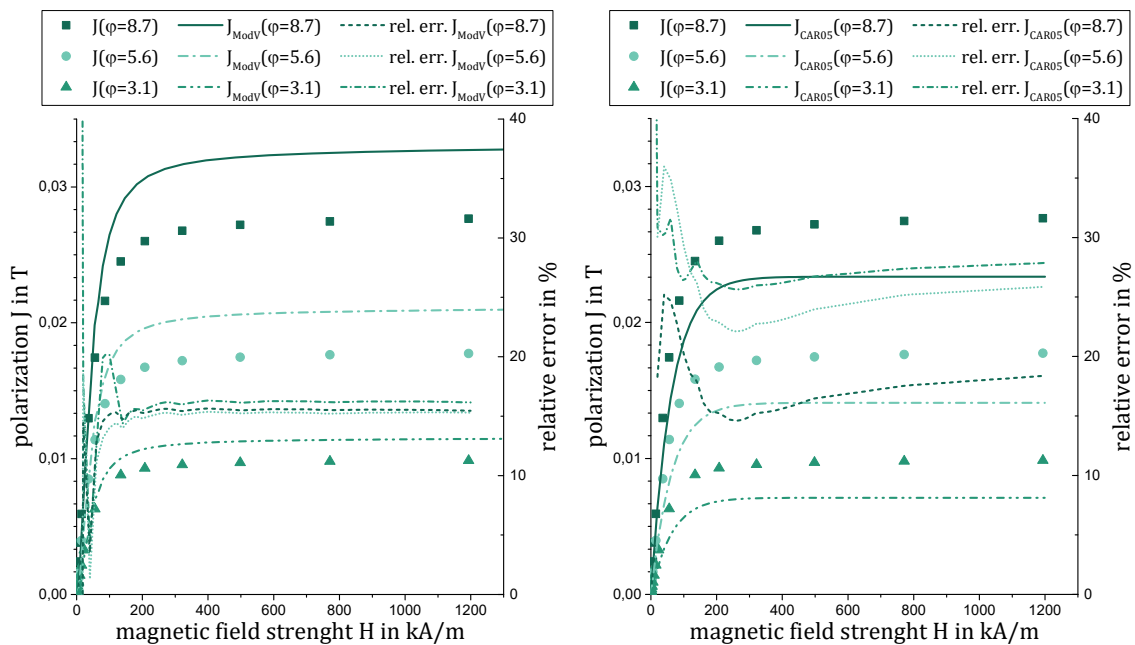
Figure 5.13: Polarization prediction and measurement results for *T*=127 °C
        left: Volume model based on equation (3-3)
        right: Empiric model based on equation (3-4)

Both, the volume model and the empiric model, describe the $J(H)$ depency for a magnetite content from zero to 100 % and are developed by means of measurements of pure magnetite. Thus, they are showing a high relative error especially for small magnetite amounts. As there is a negative effect of magnetite content on CoFRTS's total density and mechanical properties, φ should be as small as possible. At the basis of

the magnetic measurements of the compound an adapted model can be found, which is more suitable for small magnetite contents:

$$J = C_1 \varphi \left(1 - e^{(-C_2 \mu_0 H)}\right) \tag{5-3}$$

Hereby, the power of φ is 1 instead of 1.133 as ordinarily suggested by [134]. A linear influence φ is physically more profound and also reported in [123]. Furthermore, a linear behavior was observed in the present measurements (compare Figure 5.14, left).

To use a maximum number of measuring points for the definition of the constants C_1 and C_2, the least square fit is performed based on the specific polarization for $\varphi = 3.1$, 5.6 and 8.7 vol. $-\%$ at a temperature of 127 °C. Thus, equation (5-3) rearranges to:

$$J/\varphi = C_1 \left(1 - e^{(-C_2 \mu_0 H)}\right) \tag{5-4}$$

with:

$$C_1 = 0.31401 \text{ T}$$
$$C_2 = 14.14078 \text{ T}^{-1}$$
$$\bar{R}^2 = 0.99932$$

to (compare Figure 5.14, left):

$$J_{\text{MathFit}}(T = 127\,°C, \varphi, H) = 0.31401\varphi\left(1 - e^{(-14.14078\mu_0 H)}\right) \tag{5-5}$$

To extend the empiric model by the influence of temperature, a term for the change of polarization by temperature is needed. Literature describes nonlinear temperature behavior of J_s of ferrimagnetica [84] for temperatures from absolute zero to their Curie-temperature ($T_{C\,Fe_3O_4} = 585\,°C$ according to [130]). But in the regarded process window the temperature influence on the saturation polarization J_s is linear (Figure 5.14, right) and can be described by:

$$\Delta J_{s\,\text{Temp}}(T, H = 770\text{kA/m})/\varphi = C_3 + C_4 T \tag{5-6}$$

with:

$$C_3 = -0.04492 \text{ T}$$
$$C_4 = 3.4979 \ 10^{-4} \ °\text{C}^{-1}$$
$$\bar{R}^2 = 0.97983$$
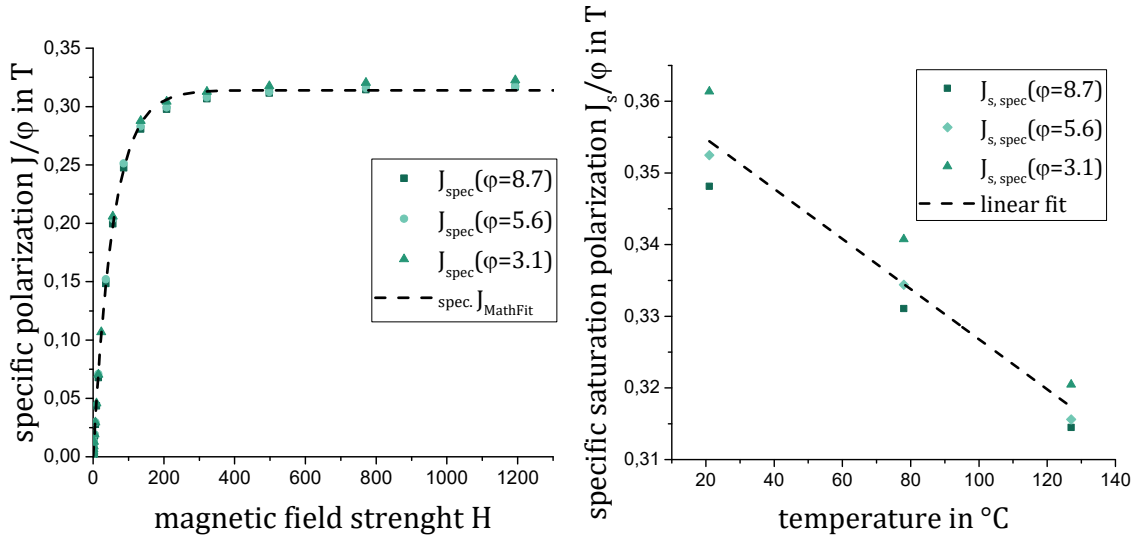
Figure 5.14: Specific polarization
left: Measurements and mathematical based fit at T=127 °C
right: Temperature influence on saturation polarization

Assuming the temperature influence for a changing magnetic field behaves directly proportional to the polarization at constant temperature, a more general equation can be formed. (5-7) describes the temperature induced polarization change:

$$\Delta J_{\text{Temp}}(T, \varphi, H) = \varphi(C_3 + C_4 T)\left(1 - e^{(-C_2 \mu_0 H)}\right) \tag{5-7}$$

Combined with formula (5-5):

$$J_{\text{emp}}(T, \varphi, H) = J_{\text{MathFit}} - \Delta J_{\text{Temp}} \tag{5-8}$$

a general expression for the polarization in relation to temperature T, magnetite content φ, and magnetic field H is found:

$$J_{\text{emp}}(T, \varphi, H) = \varphi\big(C_1 - (C_3 + C_4 T)\big)\big(1 - e^{(-C_2 \mu_0 H)}\big) \tag{5-9}$$

with:

$$C_1 = 0.31401 \text{ T}$$
$$C_2 = 14.14078 \text{ T}^{-1}$$
$$C_3 = -0.04492 \text{ T}$$
$$C_4 = 3.4979 \ 10^{-4} \ {}^{\circ}\text{C}^{-1}$$

Figure 5.15 shows the match of the developed model with the measurements. Figure 5.16 shows the corresponding relative error.
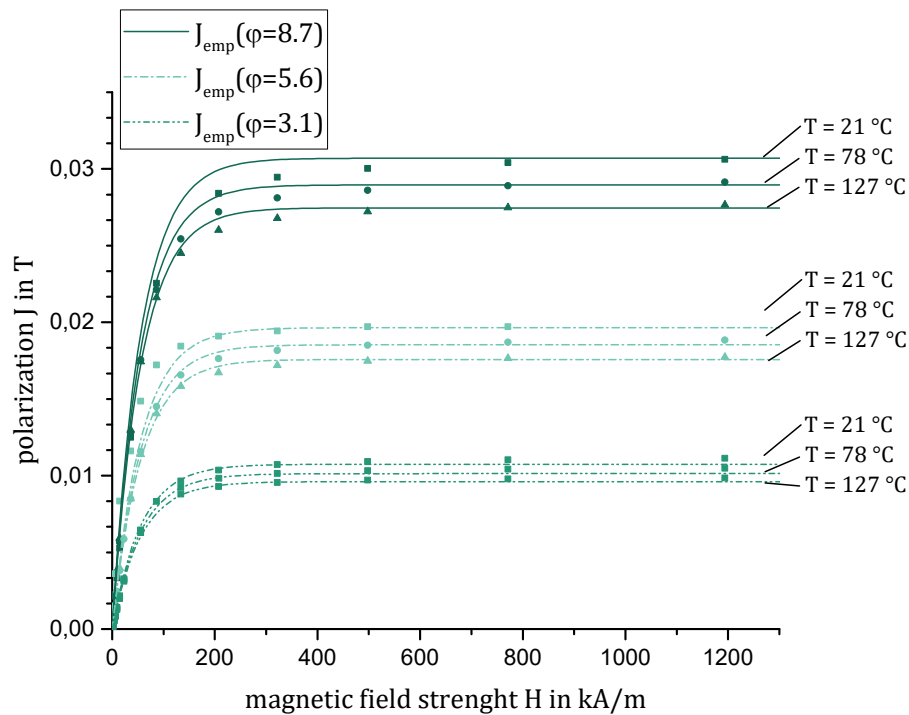
Figure 5.15: **Polarization prediction of equation (5-9) in contrast to measurement results (dots)**
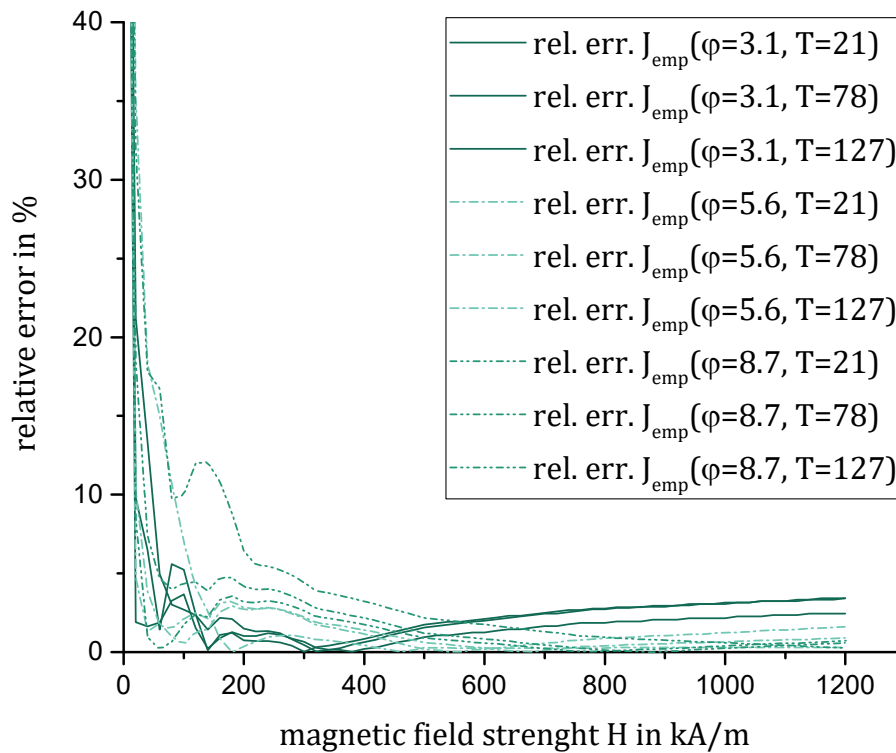
Figure 5.16: Relative error of polarization prediction of equation (5-9)

Starting with an external field strength of 300 kA/m the modell shows a relative error of less than 5 % for each single temperature to magnetite combination. The average relative error over the total measurement range is equal to 3.6 %.

Equation (5-9) delivers sufficient information to design CoFRTS formulation and processing equipment for any magnetite content till at least 8.7 wt. −% and any processing temperature in the range of 21 to 127 °C. As the temperature influence on polarization is strongly linear (compare Figure 5.14) in the regarded range, the error by extrapolating the dependency to 150 °C molding temperature should be negligible small. Furthermore literature describes a smooth and continuous function of polarization for ferrimagnetica until Curie temperature without sudden leap [84].

5.5 Deformation and Displacement of Local CoFRTS During Co-molding with DicoFRTS
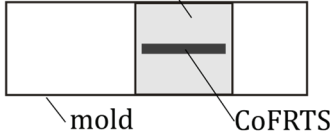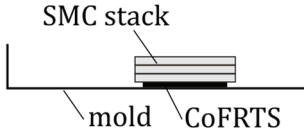
The hypothesis, that the fundamental requirement for a reliable co-molding is a stiff reinforcement as well as its fixation, is examined within this section. Molding trials were performed to either verify or refute the hypothesis. Part of the results are published within [16].

5.5.1 Methodology

First, CoFRTS materials of two different resin systems, with and without magnetite, are produced by the help of the manufacturing line described in section 4.1.2 on page 66. As resin systems, a state-of-the-art MgO-thickening UP resin and the UPPH resin are used. The powder *Bayferrox 318m* is used as ferrimagnetic filler for one half of the materials to enable magnetic fixation. Details about the formulations of the four different CoFRTS materials can be found in Table 8.6 in the appendix on page 143. After maturation the prepreg is CNC-cut (*Precision-Cutter G3* by *Zünd Systemtechnik AG*) into patches of $220 * 25$ mm. The molding is performed by a hydraulic press (*DYL630/500* by *Dieffenbacher GmbH*) and the $800 * 250$ mm sized mold. The mold is heated by oil to $\approx 145\,°C$ and is equipped with the permanent magnet inlay (compare section 4.3.2). For molding, one patch of CoFRTS is placed in the cavity exactly over the PMs. As a next step a stack of glass fiber reinforced SMC (DicoFRTS type *6419-01* by *Polytec GmbH*) is placed in the mold. The initial position of the patch is kept constant for all trials, but DicoFRTS position and mold coverage is changed (compare Figure 5.17):

(M33): The (M33) trials are characterized by a stack of three layers of DicoFRTS at a mold coverage of 33 %. The DicoFRTS charge is placed symmetrically on the CoFRTS patch, having full overlap. As this molding condition seems to be the most relevant for the SMC-industry, the trials are repeated by four iterations to investigate reproducibility.

(S33): For (S33) condition the same stack and mold coverage is used as for (M33) trials, but the charge is placed next to the patch without any overlap of the patch and DicoFRTS.

(S66): Here the mold coverage is increased to 66 % and the stack height is reduced to two layers of DicoFRTS. The CoFRTS patch is fully covered by DicoFRTS.


Figure 5.17: DicoFRTS mold coverage and patch position during co-molding [16]

After placing the materials, the process of compression molding is started. The closing speed of the press is set to 1 mm/s, the final pressure is 50 bar as a standard. Additionally, some plates are molded at 75 and 100 bar according to an experimental plan generated by the help of a design of experiments (DoE) software (*Modde* by *Umetrics AB*). The cure time is 120 s, the parallelism control of the press is activated.

After demolding the lower side of each plate is photographed rectangular to its surface. To measure position and geometry of a patch in reference to its initial position, the image analysis software *ImageJ* provides several algorithms. A "rolling ball" algorithm is used to subtract

the smooth change in brightness over the total length of the CoDico-FRTS plate [161].Furthermore, the colors of the image are converted into grey values. In a next step the dark carbon fiber reinforced patch can be separated from the bright glass fiber reinforced SMC by using a threshold for the grey value. Now, the centroid of the patch as well as a bounding rectangle drawn around the patch is measured in the systems of coordinates of the plate. This enables to calculate key values for the two main failure mechanisms of the patch during co-molding: displacement and deformation (compare Figure 5.18). The displacement is expressed as a vectorial shift d in mm of the patch's centroid and as a rotation β in deg of the bounding rectangle. The deformation is described by a change in width and length (Δw, respectively Δl in %) of the bounding rectangle in relation to the initial shape of the patch.
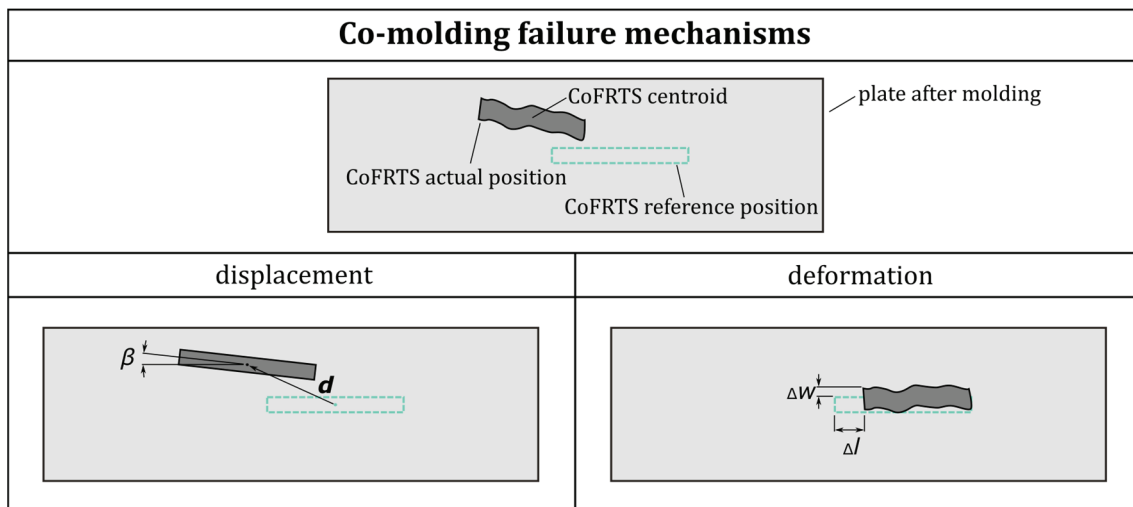
Figure 5.18: Failure mechanisms of CoFRTS patch [16]

5.5.2 Results and Discussion

Visual inspection of the plates and image processing shows a clear dependency of molding conditions, resin system and magnetic fixation on molding result. Figure 5.19 displays exemplary pictures of the plates after molding.
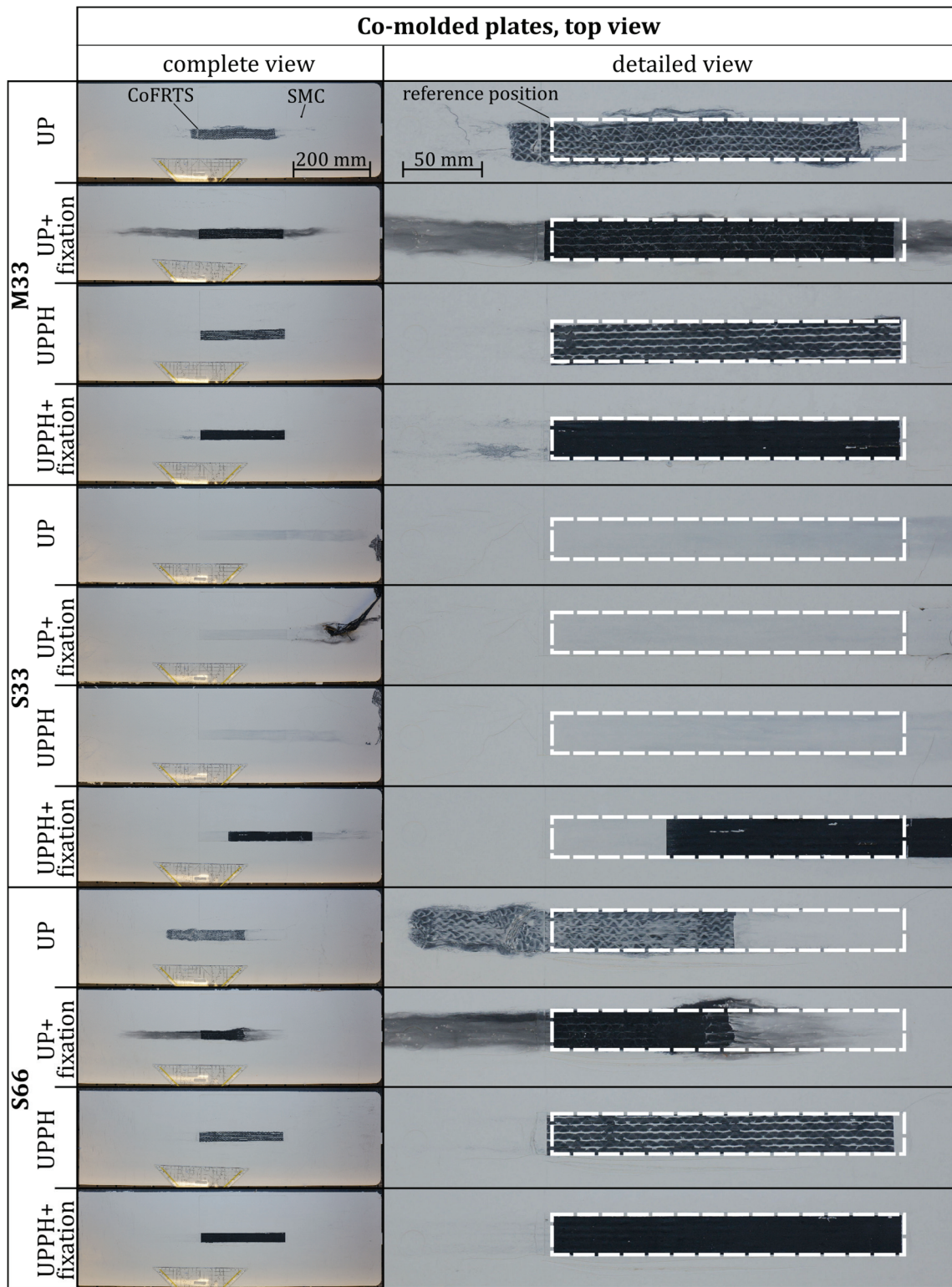
Figure 5.19: Pictures of the patch reinforced plates after molding

Figure 5.20 shows the calculated key values for (M33) condition with the corresponding standard deviation as these trials are reproduced by four iterations.
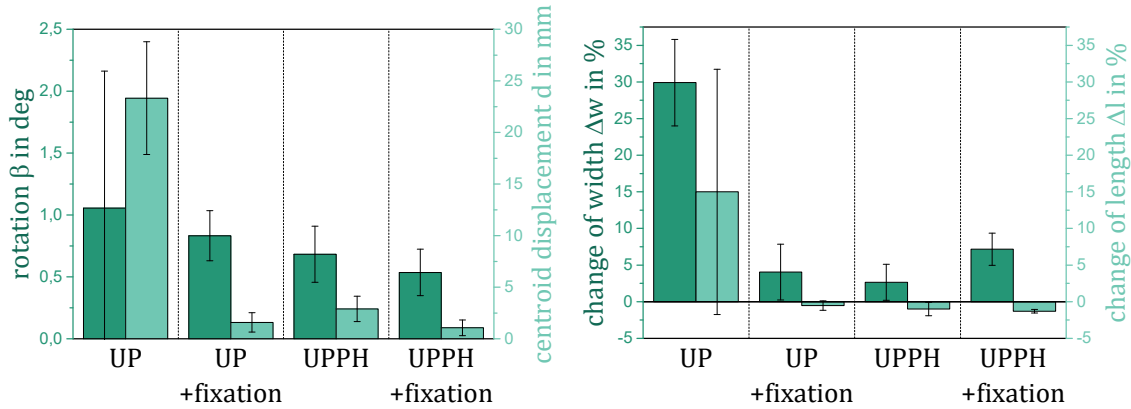
Figure 5.20: Key values for (M33) molding conditions
left: Displacement
right: Deformation

In the following the results are discussed ordered by molding conditions:

(M33): This molding condition is characterized by a full and symmetric overlap between patch and DicoFRTS charge. The flow of DicoFRTS is one-dimensional. As a result the rotation of the patches is negligible small (≈ 1 deg), independent of resin system and fixation. However, patches of UP resin without fixation are showing with 1.1 deg highest standard deviation (Figure 5.20, left). For all other experiments the deviation is less than 0.2 deg.

As the position of the charge is symmetrical to the patch but not to the mold, there is a change in flow during molding. The first one-dimensional but two-directional flow of DicoFRTS will change just before the complete filling of the mold to a one-directional flow. In the first phase, the displacement forces acting on the patch should compensate each other. In the second phase there should be a displacement force for a short period of time. Indeed, the patches are displaced in the direction of flow of this second molding phase (Figure 5.19,

(M33)). The state-of-the-art material (UP resin, no fixation) shows a vectorial displacement of 23 mm. This displacement can be reduced to less than 3 mm by switching the resin system to UPPH, adding magnetite for an additional fixation or doing both (Figure 5.20, left). The deviation is reduced from 5.5 mm for the reference material to maximum 2.2 mm for the others.

The results appear to be similar for the patches deformation (Figure 5.19, (M33)). Using UPPH resin and/or fixation reduces the deformation in width from 30 % to 7 % or less (Figure 5.20, right). The influence on the change in length is not significant. But again an improvement in reliability can be observed, which is reflected in a smaller standard deviation. The 6 % deviation in width and 17 % deviation in length can be reduced to 4 % respectively 1 % or less by using either UPPH resin or fixation or both.

Furthermore, the magnetic particles are washed out when using UP resin as matrix (Figure 5.19, (M33)).

(S33): The flow of this molding condition is completely one-directional. The DicoFRTS stack has no overlap. Therefore, there is no normal force on the patch applied by the press and transferred by the DicoFRTS at the time the flow front arrives at the patch.

Consequently, this molding condition leads to high deformation and displacement in most experiments. Only the combination of UPPH resin and magnetic fixation is able to prevent massive deformation and limits the displacement of the patch (Figure 5.19, (S33)).

(S66): For this molding condition, the patch is completely covered with DicoFRTS prior to molding. The flow is one-directional from the start. This leads to a displacement force on the patch during the whole process of mold filling.

The rotation is negligible small for all patches. The UP resin based materials show high deformation, often by buckling and

108

independent of the fixation. The UPPH materials were keeping their shape. Magnetic fixation reduces the vectorial displacement (compare Figure 5.19, (S66)). Again, the magnetic particles are washed out when using UP resin (Figure 5.19, (S66)).

The calculated key values for displacement and deformation are used as response input for the DoE software *Modde 9.1*. The software is configured to use multiple linear regression (MLR) to fit the observed data to a linear model. Hereby, singular value decomposition (SVD) is applied to solve the system of equations [162]. MLR and SVD are described in literature [163, 164].

The models for β, Δw and Δl are showing an unsatisfactory model quality and will thus, be not considered any further. The quality of the model for the key value of highest interest, centroid displacement d, is sufficient. It shows a R^2 of 0.82, a Q^2 of 0.73 and a model validity of 0.76 at a reproducibility of 0.82. Therefore, a regression coefficient plot can be used to determine significance and general impact of the parameters. Figure 5.21 shows this plot data centered [162] for the centroid displacement. Molding pressure as well as the molding condition (S66) are not significant for the vectorial displacement. Molding condition (M33) shows a positive effect, (S33) a strong negative effect. On the material side the presence of magnetite (fixation) shows the highest effect and leads to a general reduction of centroid displacement. Thus, the effect of the fixation is higher than the effect of the UPPH resin.
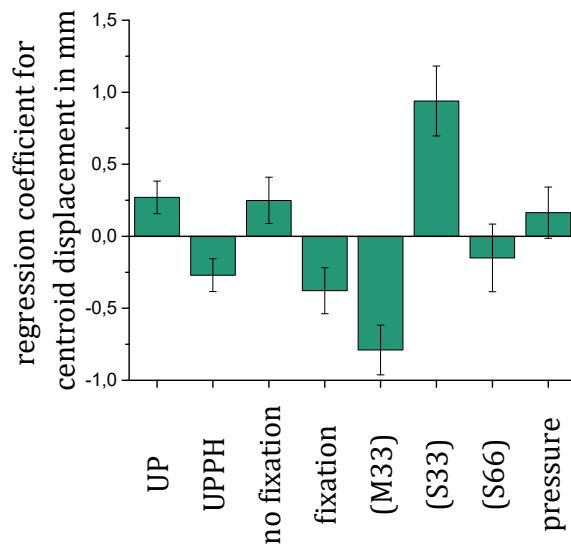
Figure 5.21: Overall impact of parameters on centroid displacement

In summary, both parts of the hypothesis were confirmed. For unfavorable process conditions, like (S33), a fixation as well as a stiff reinforcement is essential to limit displacement and deformation. The difference in viscosity drop of UP resin to UPPH resin when placed in the hot mold is reflected by a wash out of magnetic particles for the conventional thickened resin system. If the displacement forces mostly compensate each other, like for (M33) conditions, one of these improvements can be sufficient. Along all experiments, the molding conditions placement of DicoFRTS charge and mold coverage showed the highest impact on the outcome. On the material side the fixation has the highest impact.

5.6 Simulation of Magnetic Fixation Force

The molding trials in the previous sub-section identified the fixation as a main factor to reduce displacement during co-molding. This force shall be investigated more deeply as a consequence. For the following calculations, the software FEMM and the model introduced in Section 4.3.2 are used. This time the magnetic properties of the CoFRTS patch are modeled by formula (5-9) instead of using (3-3). This allows a pre-

cise description of the molding conditions showed in Figure 5.17: the height of the reinforcement is 0.45 mm, the magnetite content φ is 8.21 vol. $-\%$ and the molding temperature is set to 145 °C.

The fixation force calculated accordingly is shown in Figure 5.22 in relation to the stamp distance. Hereby, the stamp distance reflects the height of the cavity. In an open mold, the initial fixation force is 4.5 N. At the moment the stamp hits the stack of DicoFRTS material the force is 5.1 N for (M33) conditions. Afterwards it drops to finally 4 N, when the cavity is fully filled.
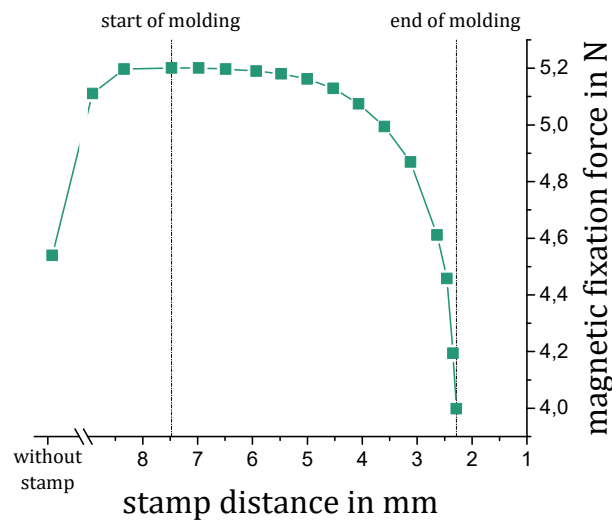
Figure 5.22: Magnetic fixation force during co-molding, (M33) conditions

5.7 Simulation of Co-molding

To investigate the forces acting on the reinforcement during co-molding, mold filling simulations are performed. The Software *Mold-ex3D R14* by *CoreTech System Co., Ltd.* is used for this purpose.

5.7.1 Methodology

The simulation is built up for the molding conditions of highest impact (M33) and (S33), according to Figure 5.17. The dominant factors for

the co-molding forces are the processing parameters and the Dico-FRTS's viscosity. The processing parameters are set according to the trials shown in section 5.5 to:

- Stamp closing speed: 1 mm/s.
- Final pressure: 50 bar, equals press force of 1 000 kN.
- Mold temperature: 145 °C.
- Time between placement of charge and start of molding: 3 s.

In this study, the viscosity of the DicoFRTS is described as a function of temperature T and shear rate $\dot{\gamma}$ according to the extended Cross model introduced in section 2.9.2. The material parameters for this are based on the *CAE-BMC-1* material of the *Moldex3D R14* materials library. This BMC material-model was then adjusted (see section 8.5 in the appendix) to fit SMC literature values and the material behavior, observed at the molding trials, as follows:

- The curing of the DicoFRTS is neglected as the fill time of the cavity is less than 20 s [165].
- Literature values [165] are used to describe the thermal material properties (thermal conductivity and heat capacity).
- The filler as well as the fiber content of the provided *CAE-BMC-1* material data is unknown. Thus, its viscosity curve in the logarithmic viscosity versus temperature graph was shifted to fit values reported by Ritter for a similar DicoFRTS material under similar molding conditions [106].

The reinforcement is modeled as a solid as it is supposed not to deform or to displace during co-molding. Its temperature is set equal to the mold temperature, since:

- The reinforcement's height is relatively small (0.45 mm).
- The reinforcing carbon fibers are showing a high thermal conductivity ($\lambda_{\text{CF}} = 15$ to 40 W/mK, [9]).

- The patch is placed several seconds prior to the DicoFRTS charge in the mold. Thus, it is assumed that the patch has sufficient time to heat up.

After computation of the model, the data is analyzed on the basis of measurement nodes, which are shown in Figure 5.23. The nodes 1-3 are placed on a xy-plane on the surface of the reinforcement. The nodes 4 and 5 are located at the short side face of the reinforcement on yz-plane. Nodes 6 to 8 are placed at the end of the cavity in yz-plane. They are used to monitor the change in flow direction for (M33) conditions only. Each node delivers the following information, which is saved for analysis at defined time steps:

- Resin front time in s.
- Shear stress in kPa.
- Shear rate in 1/s.
- Pressure in MPa.

The global model parameters press force (in kN), stamp distance (in mm) and mold filling (in %) are saved at a higher time resolution ($\approx$ 2 Hz).
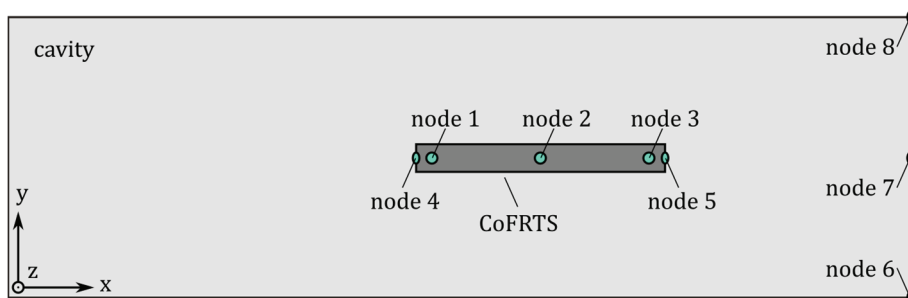
Figure 5.23: Position of measuring nodes for process simulation

5.7.2 Results and Discussion

The simulated press force, shear stress and normal pressure are shown for selected nodes in relation to the stamp distance in Figure 5.24 and Figure 5.25.
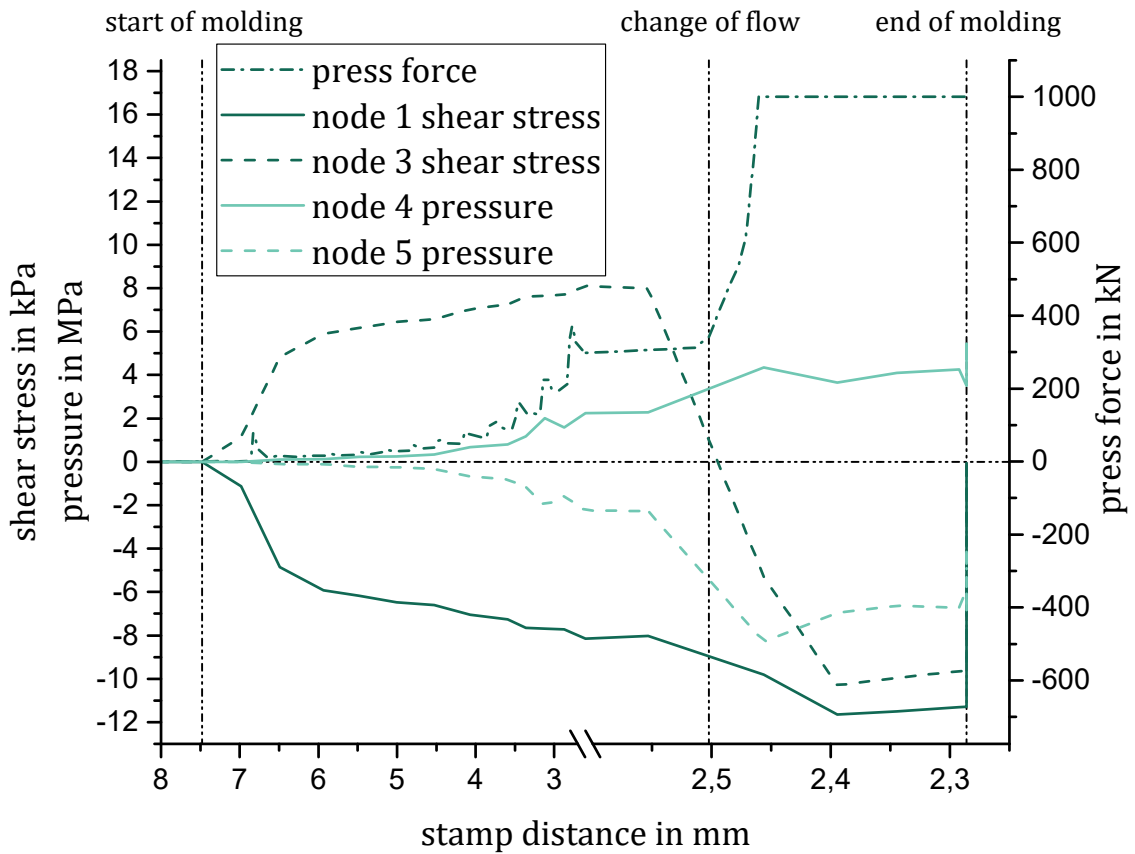
Figure 5.24: Forces on CoFRTS during co-molding, (M33) conditions
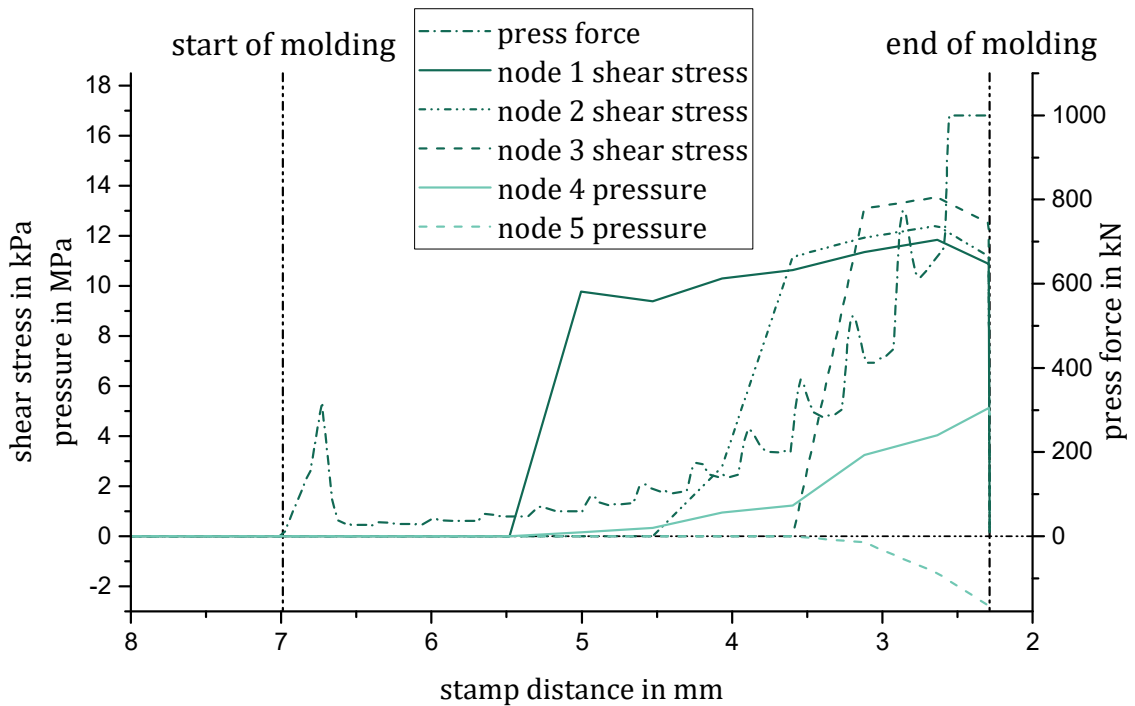
Figure 5.25: Forces on CoFRTS during co-molding, (S33) conditions

The forces on the patch for (M33) conditions are balanced over a long period of the molding process (compare Figure 5.24). The shear stress for node one and three as well as the normal pressure on the short side faces of the reinforcement setoff each other. This is caused by the symmetrical position of the charge to the patch and the two-directional flow of DicoFRTS. At a stamp distance of 2.55 mm the flow gets unsymmetrical and is finally one-directional at a stamp distance of 2.50 mm. This corresponds to a mold filling of 91 % and is visualized by the line "change of flow" in Figure 5.24. At this line, the sign of the shear stress of node three changes. The absolute normal pressure on the face side looking against flow direction (node five) increases faster than the pressure in flow direction (node four). At the very moment the flow changes, the press force increases as well, from ≈ 300 kN to the final pressure of 1 000 kN. A complete filling of the mold is achieved in 5.3 s.

For (S33) conditions the force is unbalanced from the beginning (see Figure 5.25). The shear stress increases from zero to ≈ 12 kPa at the very moment the flowing DicoFRTS reaches the nodes one to three. The press force required to keep the closing speed at 1 mm/s increases constantly, until the final pressure is established. This occurs at a stamp distance of 2.55 mm, which equals a mold filling of 90 %. The mold is fully filled after 4.7 s.

There is a peak in press force visible at the moment the stamp first touches the stack of material. This peak is more pronounced for (S33) conditions. Here the whole lower surface of the DicoFRTS stack is in contact with the mold. A respectively high force is needed to keep the stamp velocity constant as the full stack of DicoFRTS has to start flowing in x-direction at a high viscosity, due to the low shear stress. For (M33) conditions, the DicoFRTS stack is placed on top of the reinforcement. Thus, the molding force is concentrated on this small region at the beginning, resulting in a high shear stress and lower local viscosity. Furthermore, the DicoFRTS material is able to flow in several directions. The DicoFRTS flows as well in positive as in negative x-direction

and it fills the space between DicoFRTS stack and mold-cavity around the patch in y-direction (compare Figure 5.17). This reduces the peak in press force significantly.

In summary, the simulation delivers plausible results. For (M33) conditions, a force on the reinforcement opposite to x-direction results at the moment the flow changes from two-directional to one-directional flow. At sidewise placement of the charge (S33), there is a force in x-direction as soon as the DicoFRTS flow reaches the patch (stamp distance 5.9 mm) till the end of mold filling.

However, the closed box approach of moldex3D for modelling the material flow and the mold-material interface is leading to considerable uncertainty of the simulation results. This is further exacerbated by the fact that the material model is based on literature values only. Nevertheless, the performed simulations are able to uncover the dominant forces during co-molding and to provide a more fundamental understanding of the effects, when changing process conditions.

5.8 Mechanics of Local CoFRTS During Co-molding

This section is combining the single characterization and simulation results showed before in order to investigate the forces acting on the CoFRTS during co-molding in its entirety. Thereby the focus is placed on the displacement of the reinforcement. The molding conditions (M33) and (S33), introduced in section 5.5, are examined more closely. Furthermore, the material systems are limited to the UP-based CoFRTS as reference and the UPPH-based material containing 8.21 vol.$-$% of magnetite.

5.8.1 Methodology

Figure 5.26 illustrates a two-dimensional cross-section of the planar co-molding trials with respect to the forces on the CoFRTS material.
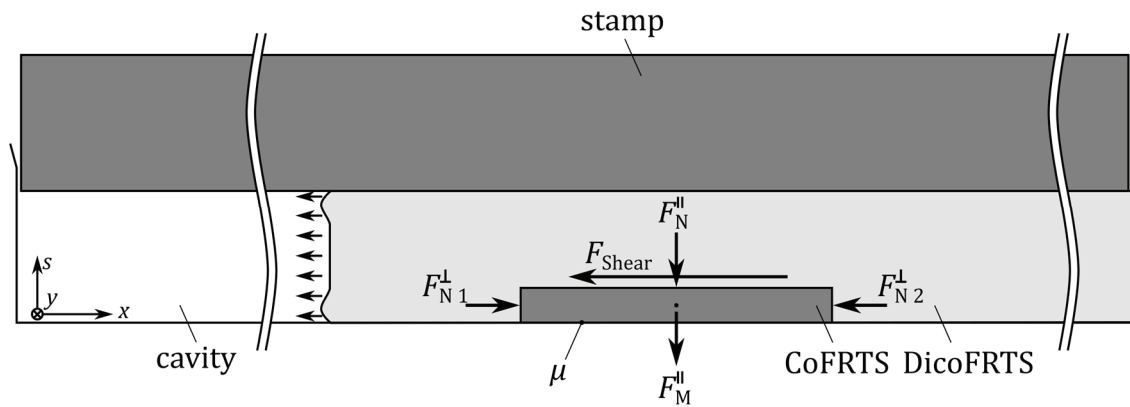
Figure 5.26: Forces on CoFRTS during co-molding, schematic for (M33)

The normal force F_N is applied by the hydraulic press. The magnetic force F_M is applied by the magnetic field. The proportions of these forces acting in molding direction are beneficial for the fixation. However, friction is needed to transfer these forces into the direction of the displacement. The total fixation force F_{fix} is consequently calculated as follows:

$$F_{fix} = \mu \, F^{\parallel} = \mu \left(F_N^{\parallel} + F_M^{\parallel} \right) \tag{5-10}$$

$$F_N^{\parallel} = f(press \ force, \ mold \ filling)$$

$$F_M^{\parallel} = f(H, \varphi, T)$$

As shown in section 5.6, the magnetic fixation force $F_M^{\parallel}$ can also be expressed as a function of the stamp distance s, using FEM-software for this two-dimensional problem:

$$F_M^{\parallel} = f(s, \varphi, T)$$

with: $\qquad\qquad T = 150 \, °C$

$$\varphi_{UPPH} = 8.21 \ vol. -\%$$

Obviously $F_M^{\parallel}$ is equal to zero, if there is no magnetite present in the formulation.

For a conservative and fail-safe design the dynamic friction coefficients determined in sub-section 5.1 are used:

$$\mu_{\text{Dy}} = f(resin, T)$$

$$\mu_{\text{Dy UP}}(T = 150\,°\text{C}) = 0.139$$

$$\mu_{\text{Dy UPPH}}(\varphi = 8.21\,\text{vol} - \%, T = 150\,°\text{C}) = 0.527$$

Forces acting perpendicular to the molding direction will directly result in a displacement force F_{dis} of the reinforcement, if not balanced or compensated by the fixation forces:

$$F_{\text{dis}} = F_{\text{N}\,1}^{\perp} + F_{\text{N}\,2}^{\perp} + F_{\text{Shear}} \qquad\qquad \textbf{(5-11)}$$

The normal forces as well as the shear force are determined by the mold-filling simulations shown in sub-section 5.7. The CoFRTS itself is considered to be rigid. Furthermore, the magnetic force in y-direction, the force on CoFRTS by gravitation and the force on CoFRTS lateral surfaces in x/s-plane are small and therefore neglected.

Displacement of the reinforcement should occur, if the forces perpendicular to molding direction are unbalanced ($F_{\text{dis}} \neq 0$) and in addition are not compensated by the fixation force ($F_{\text{fix}} < |F_{\text{dis}}|$). Hereby, the sign of F_{dis} specifies the displacement direction.

5.8.2 Results and Discussion

Figure 5.27 shows the fixation force as well as the displacement force in relation to the stamp distance for two different molding conditions and the two materials.
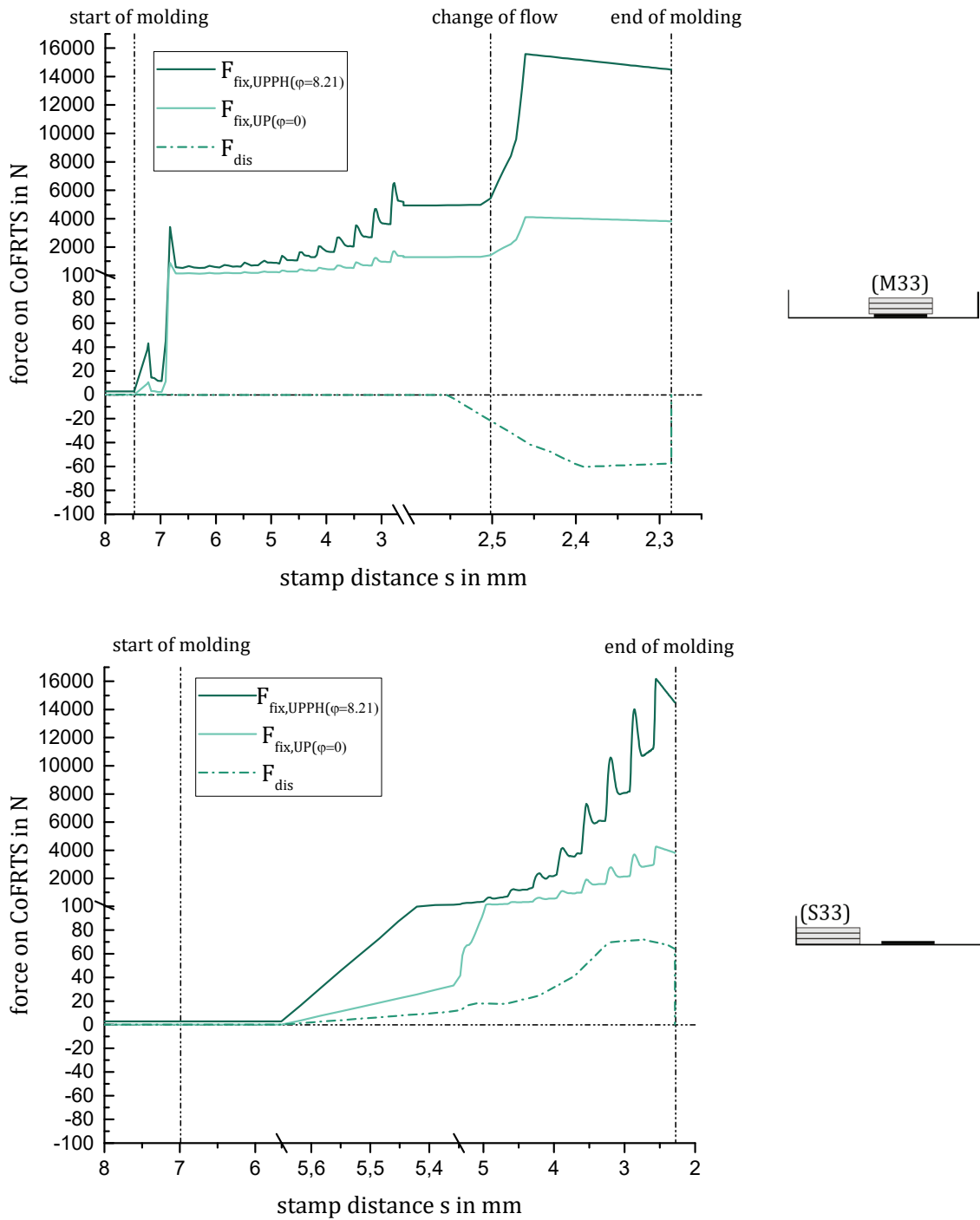
Figure 5.27: **Calculated forces on CoFRTS during co-molding**
top: Full overlap of initial charge with CoFRTS (M33)
bottom: No overlap of initial charge with CoFRTS (S33)

The results are discussed separate for each molding condition:

- The fixation force of the (M33) condition starts at zero for the UP-based material and at 3 N for the UPPH material, because of the magnetic fixation (compare Figure 5.27, top). At the moment the stamp gets in contact with the initial charge, the fixation force increases as this molding condition is characterized by a full overlap between initial charge and CoFRTS. Consequently the starting flow of DicoFRTS is at first two-directional and symmetrical to the reinforcement. Thus, the displacement force is balanced and equal to zero for this molding period. As the position of CoFRTS is not symmetrical to the mold, the flow changes towards the end of the molding process to a one-directional flow in negative x-direction. At this moment the displacement force gets unbalanced. At the same time the fixation is strong as there is high press force needed to keep the molding velocity constant, while the strain rate of the CoFRTS increases.
- For (S33) condition, the fixation force as well as the displacement force start to increase simultaneously at the moment the flow front hits the CoFRTS (compare Figure 5.27, bottom). However, the gradient of the fixation force is higher for both material types than the gradient of the displacement force. Again, there is a shift in fixation force for the UPPH material, because of the magnetic fixation. In contrast to the (M33) condition, the displacement force is positive and therefore pointed in the other direction.

In summary the fixation force is higher than the displacement force for all molding conditions and material systems. Therefore, a reliable co-molding process showing no displacement of the CoFRTS would be expected. However, the experiments showed small displacement for (M33) conditions and large displacement for (S33). Also a stronger influence of the resin system and the magnetic fixation was observed. These differences between experiment and simulation may have several possible causes:

- For the simulation of (S33) condition and UP-based material, the fixation force and displacement force start at the very same moment of mold filling: the point the DicoFRTS hits die reinforcement. The fixation force of the press can only be transferred to the CoFRTS, if the reinforcement stays in place and the DicoFRTS is flowing over it. This condition is assumed for the mold filling simulation. If the flow front of DicoFRTS is just pushing the CoFRTS in front of itself, there is no fixation and therefore high displacement. This behavior was observed for several experiments with no magnetic fixation. If magnetite is present in the formulation, the fixation force of the magnets appears during the whole molding process, thus also at this critical moment. It is probable, that this indeed small force affects the difference between an unstable process und a stable process. To investigate this more deeply Figure 5.28 shows a breakdown of displacement and fixation forces in x-direction. Hereby, $F_N^{\perp}$ is based on the press force in x-direction, but adjusted by the actual mold filling and converted in y-direction by the friction coefficient. This force is able to compensate the shear force of flowing DicoFRTS and the force acting on the reinforcements face side (compare Figure 5.26). However, shear strength as well as $F_N^{\perp}$ appear only, if the reinforcement stays in place. For a flow front pushing and moving the reinforcement, there will be only the force on the face side. As Figure 5.28 shows, the magnetic fixation all alone is able to compensate this force for a long period of the molding process and in particular for the critical moment of the first contact. For formulations without magnetite, the magnetic fixation force is zero. The result is

an unstable molding behavior, depending on whether the CoFRTS stays in place for its first contact with the flow front or not.
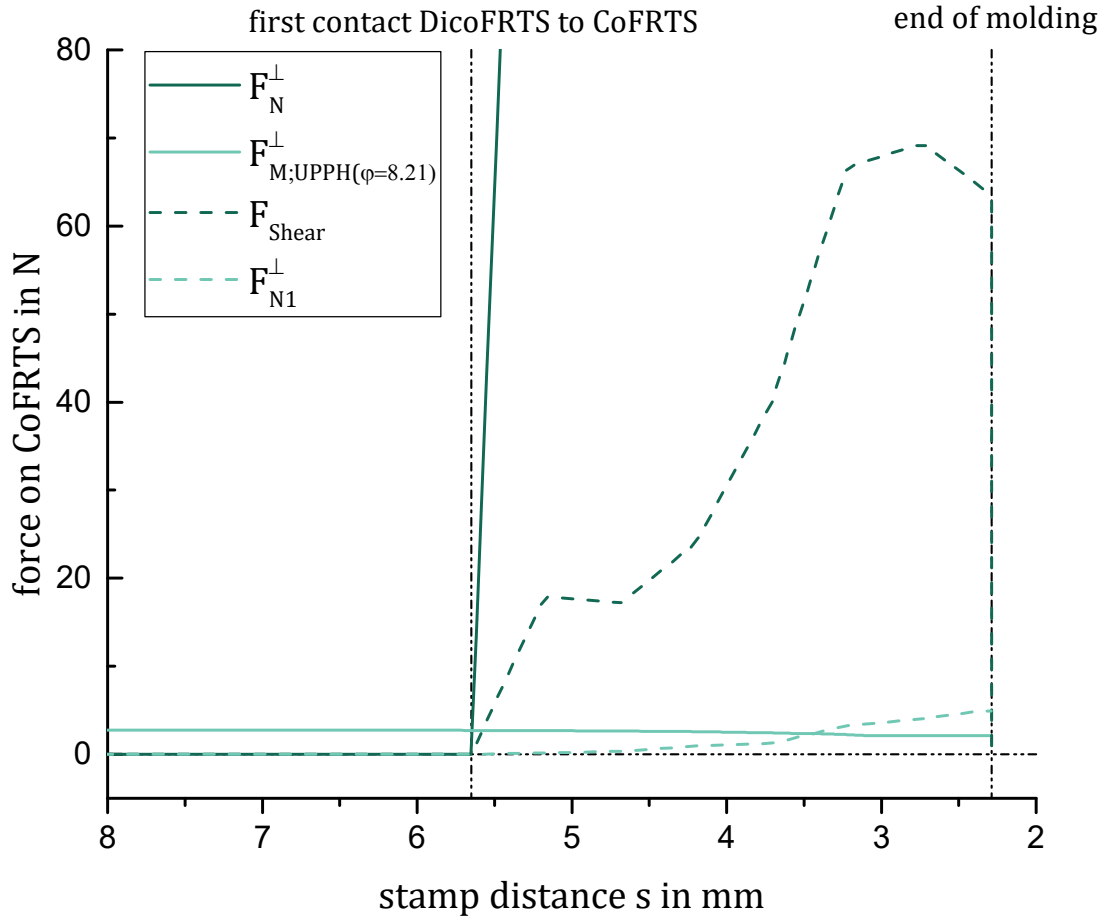
Figure 5.28: Breakdown of fixation and displacement forces for (S33) conditions

- The reinforcement is modeled as a solid having infinite stiffness. In reality the CoFRTS is limb under bending, especially for the UP-based materials at molding temperature. Thus, there is little resistance against a local lift of the reinforcement from the material itself. This local floating can either be caused by harsh molding conditions, like (S33), or local deviations in pressure because of macroscopic inhomogeneity of the DicoFRTS. It has high impact on the effective fixation force applied by the press as the force is transferred by the low-viscous DicoFRTS. For a floated section of the reinforcement, pressure will exist on the top side and the bottom side of the reinforcement and thus balance each other out. So there is no

fixation by the press for this area. Furthermore there is no restoring force to push back the DicoFRTS except that of the bending stiffness for state of the art material and processing. This creates an unstable situation. Both, the higher bending stiffness of the B-staged UPPH-based materials as well as the magnetic fixation are beneficial to prevent local floating. Furthermore the magnetic fixation also applies for local floated sections and is able to push back DicoFRTS material flown under the CoFRTS to a certain extent. Consequently a more stable mechanism for applying the high fixation force of the press is found resulting in a more reliable co-molding. However, this mechanism is not implemented in the mold filling simulation used here. Obviously, this limits the outcome of the simulation.

- Modelling the interface between flowing DicoFRTS and mold respectively reinforcement, is nontrivial and has not yet been satisfactorily solved [105]. The software used for the current investigation, *Moldex3D R14*, gives the possibility to describe this interface either with slip at a constant friction coefficient or by no-slip at all [166], which is insufficient. The friction for example is strongly dependent of the temperature and the time exposed to temperature, as shown in sub-section 5.1. Influence of temperature and shear rate on slip behavior is also reported in [106]. According to more recent studies, the interface should be modeled by thermodynamical friction (proportional to the materials relative velocity [167]), as DicoFRTS provides a thin lubricating paste layer [168]. However, this is not implemented into commercial tools, yet. As the modelling of the interface will have major impact on the main displacement mechanism shear, a significant error is estimated by using a constant boundary condition independent from shear rate, temperature or viscosity.

5.9 Draping

Three different draping concepts were introduced in section 4.2: manual, stamp and magnetic draping. Here these concepts are analyzed for their capability of draping UPPH based CoFRTS patches. For the exper-

iments the cross beam sub-preform of the subfloor reinforcement is produced, measured and analyzed (compare Figure 4.1). For this thesis the extent of the investigation is limited to a summary of four exemplary layer structures. Broader investigations can be found in the master thesis "Comparison of the preform quality produced by different processes for the manufacturing of reinforcement structures out of prepreg materials" of A. Damm.

5.9.1 Methodology

CoFRTS material is produced according to the formulations shown in Table 8.7 (annex on page 145). The basis for all materials is the UPPH resin. For draping with the magnetic draping device, 8.82 vol. $-\%$ of magnetite are added. The CoFRTS is CNC-cut (*Precision-Cutter G3* by *Zünd Systemtechnik AG*) and stacked (manually) directly after impregnation. Hereby, four different layer structures are realized, according to Figure 5.29.
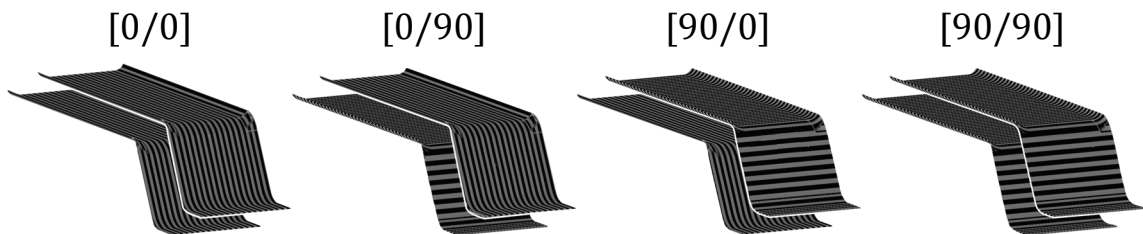
Figure 5.29: **Different layer structures of sub-preforms**

The CoFRTS is then preformed by the three different devices explained in section 4.2. Two sub-preforms are draped in parallel. The procedure is iterated three times. The heating of the different molds is used for $\approx$ 13 min at 80 °C to fully finish the first reaction step. This time period is chosen to ensure a chemically stable first reaction step. For mass-production the heating time can be reduced, but first must be further investigated. In this stage the sub-preforms would be ready for assembling to the complete preform and co-molding. Of interest within this thesis is the geometrical accuracy of the draping devices. Thus, the sub-preforms are placed in an oven for 30 min at 120 °C. This initiates the

second reaction step and leads to a fully cured and hence stiff sub-preform, ideal for measuring.

The surface of each sub-preform is then digitized at the *Baden-Württemberg Cooperative State University*, located in Karlsruhe. It is measured by laser triangulation with a *ROMER Absolute Arm 7320SI* by *Hexagon Metrology*. In a next step the sub-preforms actual geometry is globally compared to the target geometry, using the software *Geomagic Contr*ol by *Geomagic GmbH*. First outliers are removed and the point cloud is transformed to a consistent surface of polygons. The comparison result is the deviation of each polygon of the sub-preforms surface as a normal vector originating from the reference surface (compare Figure 5.30).
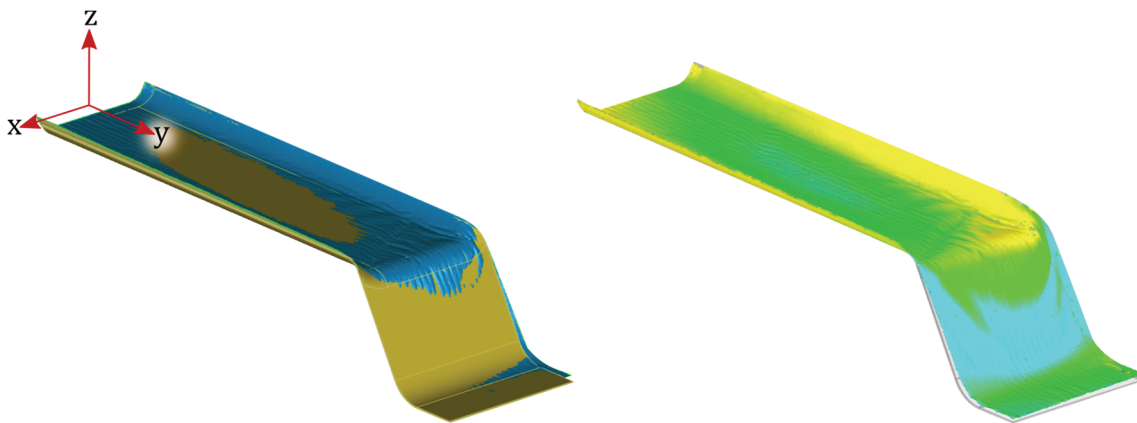
Figure 5.30: Global result of the measuring procedure
left: Comparison of actual (blue) to target (yellow) geometry
right: Deviation of sub-preform as false-color image

5.9.2 Results and Discussion

To compare several results, the measured discrepancy is shown locally at cross-sections along and perpendicular to the sub-preforms long side, according to Figure 5.31. The graph to the left represents cross-sections at five different y-coordinates. The graph to the right represents four cross-sections of different x-coordinate.
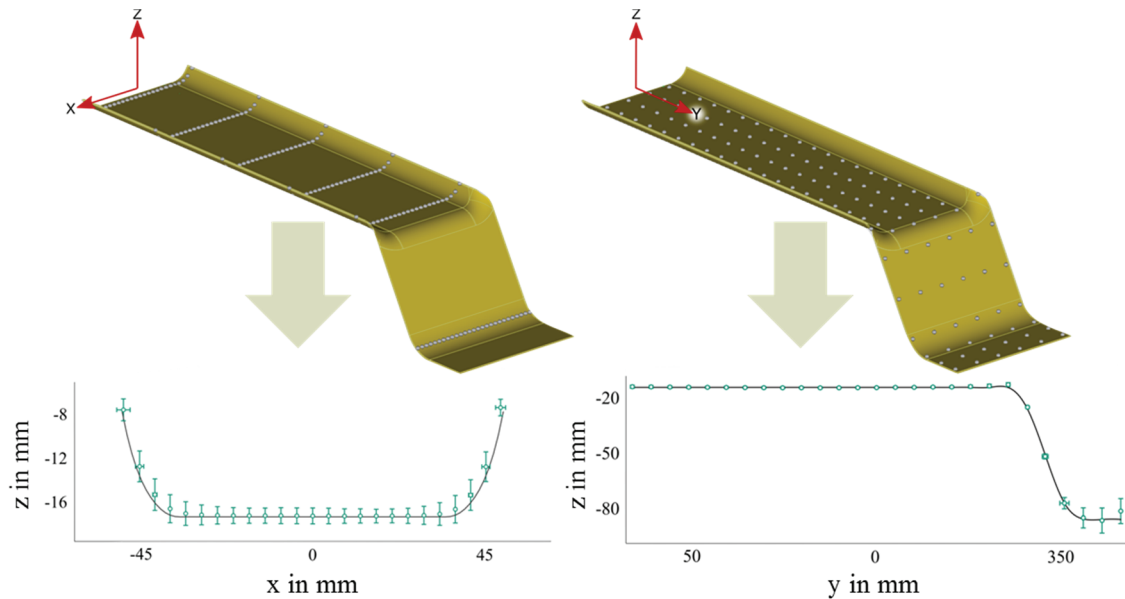
Figure 5.31: Measuring points of the x/z (*left*) and y/z (*right*) cross-sections

The cross-sections in xz-plane are shown in Figure 5.32. Additional to the five different y-coordinates, each graph includes all four layer structures at six iterations. So each point in the graph represents 120 measured points. Manual draping shows an overall mean deviation of 0.22 mm in z-direction and -0.01 mm in x-direction. For stamp draping these values are 0.19 mm for z and 0.02 mm for x. Magnetic draping leads to a deviation of 0.76 mm in z-direction and -0.04 mm in x-direction. The deviation is highest for magnetic draping and lowest for stamp draping.
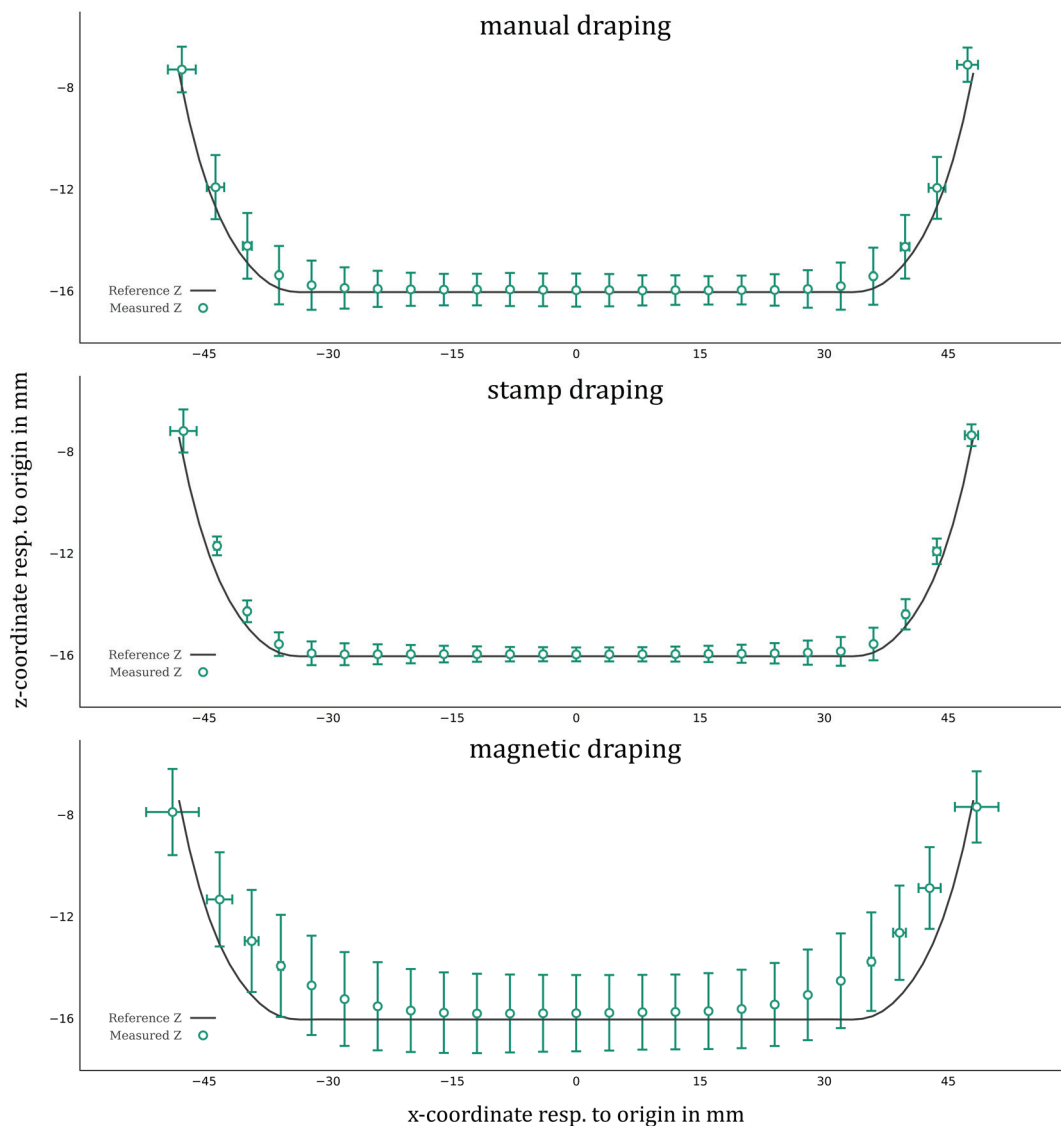
Figure 5.32: X/z cross-sections for all layer structures by draping concepts

Figure 5.33 shows the cross-section along the patches in yz-plane. Manual draping reaches the reference geometry with a deviation of 0.27 mm in z-direction and 0.01 mm in y-direction. A mean deviation of 0.77 mm in z and -0.35 mm in y is achieved by stamp draping. Magnetic draping leads to 1.3 mm for z and 0.62 mm for y. The standard deviation for stamp and manual draping are comparable. Magnetic draping shows higher standard deviation.
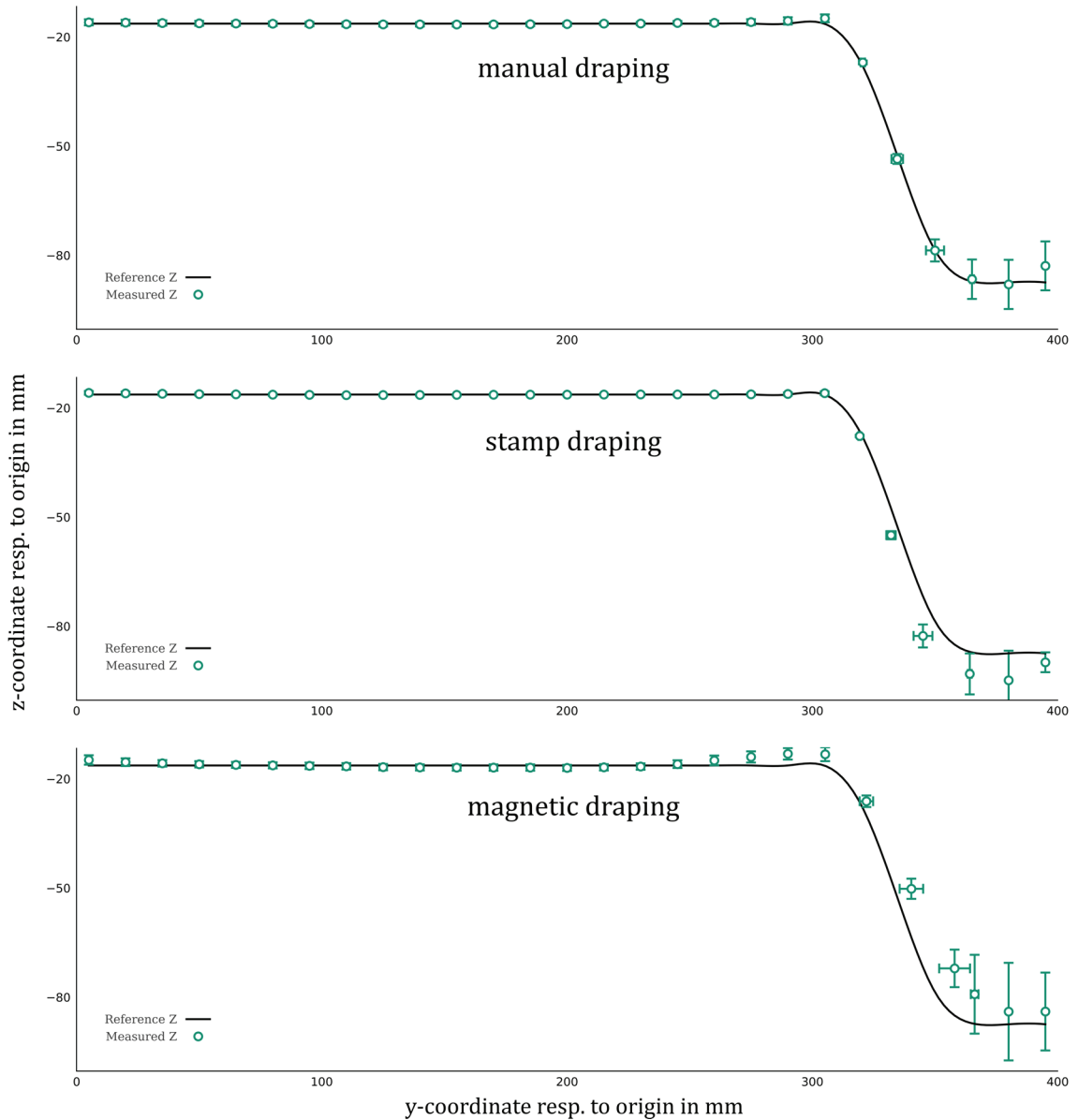
Figure 5.33: Y/z cross-sections for all layer structures by draping concepts

The magnetic draping device is not able to drape sharp radii accurately, but flat sections are draped precisely. Stamp and manual draping are showing very high accuracy in general. The reproducibility of the stamp draping device is superior to the other concepts.

While draping, it became apparent, that the process window for draping after impregnation is limited to around four hours for the used formulation. Afterwards, the first reaction has progressed too far and the material behaves elastic. Thus, spring-back after draping occurs.

5.10 Co-molding to Realize Complex Parts

The hypothesis, that the fundamental requirement for a reliable co-molding is a stiff reinforcement as well as a fixation, was proven in sub-section 5.5 for a magnetic fixation at a two-dimensional problem. In this section the hypothesis is tested for a complex and highly ribbed part – the automotive subfloor. As the reinforcement of this part is a complex three-dimensional structure by itself (see Figure 5.34, left), the fixation concept is simple positive-locking of the structure to the mold. The reinforcement is further supported by the contact of its front faces to the flash face of the mold (see Figure 5.34, right). This is in contrast to the unsupported CoFRTS patch used locally at the two-dimensional trials. Displacement and deformation of the co-molded CoFRTS shall be investigated by representative cross-sections.
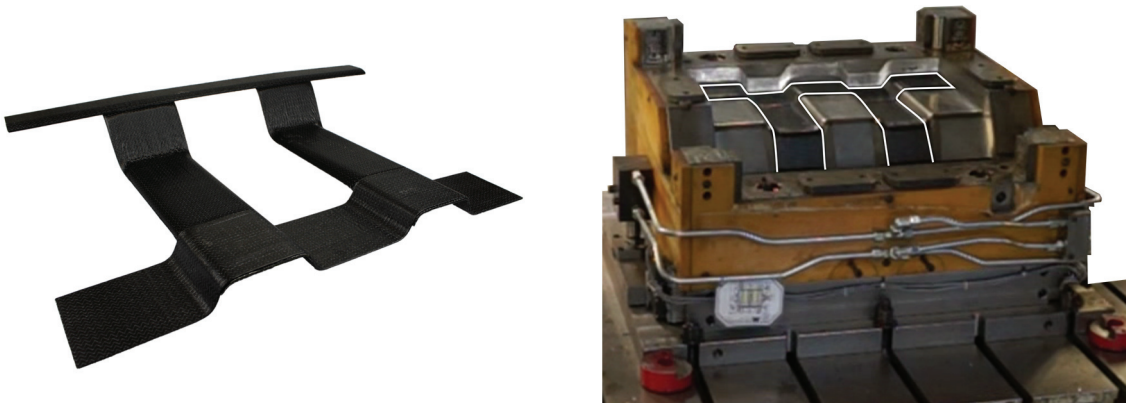
Figure 5.34: CoFRTS to mold complex parts
             left: CoFRTS reinforcement structure
             right: CoFRTS in mold cavity

5.10.1   Methodology

Materials and parts manufactured in the framework of the *MAI qfast* project [18] act as reference and state-of-the-art for this investigation. The semi-finished products for these reference materials were produced by *Polynt*. Hereby, the matrix of CoFRTS (type *HUP CF LE 24760 UDB-1090*) and DicoFRTS (type *HUP CF 24/40 RB 1090/EJ 39935*) is identical and based on a VE resin system. Furthermore, the used car-

bon fiber is the same for CoFRTS and DicoFRTS (*Panex35* (*PX3505098T-13)* by *Zoltek*). Hereby, the CoFRTS is produced directly out of fibers, not from fabric. These reference parts are compared with three populations of parts, which are reinforced by UPPH resin impregnated NCF material (*UD300* by *Zoltek*). The comparing parts are distinguishable by the co-molding material, only. An overview about the differences of all populations is shown in Table 5.3. Detailed information of the comparison parts formulation is given in Table 8.8 (annex on page 146). Except of the reference materials, all semi-finished materials were produced at *Fraunhofer ICT*.

Table 5.3:   **Differences in materials of the examined parts**

	Reference	**Population 2**	**Population 3**	**Population 4**
DicoFRTS				
fiber	Panex35	Panex35	Panex35	Multistar272
fiber form	roving	roving	roving	roving
matrix	VE	VE	UPPH	UPPH
CoFRTS				
fiber	Panex35	Panex35	Panex35	Panex35
fiber form	roving	NCF	NCF	NCF
matrix	VE	UPPH	UPPH	UPPH

After maturation, if necessary, the CoFRTS material is CNC-cut and manually stacked. The CoFRTS total weight is ≈ 858 g and identical for all parts. Hereby, the layup is $(0_2/90/0_2)$ for the reference material and $(0_3/90_2/0_3)$ for the UPPH-material, because of different surface weight of the semi-finished materials. After stacking, the still two-dimensional layups of CoFRTS are preformed manually to three-dimensional reinforcements (as described in section 4.2 on page 70), ready for co-molding.

For the DicoFRTS material there is a different procedure for the reference material than for the comparison materials. For the comparison materials (populations 2-4) the semi-finished DicoFRTS is cut by hand to rectangular sheets of ≈ 90 % of mold coverage and placed on top of

the CoFRTS in the open mold just before co-molding (see Figure 5.35, left). Doing so for the reference material led to massive deformation and displacement of the CoFRTS during co-molding. Thus, the flow of material has to be reduced to a minimum. Therefore, the DicoFRTS for these parts was CNC-cut to six individual blanks and implemented in the draping process for the CoFRTS material. Furthermore the mold coverage of DicoFRTS is raised to 99 %, and the layup of the blank is stepped following the thickness of the final part (see Figure 5.35, right). The DicoFRTS total weight is ≈ 850 g for all produced parts. Details about molding conditions can be found inside the MAI qfast final report [18].
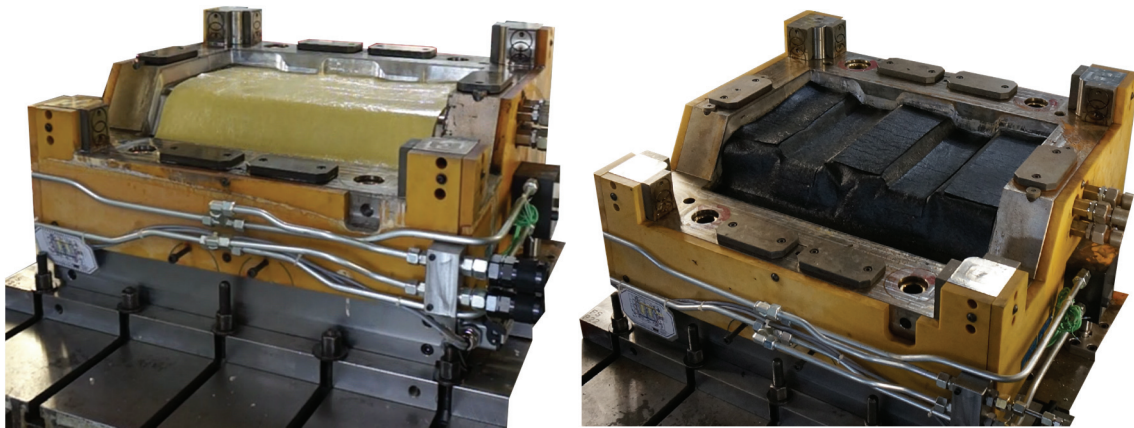
Figure 5.35: **Differences of DicoFRTS before co-molding**
left: Simple rectangular blank for comparison parts
at 90 % mold coverage
right: Complex preform for reference parts
at 99 % mold coverage

After demolding, displacement and deformation of the CoFRTS reinforcing the subfloors cross beam are evaluated. Position and form of the first layer of CoFRTS can be examined on the basis of top views of the parts. Figure 5.36 displays one exemplary part of population 4. So the DicoFRTS is glass fiber reinforced and has high contrast to the CoFRTS. The CoFRTS shows no displacement and low deformation. The quality evaluated by top view is comparable for all populations including the reference population after adjusting the DicoFRTS layup as described above. To gain information about the CoFRTS constitution

inside the part, cross-section micrographs according to Figure 5.36 are prepared.
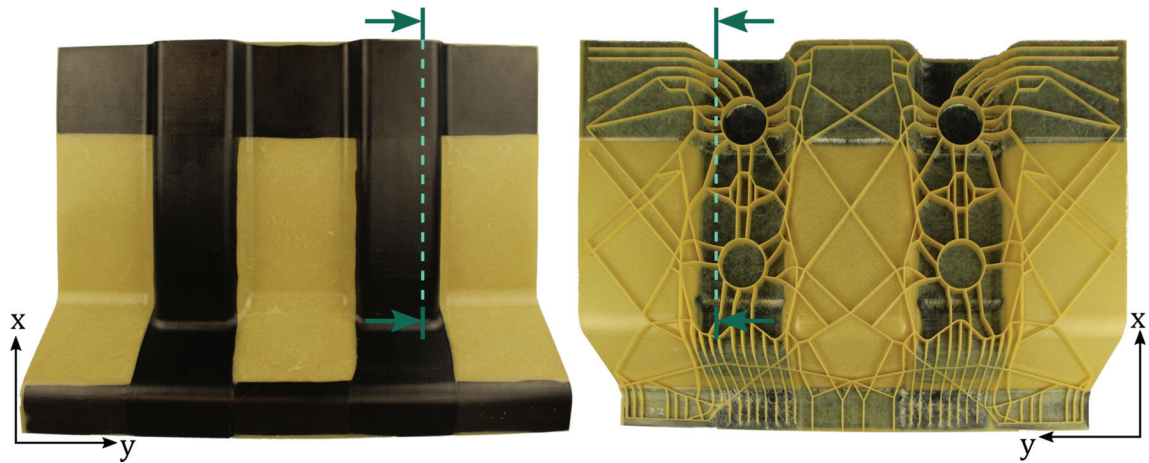
Figure 5.36: Subfloor of population 4 illustrating position of cross-section
left: Top view
right: Bottom view

5.10.2   Results and Discussion

One exemplary cross-section of each population is shown in Figure 5.37. On the left side, the entire cross beams are displayed. The right side shows details about the fiber constitution at the position of ribs.
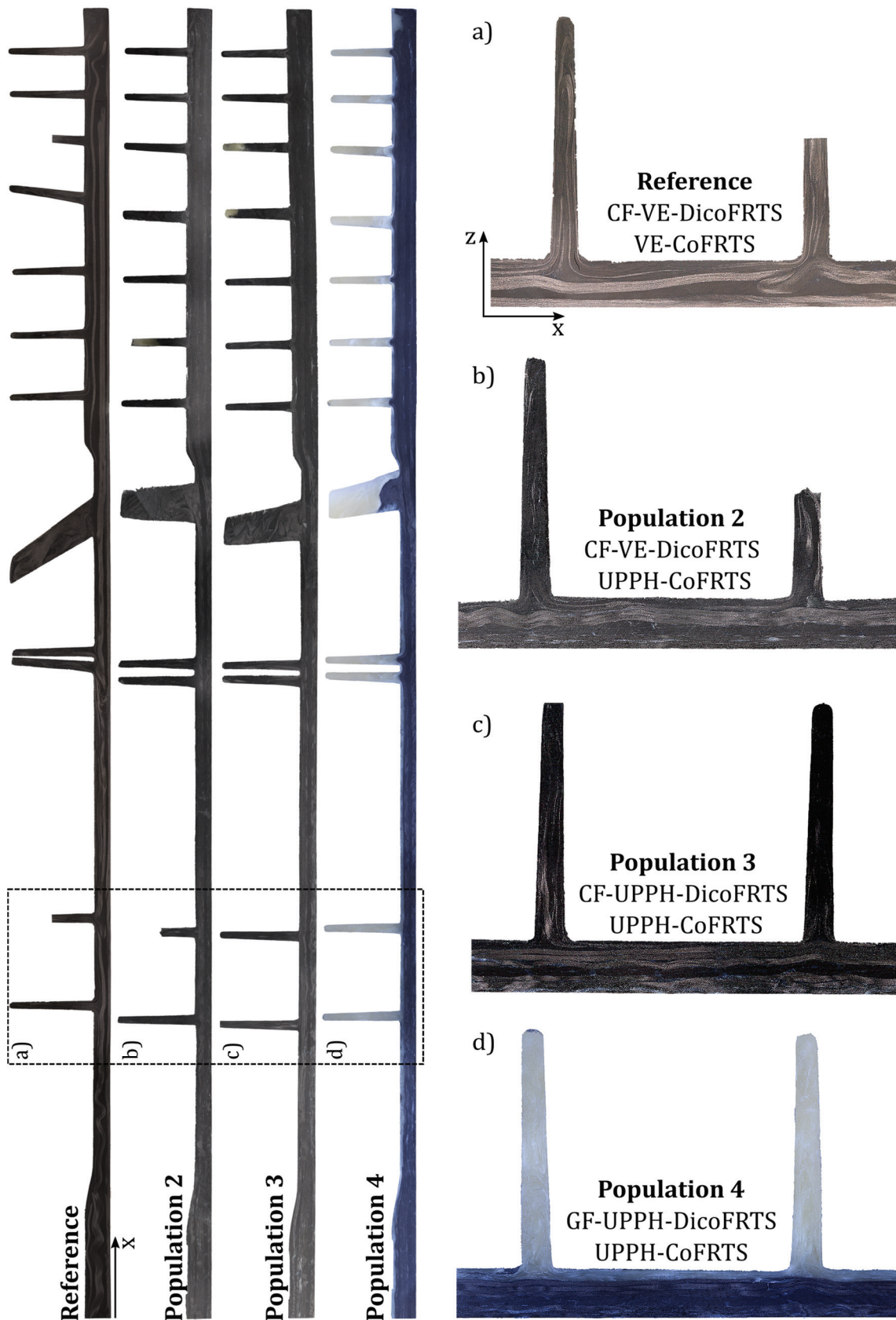
Figure 5.37: Comparison of sub floor cross-sections of different materials

Considering the entire cross beam, the continuous-fibers of the comparing parts are significantly more straight than the reference. Continuous-fibers of the reference parts are misaligned especially in the area of ribs and abrupt changes of wall thickness. This misalignment also affects the fringe of the part: the curviness of the continuous-fibers is shortening the reinforcement's length in x-direction. Thus, there is an unreinforced section at the very end of the cross-section for the reference parts.

At the position of ribs, small to no deformation is visible for UPPH-based CoFRTS. This is independent of the co-molding material (Figure 5.37, b-d). For VE-based CoFRTS there is high deformation of the 0 ° layers next to the rib, whereas the 0 ° layers at the surface remain in position (Figure 5.37, a). Here the 90 ° layer in between compensates the deformation.

Besides the greater resistance of the UPPH-based reinforcements to displacement and deformation, the handleability of the material is improved. The first advantage is based on the low viscosity drop during co-molding, the second on the high viscosity level at B-stage. The resin system even enables a certain amount of flow of the DicoFRTS material and simple cutting patterns without the need of draping of the DicoFRTS or additional fixation of the CoFRTS. This is beneficial for the productivity and a clear economic advantage compared with state-of-the-art materials.

Therefore, it can be concluded, that positive locking is an effective fixation concept for parts of high complexity. This statement is limited to reinforcements providing certain stiffness during co-molding, like the UPPH resin system. For MgO-thickened materials, co-molding is only possible by a consequent reduction of flow, whereby there are still issues with fiber misalignment, at least for the case considered here.

6 Summary

Performance, process reliability, and the economic efficiency of the final component determine whether or not the concept of co-molding presented here will establish itself on the market. The issue of performance and economic efficiency was investigated by the project *MAI qfast*. Even co-molded components of poor CoFRTS fiber alignment are mechanically directly comparable to components made by resin transfer molding [18]. Furthermore the substitution of carbon fibers by glass fibers for less stressed areas of the part, using DicoFRTS, enables for a dramatic reduction of material costs with hardly any loss of the overall stiffness [18]. Component performance and process reliability are determined by draping step and two failure mechanisms during co-molding: deformation and displacement.

- **Draping:** Within this thesis, three draping concepts were investigated: manual draping, stamp draping and magnetic draping. It is obvious, that every draping method has its strengths and weaknesses and is thus appropriate for different draping tasks. At low invest for the negative mold and positive mold realizable by a component itself, manual draping is ideal for small-series production providing sufficient accuracy. High invest is needed to implement stamp draping in the production process. In turn, a fully automated manufacturing line of high accuracy can be achieved and a reliable large-series production of co-molded components becomes possible. Magnetic draping is still on prototype level. It has the benefit of textile friendly draping preventing wrinkles without the need of an upper mold. However, the achievable deformation is limited. Thus, it is best suited for very local reinforcements of simple geometry. Furthermore the mandatory ferromagnetic or ferrimagnetic particles can be used as fixation during co-molding.
All draping concepts have one thing in common: the stability of the preform is drastically increased, when using a hybrid resin. Furthermore the two completely separable chemical reactions of the

UPPH resin allow reliable draping without any risk of starting the radical polymerization. This results in a strong cohesion between reinforcement and the co-molding material by chemical bonding.

- **Deformation of CoFRTS during co-molding:** The straight alignment of the fibers of the reinforcement in the component is key parameter for high and reliable mechanical performance. The application of UPPH resin as CoFRTS matrix material showed great impact on fiber stability during co-molding. That applies for flat reinforcements on plate level as well as for complex reinforcements, especially in the presence of ribs. Also viscosity measurements showed, UPPH resin is a rigid material when B-staged. This simplifies the effort, when it comes to modeling the mold filling process, as the reinforcement can be assumed as stiff inlay.

- **Displacement of CoFRTS during co-molding:** Besides deformation, displacement of the CoFRTS during co-molding is highly critical. Thus, a novel fixation concept for CoFRTS, using magnetic fields, was developed and realized within this thesis. In combination with the high friction coefficient of the UPPH resin, a significant improvement in fixation of very local patches was achieved when compared to conventional material. For more complex shapes of the continuous-fiber reinforcements, even positive-locking was sufficient when combined with the use of the UPPH resin system to keep the fibers in place. However, commercial available mold filling simulation software is not capable of predicting CoFRTS displacement.

To sum up, the research postulates of the introduction were confirmed. The use of modern draping techniques, new resin systems and fixation concepts as described within this thesis significantly improves performance and reliability of CoDicoFRTS components. The material formulations and materials models, but also characterization as well as simulation techniques described here are a major step toward industrialization of this process.

7 Outlook and Suggestions for Further Research

The present work with its holistic character describes materials, methods and processing as detailed as needed to reliably realize parts of CoDicoFRTS in the context of large-series production. For exactly this reason, this work could create the framework for further research addressing the single process steps, advanced resins and functional raw materials as well as improved models and characterization methods, such as:

- Improving process simulation with focus on modelling of the interface between flowing DicoFRTS and mold by thermodynamical friction
- Modelling the rheological and chemomechanical properties of the UPPH-formulation in respect of temporal and thermal history. This could enable a fast adaption of the material to other manufacturing lines without the need for further characterization
- Developing a UPPH-formulation for DicoFRTS providing instant thickening as developed for the CoFRTS material
- Introducing a third reaction step for the CoFRTS to be able to separate impregnation step from draping step
- Characterizing the cohesion between UPPH-based CoFRTS and DicoFRTS after co-molding more deeply
- Investigating the thickening effect of resins containing ferromagnetic or ferrimagnetic particles of different shape in the presence of a magnetic field
- Describing phenomena during co-molding of ripped structures with generic specimens
- Setting up a pilot line for fully automated manufacturing of CoDicoFRTS – from impregnation to structure

Some of these point are addressed by the currently running international research and training group "Integrated engineering of continuous discontinuous long fiber reinforced polymer structures" (GRK 2078, presented within [29]) and will be content of future scientific publications.

8 Appendix

8.1 Temperature Profiles for Viscosity Measurements

Table 8.1:   Temperature profile 1

No.	Start temp. in °C	End temp. in °C	Gradient in °C/min	Duration in min
1.	23	23	0	10
2.	23	80	60	1
3.	80	80	0	20
4.	80	23	-60	1
5.	23	23	0	10
6.	23	150	60	2.1
7.	150	150	0	10
8.	150	23	-30	4.2
9	22	22	0	10

Table 8.2:   Temperature profile 2

No.	Start temp. in °C	End temp. in °C	Gradient in °C/min	Duration in min
1.	22	22	0	10
2.	22	80	60	1
3.	80	80	0	4
4.	80	18	-60	1
5.	18	18	0	10
6.	18	80	60	1
7.	80	80	0	6
8.	80	18	-60	1
9.	18	18	0	600
10.	18	150	60	2.2
11.	150	150	0	10
12.	150	22	-30	4.3
13.	22	22	0	10

8.2 Mechanical Characterization Results

Table 8.3:   Formulation UPPH-CoFRTS

material	supplier	phr	wt.-%	vol.-%
Daron 41	aliancys	100	27.72	37.71
L-powder	UOP	1.5	0.42	0.31
pBQ 10%	Fraunhofer ICT	0.3	0.08	0.26
9085	BYK	2	0.55	0.89
Trigonox 117	AkzoNobel	1	0.28	0.92
Lupranat M20R	BASF	25	6.93	17.33
Borchi Kat 0243	Borchers	0.1	0.02	0.03
Panex UD300	Zoltek	-	64.00	52.23

Table 8.4: Mechanical characterization results UD-materials

		Unit	0° Manufac. 1	0° Manufac. 2	0° UD UPPH	90° Manufac. 1	90° Manufac. 2	90° UD UPPH
tensile testing	based on method		DIN EN ISO 527-5	DIN EN ISO 527-5	DIN EN ISO 527-5	DIN EN ISO 527-5	DIN EN ISO 527-5	DIN EN ISO 527-5
	sample geometry	mm	l = 250 b = 25 h = 2.5	l = 250 b = 25 h = 2.2	l = 250 b = 15 h = 1	l = 250 b = 25 h = 2.3	l = 250 b = 25 h = 2.3	l = 230 b = 25 h = 1.9
	testing velocity	mm/min	2	2	2	2	2	2
	clamping distance	mm	150	150	150	150	150	150
	measurement length	mm	100	100	100	100	100	100
	cap strips	mm	none	none	50	none	none	50
	tested specimen	-	>5	7	6	8	6	4
	tensile strength	MPa	1131 ± 89.7	1390.6 ± 45.7	1723.7 ± 174	19.6 ± 1.6	14 ± 1.2	36.2 ± 8.6
	Young's modulus	GPa	105.8 ± 1.7	104.2 ± 3.4	113.8 ± 6.8	5.6 ± 1.4	6.3 ± 0.4	8.3 ± 0.2
	strain at break	%	1.02 ± 0.08	1.39 ± 0.24	1.4 ± 0.1	0.33 ± 0.06	0.22 ± 0.04	0.39 ± 0.1
compression testing	based on method		DIN EN ISO 14126	DIN EN ISO 14126	DIN EN ISO 14126	DIN EN ISO 14126	DIN EN ISO 14126	DIN EN ISO 14126
	sample geometry	mm	l = 110 b = 10 h = 2.3	l = 110 b = 10 h = 2.3	l = 110 b = 10 h = 1.9	l = 110 b = 10 h = 2.3	l = 110 b = 10 h = 2.3	l = 110 b = 10 h = 1.9
	testing velocity	mm/min	1	1	1	1	1	1
	clamping distance	mm	12	12	12	12	12	12
	measurement length	mm	10	10	10	10	10	10
	tested specimen	-	8	5	11	9	5	7
	compressive strength	MPa	446.3 ± 15.4	560 ± 17.4	590 ± 32,1	93 ± 3.3	84.9 ± 6.4	171.2 ± 5.8
	modulus of elasticity in comp.	GPa	103 ± 3.6	94.4 ± 2	104.7 ± 7	5.7 ± 0.2	6.3 ± 0.1	7.8 ± 0.6
	compressive failure strain	%	0.43 ± 0.03	0.62 ± 0.02	0.63 ± 0.1	2.94 ± 0.34	1.5 ± 0.16	3.22 ± 0.5
3 point - bending testing	based on method		DIN EN ISO 14125	DIN EN ISO 14125	DIN EN ISO 14125	DIN EN ISO 14125	DIN EN ISO 14125	DIN EN ISO 14125
	sample geometry	mm	l = 50 * h b = 15 h = 2.3	l = 50 * h b = 15 h = 2.3	l = 50 *h b = 15 h = 2.1	l = 50 * h b = 15 h = 2.3	l = 50 * h b = 15 h = 2.4	l = 30 * h b = 15 h = 2.1
	testing velocity	mm/min	6	6	6	6	6	6
	distance between supports	mm	90	92	L = 40 * h	91	94	L = 40 * h
	tested specimen	-	5	6	6	4	6	6
	flexural strength	MPa	1140 ± 69.9	1263.9 ± 15.4	1475.8 ± 97.4	40.7 ± 2.4	29.4 ± 1.2	67.64 ± 4
	flexural modulus	GPa	101.1 ± 1.9	89 ± 3.8	105.7 ± 2.2	5.4 ± 0.06	5.6 ± 0.2	7.9 ± 1
	deflection at flexural strength	%	1.14 ± 0.07	1.48 ± 0.1	1.5 ± 0.15	0.77 ± 0.05	0.52 ± 0.02	0.84 ± 0.1
Charpy	based on method		DIN EN ISO 179-1	DIN EN ISO 179-1	DIN EN ISO 179-1	DIN EN ISO 179-1	DIN EN ISO 179-1	DIN EN ISO 179-1
	sample geometry	mm	l = 25 * h b = 15 h = 2.3	l = 25 * h b = 15 h = 2.4	l = 25 * h b = 15 h = 1.9	l = 25 * h b = 15 h = 2.3	l = 25 * h b = 15 h = 2.4	l = 25 * h b = 15 h = 1.9
	impact velocity	m/s	2.9	2.9	2.9	2.9	2.9	2.9
	distance between supports	mm	20 * h	20 * h	20 * h	20 * h	20 * h	20 * h
	impact energy	J	5	5	5	1	1	1
	tested specimen	-	9	11	10	9	11	10
	Charpy impact strength	kJ/m^2	75.3 ± 6.1	80.7 ± 8.5	77 ± 6.1	3.3 ± 1	3.6 ± 1	7.5 ± 1.3

8.3 Magnetic Characterization Details

Table 8.5: **Specimen details for magnetic characterization**

φ in vol. $-\%$	Initial plate No.	Sample No.	Fiber content in wt. $-\%$
8.7	Mag_5_1	5_1	48
5.6	Mag_4_2	4_2	52
3.1	Mag_3_2	3_2_2	52
0	Mag_2_2	2_2_1	56

8.4 Deformation and Displacement Molding Trials

Table 8.6: CoFRTS formulations used for co-molding

material 1	supplier	phr	wt.-%	vol.-%
Palapreg Premium G22-01LE	aliancys	100	28.48	40.54
Millicarb	Omya	66	19.03	11.10
Palapreg Premium G21-01LE Cure	aliancys	1	0.29	0.49
Styrene	BASF	27	1.73	2.99
W9010	BYK	2.2	0.63	0.86
Ceaesit 1	Baerlocher	6.5	1.87	3.04
Luvatol MK35	L&V	2.1	0.61	0.58
Panex UD300	Zoltek	-	47.00	40.40
material 2	**supplier**	**phr**	**wt.-%**	**vol.-%**
Palapreg Premium G22-01LE	aliancys	100	20.99	33.32
Bayferrox 318m	LANXESS	66.5	13.96	5.40
Millicarb	Omya	73	15.32	10.09
Palapreg Premium G21-01LE Cure	aliancys	1	0.21	0.40
Styrene	BASF	27	3.80	5.97
W9010	BYK	2.2	0.46	0.71
Ceaesit 1	Baerlocher	6.5	1.36	2.50
Luvatol MK35	L&V	2.1	0.44	0.47
Panex UD300	Zoltek	-	46.00	44.65
material 3	**supplier**	**phr**	**wt.-%**	**vol.-%**
Daron 41	aliancys	100	29.67	42.56
Incozol 2	Incorez	1	0.30	0.51
Millicarb	Omya	73	21.66	12.43
Peroxan	Pergan	1.2	0.36	0.59
Lupranat M20R	BASF	27	8.01	10.09
Panex UD300	Zoltek	-	40.00	33.82
material 4	**supplier**	**phr**	**wt.-%**	**vol.-%**
Daron 41	aliancys	100	14.09	25.17
Incozol 2	Incorez	1	0.14	0.30
Bayferrox 318m	LANXESS	139	19.59	8.21
Millicarb	Omya	115	16.21	11.58
Peroxan	Pergan	1.2	0.17	0.35
Lupranat M20R	BASF	27	3.80	5.97
Panex UD300	Zoltek	-	46.00	48.43

8.5 Mold Filling Simulation Models and Material Parameters

8.5.1 Viscosity

Model:

$$\eta = \frac{\eta_0}{1 + \left(\frac{\eta_0 \dot{\gamma}}{\tau^*}\right)^{1-n}}$$

$$\eta_0 = S \exp\left(\frac{T_\mathrm{S}}{T}\right)$$

Material parameters:

$$\tau^* = 1 \text{ Pa}$$
$$n = 0.3$$
$$S = 1.556 \ 10^9 \text{ Pa s}$$
$$T_\mathrm{S} = 1661.21 \text{ K}$$

8.5.2 Thermal Properties

Heat capacity:

$$c_\mathrm{p} = 0.472197 \text{ J/(kg K)}$$

Thermal conductivity:

$$\lambda = 0.7 \text{ W/(m K)}$$

8.6 Draping

Table 8.7:   CoFRTS formulation used for draping

manual draping

stamp draping	supplier	phr	wt.-%	vol.-%
Daron 41	aliancys	100	29.78	39.82
9076	BYK	3	0.89	1.23
9085	BYK	2	0.60	0.93
Styrene	BASF	2.9	0.85	1.33
pBQ 10%	Fraunhofer ICT	0.3	0.09	0.13
Trigonox 117	AkzoNobel	1	0.30	0.46
Lupranat M20R	BASF	25	7.44	8.74
Borchi Kat 0243	Borchers	0.15	0.04	0.06
Panex UD300	Zoltek	-	60.00	47.29
magnetic draping	**supplier**	**phr**	**wt.-%**	**vol.-%**
Daron 41	aliancys	100	20.56	33.38
9076	BYK	3	0.62	1.03
9085	BYK	2	0.41	0.78
Styrene	BASF	2.1	0.43	0.81
Bayferrox 318m	Lanxess	112.5	23.13	8.82
pBQ 10%	Fraunhofer ICT	0.3	0.06	0.11
Trigonox 117	AkzoNobel	1	0.21	0.39
Lupranat M20R	BASF	25	5.14	7.33
Borchi Kat 0243	Borchers	0.15	0.03	0.05
Panex UD300	Zoltek	-	49.41	49.29

8.7 Co-molding of Complex Parts

Table 8.8: Formulations used for co-molding of subfloor structures

CoFRTS of population 2, 3, 4	supplier	phr	wt.-%	vol.-%
Daron 41	aliancys	100	29.78	39.82
9076	BYK	3	0.89	1.23
9085	BYK	2	0.60	0.93
Styrene	BASF	2.9	0.85	1.33
pBQ 10%	Fraunhofer ICT	0.3	0.09	0.13
Trigonox 117	AkzoNobel	1	0.30	0.46
Lupranat M20R	BASF	25	7.44	8.74
Borchi Kat 0243	Borchers	0.15	0.04	0.06
Panex UD300	Zoltek	-	60.00	47.29

DicoFRTS of population 2	supplier	phr	wt.-%	vol.-%
Atlac XP810X	aliancys	100	54.55	65.38
9085	BYK	2	1.09	1.56
Trigonox 117	AkzoNobel	1	0.55	0.77
Luvatol EK100KM	L&V	7	3.82	3.15
PX3505098T-13	Zoltek	-	40.00	29.14

DicoFRTS of population 3	supplier	phr	wt.-%	vol.-%
Daron ZW 14142	aliancys	100	45.28	56.01
L-Powder	UOP	5	2.26	1.47
9085	BYK	2	0.91	1.28
pBQ 10%	Fraunhofer ICT	0.3	0.14	0.18
Trigonox 117	AkzoNobel	1	0.45	0.63
Lupranat M20R	BASF	24.2	10.96	11.57
PX3505098T-13	Zoltek	-	40.00	28.86

DicoFRTS of population 4	supplier	phr	wt.-%	vol.-%
Daron ZW 14141	aliancys	100	43.04	60.52
L-Powder	UOP	5	2.15	1.59
9085	BYK	2	0.86	1.38
pBQ 10%	Fraunhofer ICT	0.3	0.13	0.19
Trigonox 117	AkzoNobel	1	0.43	0.68
Lupranat M20R	BASF	19.5	8.39	10.07
Multistar 272	Johns Manville	-	45.00	25.56

9 List of Figures

10   List of Tables

11 Curriculum Vitae

Personal Details

Name: David Bücheler

Email: DavidBuecheler@gmail.com

Professional Experience

09/2016 – to date   Group Manager Thermoset Processing at
                         Fraunhofer Institute for Chemical Technology

04/2015 – 12/2016   Research assistant at
                         Institute for Vehicle System Technology (FAST)
                         Karlsruhe Institute of Technology (KIT)

05/2012 – 09/2016   Research assistant at
                         Fraunhofer Institute for Chemical Technology

11/2007 – 03/2010   Graduate assistant at
                         Institute of Technical Mechanics (ITM)
                         Karlsruhe Institute of Technology (KIT)

Education

10/2006 – 04/2012   Student at
                         Department of Mechanical Engineering
                         Karlsruhe Institute of Technology (KIT)
                         Special field: Development and Research

09/2002 – 06/2005   Pupil at
                         Technisches Gymnasium Sigmaringen

09/1996 – 07/2002   Pupil at
                         Martin-Heidegger-Gymnasium Messkirch

12 References

[1]   J. Fraden, *Handbook of modern sensors: Physics, designs, and applications*. New York: Springer Verlag, 2010.

[2]   European Alliance for SMC/BMC, *Sustainability aspects of SMC/BMC based products.* [Online] Available: http://www.allbro.com/wordpress/wp-content/uploads/ 2015/09/Position-paper-from-the-European-Alliance-for-SMC-and-BMC.pdf. Accessed on: Jul. 12 2016.

[3]   A. Wilson, "Vehicle weight is the key driver for automotive composites," *Reinforced Plastics*, vol. 61, no. 2, pp. 100–102, 2017.

[4]   European Union, *Reducing CO2 emissions from passenger cars.* [Online] Available: http://ec.europa.eu/clima/policies/ transport/vehicles/cars/index_en.htm.
        Accessed on: May 26 2017.

[5]   G. Schuh, K. Korthals, and J. Arnoscht, "Contribution of Body Lightweight Design to the Environmental Impact of Electric Vehicles," *AMR*, vol. 907, pp. 329–347, 2014.

[6]   K. Gebhardt, V. Schau, and W. R. Rossak, "Applying stochastic methods for range prediction in E-mobility," in *2015 15th International Conference on Innovations for Community Services (I4CS)*, Nuremberg, Germany, pp. 1–4.

[7]   V. Schau, W. Rossak, H. Hempel, and S. Spathe, "Smart City Logistik Erfurt (SCL): ICT-support for managing fully electric vehicles in the domain of inner city freight traffic," in *2015 International Conference on Industrial Engineering and Operations Management (IEOM)*, Dubai, pp. 1–8.

[8]   W. Assmann and E. Witten, *Handbuch Faserverbundkunststoffe - Composites: Grundlagen, Verarbeitung, Anwendungen,* 4th ed. Wiesbaden: Springer Fachmedien, 2013.

[9]   G. W. Ehrenstein, *Faserverbund-Kunststoffe: Werkstoffe, Verarbeitung, Eigenschaften,* 2nd ed. München [u.a.]: Hanser, 2006.

[10] P. Elsner, P. Eyerer, and T. Hirth, *Kunststoffe: Eigenschaften und Anwendungen,* 8th ed. Dordrecht: Springer, 2011.

[11] F. Henning and E. Moeller, *Handbuch Leichtbau: Methoden, Werkstoffe, Fertigung*. München: Hanser, 2011.

[12] M. Biron, *Thermosets and composites: Material selection, applications, manufacturing, and cost analysis,* 2nd ed. Oxford [u.a.]: Andrew, Elsevier, 2014.

[13] M. M. Schwartz, *Encyclopedia of materials, parts, and finishes,* 2nd ed. Boca Raton: CRC Press, 2002.

[14] C. Cherif, *Textile Materials for Lightweight Constructions*. Berlin, Heidelberg: Springer Berlin Heidelberg, 2016.

[15] H. Lengsfeld, *Faserverbundwerkstoffe: Prepregs und ihre Verarbeitung*. München: Hanser, 2015.

[16] D. Bücheler and F. Henning, "Hybrid Resin Improves Position and Alignment of Continuously Reinforced Prepreg During Compression Co-molding With Sheet Molding Compound," in *17th European Conference on Composite Materials (ECCM17)*, München, 2016, pp. 6699–6703.

[17] A. Trauth, D. Bücheler, K. A. Weidenmann, and F. Henning, "Mechanical Properties of Unidirectional Continuous Carbon Fiber Reinforced Sheet Molding Compounds," in *17th European Conference on Composite Materials (ECCM17)*, München, 2016, pp. 6716–6723.

[18] Audi AG, *MAI qfast - Vergleichende Prozess- und Eigenschaftsbewertung für potentielle FVK-Strukturanwendungen in der automobilen Großserie*: [Audi AG], 2015.

[19] K. Akiyama, "Development of PCM technology," in *11th-Annual Automotive Composites Conference and Exhibition, ACCE 2011*, p. 37.

[20] K. Akiyama, "Development of preforming process in PCM (Prepreg Compression Molding) technology," in *12th Annual Automotive Composites Conference and Exhibition 2012 (ACCE 2012) ; Troy, Michigan, USA, 11 - 13 September 2012*, 2013, pp. 347–362.

[21] C. Jansen, "Carbon Fiber Isogrid-Stiffened Automotive Suspension Arm," 2013. [Online] Available: http://gaiusauto.com/oemodm.html. Accessed on: Dec. 30 2014.

[22] M. Bruderick, D. Denton, M. Shinedling, and M. Kiesel, "Aplications of carbon fiber SMC for the Dodge Viper," ACCE, 2002. [Online] Available: http://www.quantumcomposites.com/pdf/papers/Viper-SPE-Paper.pdf. Accessed on: Dec. 30 2014.

[23] J. Wulfsberg *et al.,* "Combination of Carbon Fibre Sheet Moulding Compound and Prepreg Compression Moulding in Aerospace Industry," in *11th International Conference on Technology of Plasticity, ICTP*, pp. 1601–1607.

[24] M. Karcher, *Beitrag zur Umsetzung, Charakterisierung und Evaluierung eines Direktverfahrens zur Herstellung von strukturellen Bauteilkomponenten aus kohlenstofffaserverstärktem Kunststoff (InlinePrepreg)*. Stuttgart: Fraunhofer Verlag, 2016.

[25] W. Pangboonyanon, M. Zaiß, J. Fleischer, and L. Gisela, "Optimization of process chain for continuous-discontinuous long fiber reinforced polymer structures," in *17th European Conference on Composite Materials (ECCM17)*, München, 2016, pp. 6478–6485.

[26] M. Neitzel, P. Mitschang, and U. Breuer, *Handbuch Verbundwerkstoffe: Werkstoffe, Verarbeitung, Anwendung,* 2nd ed. München: Hanser, 2014.

[27] A. B. Strong, *Fundamentals of composites manufacturing: Materials, methods and applications,* 2nd ed. Dearborn, Mich.: Society of Manufacturing Engineers, 2008.

[28] W. Michaeli, *Einführung in die Technologie der Faserverbundwerkstoffe*. München: Hanser, 1990.

[29] L. Kärger, T. Böhlke, K.-A. Weidenmann, and F. Henning, "Integrierte Entwicklung kontinuierlich-diskontinuierlich langfaserverstärkter Polymerstrukturen im Rahmen des internationalen Graduiertenkollegs GRK 2078," Hamburg, Feb. 25 2016.

[30] Industrievereinigung Verstärkte Kunststoffe e. V, *GFK-Markt Europa – Wachstum der Produktionsmenge setzt sich fort.* [Online] Available: http://plasticker.de/Kunststoff_News_26022_ AVK_GFK_Markt_Europa__Wachstum_der_Produktionsmenge_ setzt_sich_fort?nmax=25&kat=Wirtschaftsdaten&nmin=25. Accessed on: Nov. 01 2016.

[31] H. G. Kia, *Sheet molding compounds: Science and technology*. Munich, New York, Cincinnati: Hanser; Hanser/Gardner Publications, 1993.

[32] P. Eyerer, *Polymer engineering: Technologien und Praxis ; mit 155 Tabellen*. Berlin, Heidelberg: Springer, 2008.

[33] I. Vancsó-Szmercsányi, "Interaction Between Unsaturated Polyester Resins and Metal Oxides," *Kunststoffe*, no. 12, pp. 1066–1071, 1970.

[34] C. Keckl, *Einfluss der Eindickung von dichtereduziertem Sheet Moulding Compound auf die Formteilwelligkeit*. Stuttgart: Fraunhofer Verlag, 2016.

[35] K. N. Warner, "Mechanism of the Thickening of Polyester by Alkaline Earth Oxides and Hydroxides," in *Annual Tech Conference Proceedings*, Washington, DC, USA, 1973.

[36] K. S. Gandhi and R. Burns, "Studies on the thickening reaction of polyester resins employed in sheet molding compounds," *J. Polym. Sci. Polym. Chem. Ed.*, vol. 14, no. 4, pp. 793–811, 1976.

[37] I. Vancso-Szmercsanyi, "Investigation of the reactions of condensation polymers and metal oxides," *Polymer Science U.S.S.R.*, vol. 15, no. 2, pp. 432–440, 1973.

[38] E. L. Rodriguez, "On the thickening mechanism of unsaturated polyesters by alkaline earth oxides and hydroxides," *J. Appl. Polym. Sci.*, vol. 40, no. 1112, pp. 1847–1855, 1990.

[39] R. Lorenz and T. Sueck, "Ungesättigte Polyesterharze - Chemische Grundlagen und technischer Stand," in *6. Internationale AVK-TV Tagung*, Baden-Baden, 2003.

[40]   D. Judas, A. Fradet, and E. Marechal, "Thickening of polyester resins with MgO: Structural study of a model magnesium carboxylate," *Polymer Bulletin*, vol. 16, no. 1, pp. 13–17, 1986.

[41]   K. E. Eisemon and J. D. Lewis, "New Proposed Mechanism for the Reaction of Unsaturated Polyester Resins by Alkaline Earth Metal Oxides," in *Composites 2004*, Tampa, Fla., U.S.A., 2004.

[42]   R. Saito, W.-M. J. Kan, and L. James Lee, "Thickening behaviour and shrinkage control of low profile unsaturated polyester resins," *Polymer*, vol. 37, no. 16, pp. 3567–3576, 1996.

[43]   K. A. Iseler, P. K. Guha, and R. C. Yen, "Dual functional additive," US 4535110 A.

[44]   J. Ferrarini, D. M. Longenecker, N. N. Shah, J. Feltzin, and G. G. Greth, "Unique Process for Thickening Smc With Polyurethane," *Modern Plastics*, no. 55, pp. 66–68, 1978.

[45]   H. R. Edwards, "High Performance Urethane Modified Unsaturated Polyesters," in *14th Reinforced Plastics Congress*, Brighton, England, 1984.

[46]   H. R. Edwards, "Handling and Physical Properties of Hybrid Polyesters," in *Technical Sessions of the 39th Annual Conference*, New York, NY, USA, 1984.

[47]   H. R. Edwards, "Use of Isophthalic Unsaturated Polyester Urethane Hybrids in Conventional Molding Techniques," in *ANTEC 86*, Boston, MA, USA, 1986, pp. 1326–1330.

[48]   H. R. Edwards, "Polyester/Urethane Hybrids Are Suited for Conventional Molding," *Modern Plastics*, no. 64, pp. 66–74, 1987.

[49]   D. G. Vanderlaan, "Low shrink hybrid resins," US 4822849 A.

[50]   G. A. van den Hondel, "Daron light weight composites," in *UTECH 96: Book of papers*, D. J. Reed and C. Lee, Eds., London, UK: Crain Communications Ltd, 1996, Paper 15, p1-4.

[51]   Y. Hayakawa, T. Shibata, K. Akiyama, and K. Nishino, "Isocyanate-modified toughened SMC and its properties," *International Progress in Urethanes*, no. 6, pp. 146–162, 1993.

[52]   Y.-Y. Chiu, R. Saito, and L. James Lee, "Modification of unsaturated polyester resins for viscosity control," *Polymer*, vol. 37, no. 11, pp. 2179–2190, 1996.

[53]   A. B. Cherian, B. T. Abraham, and E. T. Thachil, "Modification of unsaturated polyester resin by polyurethane prepolymers," *J. Appl. Polym. Sci.*, vol. 100, no. 1, pp. 449–456, 2006.

[54]   J. W. Putnam, B. S. Hayes, and J. C. Seferis, "Prepreg process-structure-property analoysis and scale-up for manufacturing and performance," *Journal of advanced materials*, no. 27, pp. 47–57, 1996.

[55]   F. C. Campbell, *Structural composite materials*. Materials Park, Ohio: ASM International, 2010.

[56]   G. Savage, *Carbon-Carbon Composites*. Dordrecht: Springer Netherlands; Imprint; Springer, 1993.

[57]   J. Prockat, *Developing large structural parts for railway application using a fibre reinforced polymer design*. Berlin: Univ.-Verl. der TU, 2005.

[58]   S. K. Mazumdar, *Composites manufacturing: Materials, product and process engineering*. Boca Raton: CRC Press, 2002.

[59]   M. Shirinbayan *et al.,* "Multi-scale experimental investigation of the viscous nature of damage in Advanced Sheet Molding Compound (A-SMC) submitted to high strain rates," *Composites Part B: Engineering*, vol. 115, pp. 3–13, 2017.

[60]   D. M. Corbridge, L. T. Harper, D. S. A. De Focatiis, and N. A. Warrior, "Compression moulding of composites with hybrid fibre architectures," *Composites Part A: Applied Science and Manufacturing*, vol. 2017, no. 95, pp. 87–99.

[61]   P. K. Mallick, *Fiber-reinforced composites: Materials, manufacturing, and design,* 3rd ed. Boca Raton: CRC/Taylor & Francis, 2007.

[62]   A. C. Long, *Composites forming technologies*. Cambridge: Woodhead, 2007.

[63] S. V. Lomov, *Non-crimp fabric composites: Manufacturing, properties and applications*. Oxford, Philadelphia: Woodhead Pub, 2011.

[64] BMW AG, *Automated tool based draping of i3 roof.* [Online] Available: https://www.press.bmwgroup.com/ deutschland/photo/compilation/T0178337DE/die-bmw-i8-produktion. Accessed on: Dec. 18 2016.

[65] BMW AG, *Rigid tool based draped roof of the BMW M3.* [Online] Available: https://www.press.bmwgroup.com/ deutschland/photo/detail/P90149583/die-bmw-m3-limousine-mit-carbon-dach-05/2014. Accessed on: Dec. 18 2016.

[66] T. Fürst, F. Henning, B. Thoma, L. Kärger, and F. Schirmaier, "Cost-efficient Preforming as leading process step to achieve a holistic and profitable RTM product development," Stuttgart, Sep. 21 2015.

[67] grz, *Senkung der Gewichtsspirale.* [Online] Available: http://www.k-zeitung.de/senkung-der-gewichtsspirale/ 150/1200/86204/1. Accessed on: Dec. 20 2016.

[68] D. Gay, *Composite materials: Design and applications*. Boca Raton: CRC Press, Taylor & Francis, 2015.

[69] K. Henning, Ed., *Wirtschaftliche Herstellung von Faserverbundbauteilen mit Hilfe automatisiert hergestellter textiler Preforms*. Aachen: Shaker, 2008.

[70] C. A. Ehinger, *Automatisierte Montage von Faserverbund-Vorformlingen*. München: Utz, 2013.

[71] M. T. Kordi, *Entwicklung von Roboter-Endeffektoren zur automatisierten Herstellung textiler Preforms für Faserverbundbauteile*. Aachen: Shaker, 2009.

[72] C. D. Rudd, *Composites for automotive applications*. [Shawbury, Shropshire]: Rapra Technology Ltd, 2001.

[73] P. Egger and A. Stock, "Automated Production of Fiber Composite Components: New Horizons for Lightweight Construction," in *Kunststoffe international*.

[74] B. Hangs *et al.,* "Co-compression molding of tailored continuous-fiber-inserts and inline-compounded long-fiber-thermoplastics," in *12th Annual Automotive Composites Conference and Exhibition 2012 (ACCE 2012) ; Troy, Michigan, USA, 11 - 13 September 2012*, 2013, pp. 481–499.

[75] T. Huber, *Einfluss lokaler Endlosfaserverstärkungen auf das Eigenschaftsprofil struktureller Spritzgießbauteile*. Stuttgart: Fraunhofer-Verl., 2014.

[76] B. Hangs, D. Bücheler, M. Karcher, and F. Henning, "High-volume production of structural automobile parts: Comparative study of relevant composite technologies," in *FIPCO Functional Integrated Plastic Components 2016*.

[77] P. K. Mallick, "Effect of fiber misorientation on the tensile strength of compression molded continuous fiber composites," *Polym. Compos.*, vol. 7, no. 1, pp. 14–18, 1986.

[78] F. Gortner, "Advanced SMC-processing with continuous fiber reinforcement," in *20th International Conference on Composite Materials*, Copenhagen, 2015.

[79] J. W. Kim, "Study on Compression Molding of an Intercrossed Prepreg Glass Fiber-Reinforced Plastic," *Strength Mater*, vol. 48, no. 1, pp. 113–120, 2016.

[80] J. Chen *et al.,* "Measurement and evolution of frictional slipping behavior of carbon fiber/epoxy prepreg," *Fuhe Cailiao Xuebao/Acta Materiae Compositae Sinica*, no. 31, pp. 101–106, 2014.

[81] S. Tumański, *Handbook of magnetic measurements*. Boca Raton, FL: CRC Press, 2011.

[82] H. Niedrig and M. Sternberg, *Das Ingenieurwissen: Physik*. Berlin, Heidelberg: Imprint: Springer Vieweg, 2014.

[83] P. A. Tipler and G. Mosca, *Physik für Wissenschaftler und Ingenieure,* 2nd ed. München, Heidelberg: Elsevier, Spektrum, Akad. Verl., 2004.

[84]   W. Raith, H. Freyhardt, L. Bergmann, C. Schäfer, and H. Gobrecht, *Lehrbuch der Experimentalphysik: Zum Gebrauch bei akademischen Vorlesungen und zum Selbststudium.* Berlin [u.a.]: De Gruyter, 1992.

[85]   R. P. Feynman, R. B. Leighton, and M. Sands, *Vorlesungen über Physik: Elektromagnetismus und Struktur der Materie,* 5th ed. München [u.a.]: Oldenbourg, 2007.

[86]   R. Pitka, S. Bohrmann, H. Stöcker, G. Terlecki, and H. Zetsche, *Physik: Der Grundkurs.* Thun [u.a.]: Deutsch, 1999.

[87]   H. Stöcker, Ed., *Taschenbuch der Physik: Formeln, Tabellen, Übersichten,* 5th ed. Frankfurt am Main: Deutsch, 2005.

[88]   R. Pitka, *Physik: Der Grundkurs,* 3rd ed. Frankfurt am Main: Deutsch, 2005.

[89]   C. B. Scott and D. B. Fischbach, "Diamagnetic studies on as-processed carbon fibers," *Journal of Applied Physics*, vol. 47, no. 12, pp. 5329–5335, 1976.

[90]   D. B. Fischbach and D. W. Gilbert, "Diamagnetic characterization of carbon fibres from pitch mesophase, pitch and polyacrylonitrile," *J Mater Sci*, vol. 14, no. 7, pp. 1586–1592, 1979.

[91]   B. Halbedel, "Magnetische Eigenschaften von Materialien," [Online] Available: http://www.tu-ilmenau.de/fileadmin/media/wt/Lehre/Praktikum/Interdisziplinaeres_Grundlagenpraktikum/_MagMat__Magnetische_Eigenschaften_von_Materialien_v2014.pdf. Accessed on: Nov. 02 2015.

[92]   P. Dobrinski, G. Krakau, and A. Vogel, *Physik für Ingenieure,* 12th ed. Wiesbaden: Vieweg + Teubner, 2010.

[93]   E. Hering, R. Martin, and M. Stohrer, *Physik für Ingenieure: Mit 116 Tabellen und 2 Falttafeln,* 11th ed. Berlin [u.a.]: Springer, 2012.

[94]   F. Brailsford, *Magnetic materials.* London, 1948.

[95]   G. Schweitzer, A. Traxler, and H. Bleuler, *Magnetlager: Grundlagen, Eigenschaften und Anwendungen berührungsfreier, elektromagnetischer Lager.* Berlin [etc.]: Springer Verlag, 1993.

[96]   C. Gerthsen, H. O. Kneser, and H. Vogel, *Physik: Ein Lehrbuch zum Gebrauch neben Vorlesungen,* 16th ed. Berlin, Heidelberg, New York, London, Paris, Tokyo, Hong Kong: Springer, 1989.

[97]   A. Schmidt, *Integrierte Magnetmodule für die berührungslose Führung einer Vorschubachse mit Lineardirektantrieb,* 1st ed. Aachen: Apprimus-Verl., 2012.

[98]   D. Delisle and F. Zacharias, "Berührungsloses Preformen," DE 10 2013 100 861 A1, Jul 31, 2014.

[99]   P. Strasser and C. Biber, "Vorrichtung und Verfahren zur Herstellung eines Kunststoffbauteiles," DE 10 2007 002 309 A1, Jul 17, 2008.

[100]   J. Krüger and A. Salkic, "Preform und Fertigungsvorrichtung für Faserverbundbauteile aus Preformen," DE 10 2010 052 597 A1, May 31, 2012.

[101]   A. Y. Malkin and A. I. Isayev, *Rheology: Concepts, methods, and applications*: Elsevier, 2017.

[102]   A. Oelgarth, *Analyse und Charakterisierung des Fliessverhaltens langfaserverstärkter Pressmassen.* Aachen: Mainz, 1997.

[103]   T. Mezger, *Das Rheologie-Handbuch: Für Anwender von Rotations- und Oszillations-Rheometern,* 2nd ed. Hannover: Vincentz Network, 2006.

[104]   J. Starke, *Beiträge zum Pressen langfaserverstärkter Kunststoffe: Contributions for compression moulding of long fibre reinforced plastics,* 1st ed. Aachen: Verl. der Augustinus-Buchh, 1994.

[105]   K. Skrodolies, *Optimierung der Oberflächengüte von Sheet Moulding Compound-Bauteilen,* 1st ed. Aachen: Mainz, 2007.

[106]   M. P. Ritter, *Material characterisation of long fibre reinforced press masses and characterisation of the compression moulding process by simulation and measurement of the centre of force progression,* 1st ed. Aachen: Mainz, 2003.

[107]   S. Boylan and J. M. Castro, "Effect of reinforcement type and length on physical properties, surface quality, and cycle time for sheet molding compound (SMC) compression molded parts," *J. Appl. Polym. Sci.*, vol. 90, no. 9, pp. 2557–2571, 2003.

[108] A. C. Long, *Composites forming technologies.* Cambridge: Wood-head, 2007.

[109] O. Guiraud, P. Dumont, L. Orgéas, and D. Favier, "Rheometry of compression moulded fibre-reinforced polymer composites: Rheology, compressibility, and friction forces with mould surfaces," *Composites Part A: Applied Science and Manufacturing*, vol. 43, no. 11, pp. 2107–2119, 2012.

[110] D. Schommer, M. Duhovic, F. Gortner, and M. Maier, "Advanced Simulation of Polymer Composite SMC Compression Molding using Fluid-Structure Interaction in LS-DYNA," in *13th International LS-DYNA Users Conference*, Dearborne, 2014.

[111] M. Hohberg, L. Kärger, F. Henning, and A. Hrymak, "Rheological measurements and rheological shell model Considering the compressible behavior of long fiber reinforced sheet molding compound (SMC)," *Composites Part A: Applied Science and Manufacturing*, vol. 95, pp. 110–117, 2017.

[112] J. D. Ferry, *Viscoelastic properties of polymers,* 3rd ed. New York: Wiley, 1980.

[113] M. M. Cross, "Rheology of non-Newtonian fluids: A new flow equation for pseudoplastic systems," *Journal of Colloid Science*, no. 20, pp. 417–437, 1965.

[114] P. J. Carreau, I. F. Macdonald, and B. R. Bird, "A nonlinear viscoelastic model for polymer solutions and melts-II," no. Volume 23, Issue 8, pp. 901–911, 1968.

[115] T. G. Mezger, *The rheology handbook: For users of rotational and oscillatory rheometers,* 2nd ed. Hannover: Vincentz Network, 2006.

[116] J. A. Dantzig and C. L. Tucker, *Modeling in materials processing.* Cambridge, England, New York: Cambridge University Press, 2001.

[117] A. I. Isayev, *Injection and compression molding fundamentals.* New York: M. Dekker, 1987.

[118] *Kunststoffe – Bestimmung der Zugeigenschaften – Teil 4: Prüfbedingungen für isotrop und anisotrop faserverstärkte Kunststoffverbundwerkstoffe*, DIN EN ISO 527-4.

[119] M. Schemme, *Sicherung der Produktqualität bei der Herstellung und Verarbeitung von SMC-Werkstoffen*: Wissenschaftlicher Arbeitskreis Kunststofftechnik (WAK), 1996.

[120] H. Lawonn and A. Hesse, "Fast Maturing of Unsaturated Polyester Resin Prepregs," *Kunststoffe*, no. 65, pp. 678–680, 1975.

[121] P. W. Dufton, *Lightweight thermoset composites: Materials in use, their processing and applications ; a report from Rapra's Industry Analysis and Publishing Group*. Shrewsbury: Rapra Technology Limited, 2000.

[122] S. Rana and R. Fangueiro, *Fibrous and Textile Materials for Composite Applications*. Singapore: Springer Verlag, Singapore, 2016.

[123] K. H. Gudmundsson, F. Jonsdottir, and F. Thorsteinsson, "Modeling Perfluorinated Polyether-Based MR Fluids," *Journal of Intelligent Material Systems and Structures*, vol. 22, no. 15, pp. 1755–1761, 2011.

[124] T. F. Tadros, *Solid/liquid dispersions*. London, Orlando, Fla.: Academic Press, 1987.

[125] T. F. Tadros, *Rheology of Dispersions: Principles and Applications,* 1st ed. Weinheim: Wiley-VCH, 2011.

[126] National Institute of Standards and Technology, *Value of the Boltzmann constant.* [Online] Available: http://physics.nist.gov/cgi-bin/cuu/Value?k. Accessed on: Jul. 18 2016.

[127] J. Mewis and N. J. Wagner, *Colloidal suspension rheology*. Cambridge, New York: Cambridge University Press, 2012.

[128] C. P. Steinmetz and J. L. R. Hayden, *Theory and calculation of electric circuits*: McGraw-Hill, 1917.

[129] J. Svoboda, *Magnetic techniques for the treatment of materials*. Dordrecht, Boston: Kluwer Academic Publishers, 2004.

[130] R. E. Rosensweig, *Ferrohydrodynamics*: Dover Publications, 2013.

[131] T. Lang, "Transport und Strukturbildung in magnetischen Hybriden: Dissertation," 2012. [Online] Available: https://epub.uni-bayreuth.de/192/. Accessed on: Jan. 06 2016.

[132] D. W. van Krevelen and K. t. Nijenhuis, *Properties of polymers: Their correlation with chemical structure ; their numerical estimation and prediction from additive group contributions,* 4th ed. Amsterdam, Boston: Elsevier, 2009.

[133] E. Kallenbach, *Elektromagnete: Grundlagen, Berechnung, Entwurf und Anwendung,* 3rd ed. Wiesbaden: Vieweg + Teubner, 2008.

[134] D. J. Carlson, "MR fluids and devices in the real world," *Int. J. Mod. Phys. B*, vol. 19, no. 07n09, pp. 1463–1470, 2005.

[135] DSM Composite Resins, "Product Data Sheet Daron 41," Aug. 2012.

[136] E. R. Riegel and J. A. Kent, *Kent and Riegel's handbook of industrial chemistry and biotechnology,* 11th ed. New York: Springer, 2007.

[137] M. Szycher, *Szycher's handbook of polyurethanes*. Boca Raton: CRC Press, 1999.

[138] H. Schürmann, *Konstruieren mit Faser-Kunststoff-Verbunden,* 2nd ed. Berlin, Heidelberg, New York, NY: Springer, 2007.

[139] F. Lionetto, A. Moscatello, and A. Maffezzoli, "Effect of binder powders added to carbon fiber reinforcements on the chemoreology of an epoxy resin for composites," *Composites Part B: Engineering*, vol. 112, pp. 243–250, 2017.

[140] P. H. Selden, *Glasfaserverstärkte Kunststoffe*. Berlin, Heidelberg: Springer Berlin Heidelberg, 1967.

[141] M. Karcher, M. Gerlitzki, B. Thoma, and F. Henning, "Evaluation of a new "Inlineprepreg" process approach to establish processes for the manufacturing of structural components out of carbon fiber reinforced plastics," in *15th-Annual Automotive Composites Conference and Exhibition, ACCE 2015*.

[142] GEMMEL METALLE, *Legierungsbeschreibung AlZnMgCu1,5.* [Online] Available: http://www.gemmel-metalle.de/ datenblaetter.html. Accessed on: May 21 2016.

[143] *Plastics - Film and sheeting - Determination of the coefficients of friction*, ISO 8295:1995(E).

[144] *Test Method for Static and Kinetic Coefficients of Friction of Plastic Film and Sheeting*, ASTM D1894-14, 2001.

[145] *Bestimmung der Druckeigenschaften in der Laminatebene*, DIN EN ISO 14126.

[146] *Berichtigungen zu DIN EN ISO 14126*.

[147] *Faserverstärkte Kunststoffe – Bestimmung der Biegeeigenschaften*, DIN EN ISO 14125.

[148] *Kunstoffe-Bestimmung der Charpy-Schlageigenschaften-Teil 1*, DIN EN ISO 179-1.

[149] G. Niemann, H. Winter, and B.-R. Höhn, *Maschinenelemente: Band 1: Konstruktion und Berechnung von Verbindungen, Lagern, Wellen,* 3rd ed. Berlin, Heidelberg: Springer Berlin Heidelberg, 2001.

[150] C. C. Chamis, *Test methods and design allowables for fibrous composites*. Philadelphia, PA: ASTM, 1989.

[151] US Dept. of Defense, *The composite materials handbook-MIL 17*. Lancaster, Pa.: Technomic Pub. Co, 1990?

[152] R. A. Schapery and C. T. Sun, *Time dependent and nonlinear effects in polymers and composites*. W. Conshocken, Pa.: ASTM, 2000.

[153] W. O. Soboyejo, *Mechanical properties of engineered materials*. New York: Marcel Dekker, 2003.

[154] A. A. Baker, S. Dutton, and D. Kelly, *Composite Materials for Aircraft Structures,* 2nd ed. Reston: American Institute of Aeronautics and Astronautics, 2000.

[155] D. Bücheler, A. Kaiser, and F. Henning, "Using Thermogravimetric Analysis to Determine Carbon Fiber Weight Percentage of Fiber-Reinforced Plastics," *Composites Part B: Engineering*, vol. 2016, no. 106, pp. 218–223, 2016.

[156] M. Flemming and S. Roth, *Faserverbundbauweisen Eigenschaften: Mechanische, konstruktive, thermische, elektrische, ökologische, wirtschaftliche Aspekte*. Berlin, Heidelberg: Springer Berlin Heidelberg, 2003.

[157] *Kunststoffe – Bestimmung der Zugeigenschaften – Teil 5: Prüfbedingungen für unidirektional faserverstärkte Kunststoffverbundwerkstoffe*, DIN EN ISO 527-5.

[158] A. Gardziella, L. Pilato, and A. Knop, *Phenolic resins: Chemistry, applications, standardization, safety, and ecology*. Berlin, New York: Springer, 2000.

[159] J. H. Paterson, R. Devine, and A. Phelps, "Complex permeability of soft magnetic ferrite/polyester resin composites at frequencies above 1 MHz," *Journal of Magnetism and Magnetic Materials*, vol. 196-197, pp. 394–396, 1999.

[160] L. Marton and R. A. Fava, *Molecular Structure and Dynamics*. Burlington: Elsevier, 1980.

[161] S. R. Sternberg, "Biomedical Image Processing," *Computer*, vol. 16, no. 1, pp. 22–34, 1983.

[162] L. Eriksson, *Design of experiments: Principles and applications,* 3rd ed. Umeå, Sweden: Umetrics Academy, 2008.

[163] N. R. Draper and H. Smith, *Applied Regression Analysis,* 3rd ed. New York, NY: John Wiley & Sons, 2014.

[164] G. H. Golub and C. Reinsch, "Singular value decomposition and least squares solutions," *Numer. Math.*, vol. 14, no. 5, pp. 403–420, 1970.

[165] L. M. Abrams and J. M. Castro, "Practical guidelines for predicting steady state cure time during sheet molding compound (SMC) compression molding," *Polym. Compos.*, vol. 21, no. 6, pp. 931–940, 2000.

[166] CoreTech System Co., *Moldex3D Support Manual: Flowpack.* [Online] Available: http://support.moldex3d.com/r13/moldex3d/user-interface/analysis-setup/preparing-analysis/computation-parameter/flowpack/.

[167] M. R. Barone and D. A. Caulk, "A Model for the Flow of a Chopped Fiber Reinforced Polymer Compound in Compression Molding," *Journal of applied mechanics-transactions of the asme*, no. 53, pp. 361–371, 1986.

[168] M. M. Shokrieh and R. Mosalmani, "Modeling of sheet molding compound compression molding under non-isothermal conditions," *Journal of Reinforced Plastics and Composites*, vol. 33, no. 13, pp. 1183–1198, 2014.